UNIVERSITY OF SOUTHAMPTON

# Fibre Optic Methods for Measuring Detonation Velocity

by

Josh E. Pooley

ORCiD: 0000-0002-3033-8868

A thesis submitted for the
degree of Doctor of Philosophy

in the
Faculty of Engineering and Physical Sciences
Optoelectronics Research Centre

October 2019

UNIVERSITY OF SOUTHAMPTON

ABSTRACT

FACULTY OF ENGINEERING AND PHYSICAL SCIENCES
OPTOELECTRONICS RESEARCH CENTRE

Doctor of Philosophy

by Josh E. Pooley
ORCiD: 0000-0002-3033-8868

Throughout this project, a number of fibre optic systems have been developed in order to measure detonation velocity — the propagation speed of a shockwave through an explosive medium. The aim of this work has been to utilise the small size and high-speed infrastructure of fibre optic systems to develop precise, high spatial resolution, embedded fibre optic velocity probes.

The three key developments, demonstrated through a combination of simulations, laboratory testing and explosive trials are: an optimised chirped fibre Bragg grating (CFBG) measurement system; a brand new uniform fibre Bragg grating (UFBG) measurement system, and; a simplified, low-cost active fibre measurement system.

It has been discovered that CFBG velocity measurements are prone to innate non-linearities due to Fourier limitations on the grating bandwidth. These effects can be mitigated if the CFBGs are designed with a high chirp-rate and a low reflectivity. This is shown using transfer-matrix simulations and in explosive tests — where the longest continuous CFBG detonation velocity measurement (24 cm) is also demonstrated.

Explosive test results from a new UFBG velocity probe show a maximum noise level that is an order of magnitude lower than similar CFBG tests — demonstrating a noise-limited spatial uncertainty below $\pm 10$ $\mu$m.

Tests on Er and Er/Yb doped fibres demonstrate the potential for these fibres to be used as strain-insensitive detonation velocity probes. This is put into practice by implementing the fibres in a helical geometry — amplifying the spatial precision tenfold and resulting in a $\pm 2$ mm uncertainty over a 100 mm measurement range.

# Contents

# List of Figures

# List of Tables

# Abbreviations

| | |
|---|---|
| ASE | Amplified Spontaneous Emission |
| AWG | Arrayed Waveguide Grating |
| CFBG | Chirped Fibre Bragg Grating |
| CJ | Chapman-Jouguet |
| COTEC | Cranfield Ordnance Test and Evaluation Centre |
| DAQ | Data Acquisition System |
| ENOB | Effective Number of Bits |
| ERDA | Explosives Research and Demonstration Area (Shrivenham) |
| FBG | Fibre Bragg Grating |
| NEP | Noise Equivalent Power |
| PDV | Photonic Doppler Velocimetry |
| PSD | Power Spectral Density |
| RI | Refractive Index |
| SDT | Shock-to-Detonation Transition |
| T-Matrix | Transfer Matrix |
| TOA | Time of Arrival |
| UFBG | Uniform Fibre Bragg Grating |
| WDM | Wavelength Division Multiplexing |

# Declaration Of Authorship

I, Josh Pooley, declare that this thesis and the work presented in it are my own and has been generated by me as the result of my own original research.

Title: Fibre Optic Methods for Measuring Detonation Velocity

I confirm that:

1. This work was done wholly or mainly while in candidature for a research degree at this University;
2. Where any part of this thesis has previously been submitted for a degree or any other qualification at this University or any other institution, this has been clearly stated;
3. Where I have consulted the published work of others, this is always clearly attributed;
4. Where I have quoted from the work of others, the source is always given. With the exception of such quotations, this thesis is entirely my own work;
5. I have acknowledged all main sources of help;
6. Where the thesis is based on work done by myself jointly with others, I have made clear exactly what was done by others and what I have contributed myself;
7. Parts of this work have been published in conference proceedings and journal articles as listed in Publications and Events.

Signed: .....

Date: .....

# Acknowledgements

First, I would like to express my sincerest gratitude to Dr. Morten Ibsen, whose guidance throughout this process has been invaluable. Many of the ideas that are presented in this thesis were conceived during our numerous discussions and I shall remember these occasions fondly. Thanks also to the various members and affiliates of the FBG group who have helped and supported me in the lab, namely Medya, Tan Xiao, Angeliki and Anoma.

This work was funded and carried out courtesy of a PhD studentship, gratefully received from AWE. Much gratitude is owed to the AWE team - Dr. Ed Price, Dr. James Ferguson and Callum Pryer - for their help, supervision and support. I have many good memories of our test weeks in Shrivenham and Salisbury and it was a privilege to work with you all. I would also like to acknowledge the friendly and patient technical support staff at the ERDA (Cranfield University, Shrivenham), COTEC (Salisbury) and the ORC technicians (University of Southampton), who helped to design, build and conduct the cylinder tests safely and efficiently.

Thanks to all my friends and acquaintances at the ORC for their moral support throughout my studies. It has been a real pleasure to meet and work with such a variety of interesting people, from whom I will always have so much to learn!

Finally, I would like to thank my parents (Robert and Katie), my brothers (Ben and Jet) and my partner (Prudence), for all of the love and support that they give me — I couldn't have done it without you!

# Chapter 1

# Introduction

In this project, the use of fibre optics has been examined for applications in detonation velocity sensing. The work is primarily of a practical nature, with various fibre optic probes being fabricated and tested in both laboratory conditions and in a series of explosive tests — carried out at the *ERDA, Cranfield University, Shrivenham campus* and at *COTEC (Rear-battery), Salisbury.*

The aim of this project has been to optimise the use of existing chirped fibre Bragg grating detonation velocity sensors and to develop new fibre optic measurement techniques which are capable of improved spatial precision. To this end, a brand new uniform fibre Bragg grating technique has been developed which shows a tenfold improvement in signal-to-noise ratio.

As an alternative method, Er doped fibres have also been tested in detonation velocity experiments and show promise as a low-cost, strain-insensitive alternative to the aforementioned Bragg grating systems.

The following section introduces and summarises the progression of ideas that are presented in this report.

## 1.1 Report Overview

Detonation velocity is an important parameter in the evaluation of explosive performance and should be measured as accurately as possible in order to validate and improve the design and modelling of explosive systems. In Section 1.2, a brief overview of explosive technology is given and a simple model of detonation is introduced.

The aim of this section is to contextualise the project, by demonstrating how measurements of detonation velocity might be used to characterise the energy output and/or

peak pressure of a particular explosive substance. After this, the use of detonation velocity sensors in modern applications is discussed — in particular, how non-linear effects might be measurable if sensors of sufficient resolution are developed.

Once the utility of detonation velocity measurements has been established, Section 1.3 aims to describe a number of past and present detonation velocity measurement techniques. This section is included in order to determine the measurement range and resolution that can already be achieved and to identify any areas for improvement. It is then determined that the use of optical fibres as potentially high-resolution *embedded* velocity sensors sets them apart from many of the existing photographic, interferometric or electronic systems.

As such, a number of explosive tests have been conducted throughout this project to assess various new and existing fibre optic velocity probes. To ensure that each different technique could be evaluated fairly, all of the tests were carried out in nominally identical conditions. The final design of the test — the nitromethane copper cylinder test — is described in detail in Section 2.1, where each design specification is broken down and justified in relation to the total reliability, efficiency and cost.

Aside from the design of the fibre-optic systems or the explosive test setup, the success of each velocity measurement scheme is also highly dependant on the back-end electronic hardware. In Section 2.2, the noise-floor, dynamic range, responsivity and bandwidth of photodetectors and oscilloscopes is discussed in relation to detonation velocity measurements. This is accompanied by specific examples of how each factor might affect the measurement precision, resolution or linearity.

Starting from Section 3, the remainder of this report is focused on the design and implementation of fibre optic detonation velocity probes — starting with methods involving fibre Bragg gratings (FBGs). However, before the FBG probe designs are described in detail, a theoretical background is given that introduces the important characteristics and parameters for FBG design as a whole.

Section 3.1 starts by qualitatively describing the operating principle of a uniform FBG (UFBG), in regards to its reflection spectrum and Fourier properties. This is then extended to a brief overview of coupled-mode theory, which evaluates UFBG behaviour in a more quantitative and analytical way. After this, chirped and apodized FBGs are introduced in Section 3.1.2, under the general heading “Non-Uniform FBGs”.

In Section 3.1.3, FBG fabrication is discussed, eventually leading to a description of the phase mask setup used to fabricate UFBG detonation velocity probes.

To round off the FBG background section, a description of the transfer-matrix simulation method is given. This simulation method was used regularly throughout this project in order to non-destructively test and design various FBG systems.

The first FBG method to be introduced is the chirped FBG (CFBG) method. In Section 3.2, the basic concept of the CFBG system is introduced with reference to any previous related works. Following on from this, a number of simulations are presented which show the potential for CFBG probes to behave non-linearly if UFBG bandwidth effects are not fully considered. These non-linear effects are also demonstrated in explosive testing and shown to decrease for lower reflectivity and higher chirp-rate gratings.

The CFBG section ends with a summary of the optimal design parameters for a chirped grating probe, as well as some other practical optimisations like signal launch end and the plausibility of additional CFBG filtering.

In Section 3.3, a new FBG based system is introduced, that builds upon the CFBG concept but demonstrates a tenfold improvement in the spatial precision that is attainable. The development of the narrowband UFBG method is given chronologically, from its first iteration, as an array of broadband illuminated UFBGs, to its final form as a single UFBG with narrowband illumination.

This section ends with a brief design summary, discussing the practicalities of UFBG bandwidth and reflectivity.

In this project, non-FBG velocity sensors have also been explored. More specifically, the use of off-the-shelf Er doped fibres as detonation velocity probes have been considered as a simple and low cost alternative to the FBG systems. In this work, standard Er fibre was fielded in explosive tests, in a 1 m long helical formation, demonstrating a spatial precision in the mm–cm scale.

As well as standard Er fibre, a set of laboratory tests were also conducted on high-concentration Er/Yb fibre. Whilst these fibres were not fielded in explosives tests, they do show promise as a strain-insensitive and high-precision velocity sensor over ∼10 mm length scales.

The introduction of the active fibre concept, laboratory results and explosive test results are given in Section 4.

In Section 5, a final review of detonation velocity sensors is given in order to contextualise the work done throughout this project. The measurement ranges, precisions and practicalities of each method are discussed in relation to one another and other more established techniques.

After this, a discussion on the future of fibre optic detonation velocity probes is presented and a variety of new techniques and improvements are introduced.

## 1.2 Explosives and Detonations

The intention of this section is to provide a brief introduction to explosives and detonations. The theory is simple and aims to demonstrate the utility of detonation velocity measurements in explosive characterisation tests.

An explosion is a release of energy, which occurs in a very short time frame (typically $\mu$s timescales). This energy manifests as light, heat and a rapid expansion of gases which do work on their surroundings [1]. There are a variety of circumstances that can result in an explosive event, but most explosions can be categorised as either physical, chemical or nuclear [2]. These categories are defined as follows:

- **Physical:** A sudden release of high pressure gas, perhaps due to the failure of a pressurised vessel [3].
- **Chemical:** A rapid release of energy due to fast exothermic chemical reactions [1].
- **Nuclear:** A rapid release of energy due to changes in the binding energy of atomic nuclei [4].

In this report, the primary focus will be on chemical explosives, which constitute the majority of explosives used in military and civil applications.

Chemical explosives are sub-categorised as either high- or low-explosives. Low-explosives, such as *black powder*, are found in propellants and pyrotechnics and do not detonate in most circumstances [1]. Instead, they are characterised by their ability to *deflagrate*; a process where an exothermic chain-reaction is perpetuated through a substance via the conduction of heat. As such, deflagrations travel at subsonic velocity.

A high-explosive is characterised by its ability to *detonate*. In a detonation, energy is transferred through an explosive in the form of a supersonic shockwave, also known as a *detonation wave*. As this shockwave travels through an explosive, the substantial pressures at the shock-front initiate exothermic chemical reactions. The energy liberated during these reactions reinforces the shockwave, ensuring its continuation.

This mechanism represents the fundamental difference between a shockwave in an inert material (such as air) and a detonation wave. A detonation wave is self-sustained by chemical reactions and can propagate indefinitely, whereas shockwaves travelling through inert materials tend to dissipate quickly – an $R^{-3}$ magnitude decrease for a spherical shockwave at a radial distance $R$ from the source [1].

As a detonation wave progresses through an explosive, it leaves behind a trail of hot exhaust gases – also known as *detonation products*. These products are formed immediately behind the detonation-front in the so-called *reaction zone* and then quickly

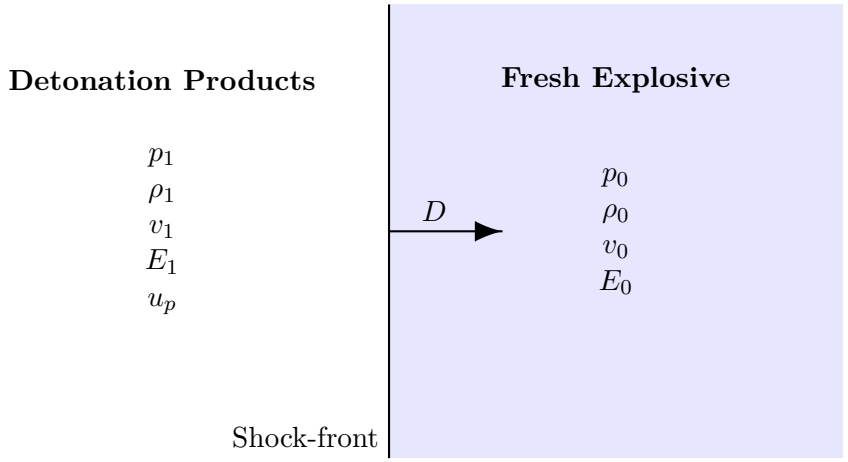


FIGURE 1.1: A simple model of detonation. An explosive exists in two distinct states, pre-shocked and post-shocked, separated by a shock-front and infinitesimal reaction zone.

expand, doing work on the surrounding environment. In rock blasting applications, the transient impact from the shock-front of a detonation creates fissures in the rock, and the expanding exhaust gas prises them open and displaces the fragments [5].

In the characterisation of explosives, the ability of a detonating charge to shatter a target is called *brisance* and the extent to which the exhaust gases can do work on the environment is called *strength* [1]. The strength of an explosive is largely determined by the amount of heat liberated, as well as the volume of gas formed, in the reaction zone. The brisance is largely determined by the velocity of the detonation shock-front and the density of the explosive charge [1].

A simple, one-dimensional, laminar model of detonation is shown in Figure 1.1. In this case, the explosive is only considered to have two thermodynamic states. On the right hand side, the un-reacted explosive is at an initial pressure, $p_0$, density, $\rho_0$, specific volume, $v_0 = \frac{1}{\rho_0}$ and specific internal energy, $E_0$. On the left hand side, the detonation products are at a pressure, $p_1$, density, $\rho_1$, specific volume, $v_1 = \frac{1}{\rho_1}$ and specific internal energy, $E_1$.

The interface between these two regions is the detonation shock-front, which propagates at the detonation velocity, $D$. The particle velocity associated with this detonation wave is denoted $u_p$ and quantifies the average velocity of the particles in the shocked state, immediately behind the shock-front (on the left hand side). In this model, the reaction zone is infinitesimally small because the yield of the chemical reaction induced by the shock-front is assumed to be full and instantaneous [6].

As the shock-front progresses through the fresh explosive, the total mass, momentum and energy in the system must be conserved. This leads to the formulation of the three

conservation equations, which help to predict the state of the detonation products given some initial conditions and experimental measurements.

### *Conservation of Mass*

In a time, $\Delta t$, the shock-front has progressed a distance $D\Delta t$ into the fresh explosive. For an arbitrary cross-sectional area, $\alpha$, the mass of fresh explosive that is consumed in this time interval is $\rho_0 \alpha D \Delta t$.

The detonation products produced in the same time interval acquire a velocity, $u_p$, and occupy a volume $\alpha(D - u_p)\Delta t$. The mass gained in detonation products is then $\rho_1 \alpha (D - u_p)\Delta t$.

In the frame of the shockwave, it is intuitive that the mass of the explosive entering from the right-hand side should equal the mass of the detonation products leaving on the left-hand side. This leads to the conservation of mass equation [6, 7],

$$\rho_0 \alpha D \Delta t = \rho_1 \alpha (D - u_p)\Delta t, \tag{1.1}$$

$$\rho_0 D = \rho_1 (D - u_p). \tag{1.2}$$

### *Conservation of Momentum*

In the time interval, $\Delta t$, the change in momentum across the shock-front is a product of the mass difference, $\rho_0 \alpha D \Delta t$, and the newly acquired particle velocity, $u_p$. The rate of change of momentum is, therefore, $\rho_0 \alpha D u_p$ (the change in momentum divided by the time interval $\Delta t$).

From Newtonian mechanics, this should be equal to the force required to transition between the pressure states, $p_0$ and $p_1$, which in this case is $\alpha(p_1 - p_0)$. This leads to the momentum conservation equation [6, 7],

$$\alpha(p_1 - p_0) = \rho_0 \alpha D u_p, \tag{1.3}$$

$$p_1 - p_0 = \rho_0 D u_p. \tag{1.4}$$

***Conservation of Energy***

The conservation of energy requires that the kinetic and internal energies on either side of the shock-front are balanced by the chemical potential energy released during the reaction.

In the frame of the shock-front, the kinetic energy per unit mass of the fresh explosive entering from the right-hand side is $\frac{D^2}{2}$. The detonation products immediately behind the shock-front leave with a kinetic energy per unit mass of $\frac{(D-u_p)^2}{2}$.

This leads to the energy conservation equation [6],

$$\frac{D^2}{2} + p_0 v_0 + E_0 = \frac{(D-u_p)^2}{2} + p_1 v_1 + E_1. \tag{1.5}$$

***Determining the Final State***

These three conservation conditions, Equations 1.2, 1.4 and 1.5, can now be combined in order to restrict the possible final states ($p_1$, $v_1$, etc.), given some initial conditions and experimental measurements. Assuming that the initial conditions ($p_0$, $v_0$, etc.) are known, the system is reduced to five unknown variables ($E_1$, $p_1$, $v_1$, $u_p$, $D$). In this case, the measurement or determination of two detonation variables will reveal the value of the remaining three by virtue of the conservation equations.

To show this graphically, the conservation equations can be rearranged in terms of the final state pressure and specific volume, $p_1$ and $v_1$. These parameters are conventionally chosen to be the "unknowns", because they are particularly difficult to measure, especially in comparison to the detonation velocity [8].

By combining Equations 1.2 and 1.4, it is possible to eliminate the particle velocity, $u_p$, and find the equation of the *Rayleigh* line [6],

$$\rho_0^2 D^2 = \frac{p_1 - p_0}{v_0 - v_1}. \tag{1.6}$$

For a known initial state, $p_0$ and $v_0$, Equation 1.6 describes a straight line in ($v$, $p$) space, for a constant detonation velocity, $D$. If the detonation velocity is known, then the possible final state, ($v_1$, $p_1$), must exist somewhere along this line. Figure 1.2 shows the initial state, ($v_0$, $p_0$), and a Rayleigh line which passes through it.

If Equations 1.2, 1.4 and 1.5 are combined, so as to eliminate both $D$ and $u_p$, the equation of the *Hugoniot* curve is found to be [6]

$$E_1 - E_0 = \frac{1}{2}(p_1 + p_0)(v_0 - v_1). \tag{1.7}$$

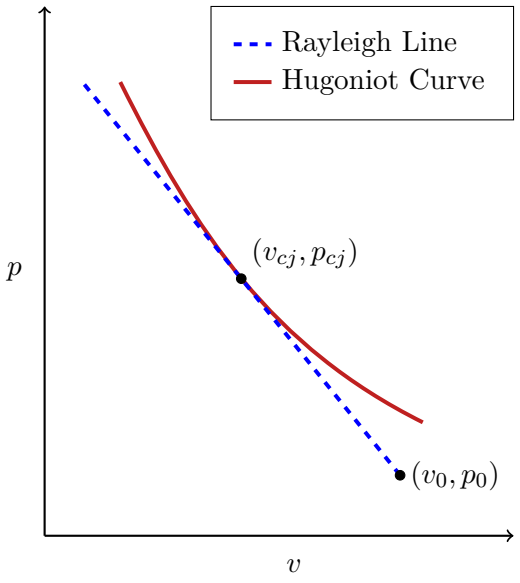


FIGURE 1.2: Diagram showing ($v$, $p$) space, for the simple detonation model shown in *Figure 1.1*. The initial state is labelled $(v_0, p_0)$ and the Rayleigh and Hugoniot lines show the possible final states, corresponding to a known detonation velocity, $D$, and specific internal energy, $E_1$. The Chapman-Jouguet state is labelled $(v_{cj}, p_{cj})$ and represents the only single state solution.

For known initial conditions, $E_0$, $p_0$ and $v_0$, Equation 1.7 describes a reciprocal function in ($v$, $p$) space, for a known final state internal energy, $E_1$. A Hugoniot curve is illustrated in Figure 1.2.

It is necessary that any final state, ($v_1$, $p_1$), must satisfy both the Rayleigh and Hugoniot conditions. Possible states are, therefore, further reduced to include only the *intersections* of the Rayleigh and Hugoniot lines in ($v$, $p$) space.

For a known final state Hugoniot, some detonation velocities will be impossibly low, corresponding to a Rayleigh line that never intersects it. However, for a majority of other detonation velocities, there are *two* intersection points, known as the strong and weak solutions [6].

At one particular detonation velocity, the Rayleigh line will intersect the Hugoniot curve tangentially, crossing at only a single point. This is known as the Chapman-Jouguet (CJ) point and is labelled in Figure 1.2 with the coordinates ($v_{cj}$, $p_{cj}$) [6]. For a steady state detonation, with a constant detonation velocity, the detonation products are in the CJ state [9].

From this simple analysis, it is possible to understand why detonation velocity is frequently measured when characterising explosives. Even for qualitative comparisons, it can be understood from Figure 1.2 that a higher detonation velocity may be indicative of a higher final state pressure, or a higher energy yield in the reaction zone.

### Beyond the Simple Model

The simple detonation model, shown in Figure 1.1, introduces a few crucial variables and how they may relate to one another in a simplified scenario, but it is not complete. Two examples of possible extensions to this theory are given below:

- The final state variables shown in Figure 1.1 represent the conditions immediately behind the shock-front, but for a more comprehensive analysis, a rear-boundary condition is required to evaluate the so-called "following flow" [6].
- The reaction zone in the simple model is reduced to an infinitesimally small width. In reality, the reaction does not happen instantaneously, and thus occupies a *finite* width. This is realised in the Zel'dovich, von Neumann, Döring model [6].

For many "real-life" cases, models are required which consider various three-dimensional geometries, with detonations that cannot be assumed to propagate as plane waves. Handley et al. [9] define two regimes in which these problems require consideration.

First, the pre-detonation phase, between the initiation stimulus and the transition to detonation. Studies in this regime may concern the evolution of different input stimuli and the affect of various geometries or wave shapes on the run-to-detonation distance [9].

The second regime, once a detonation has been established, may concern the response of detonation waves to geometrical features such as bends or corners. Other interesting phenomena in this regime may include the interaction between a detonation wave and other shockwaves in the same medium [9].

Throughout the lifetime of a detonation, from initiation through to steady state and beyond, the application of detonation velocity sensors can be elucidating.

For example, in shock-to-detonation experiments, where an explosive is initiated via a controlled incident shock, it is possible to measure the shock-to-detonation transition (SDT) using shock/detonation velocity sensors [10].

For propagating detonation waves, detonation velocity measurements may also be able to monitor the progress of a detonation wave around a corner, or determine the effects of various other conditions on the rate of propagation. This has been demonstrated, using fibre optic velocity sensors, in the tracking of detonation waves across material boundaries [11].

## 1.3 Review of Existing Technology

Having established that detonation velocity is an important characterisation parameter for explosives, this section aims to review existing techniques for measuring it and introduce some of the potential benefits of using fibre optic sensors.

### 1.3.1 Fibre Optic Sensing

The function of a sensor is to convert environmental stimuli into a human readable form through a process of transduction. Given the advancement of electronics and computing in recent times, most contemporary sensing systems utilise electronic transducers that are directly monitored using electronic hardware [12].

In environments where electronic components are sensitive to undesirable stimuli, hazardous to implement or incompatible in some other way, a fibre optic transducer can offer several advantages. These advantages include [13, 14]:

- Small size;
- Immunity to electromagnetic interference;
- Chemical stability;
- Ability to function in high temperature environments; and
- Multiplexing capabilities.

The use of fibre optic sensors will usually require an additional transduction interface, so that electronic hardware can still be used to monitor, digitise and store information from the optical signal. Therefore, the two interfaces are **Stimulus** $\Longrightarrow$ **Optical Signal** and **Optical Signal** $\Longrightarrow$ **Electrical Signal**.

These interfaces correspond to the two major considerations for fibre optic sensor design. First, how does the fibre optic transducer physically respond to external stimuli and how can this response be interrogated? Secondly, how does the choice of detector, oscilloscope and/or other back-end hardware affect the accuracy, reliability and precision of the results?

An example of a fibre optic transducer is the fibre Bragg grating (FBG). FBGs are intricate structures, typically comprising sub-micron scale perturbations in the core of an optical fibre [15]. These perturbations are periodic, such that incident light whose wavelength satisfies the Bragg condition may undergo a reversal of propagation direction. The Bragg condition for an FBG with a period $\Lambda_{FBG}$ is

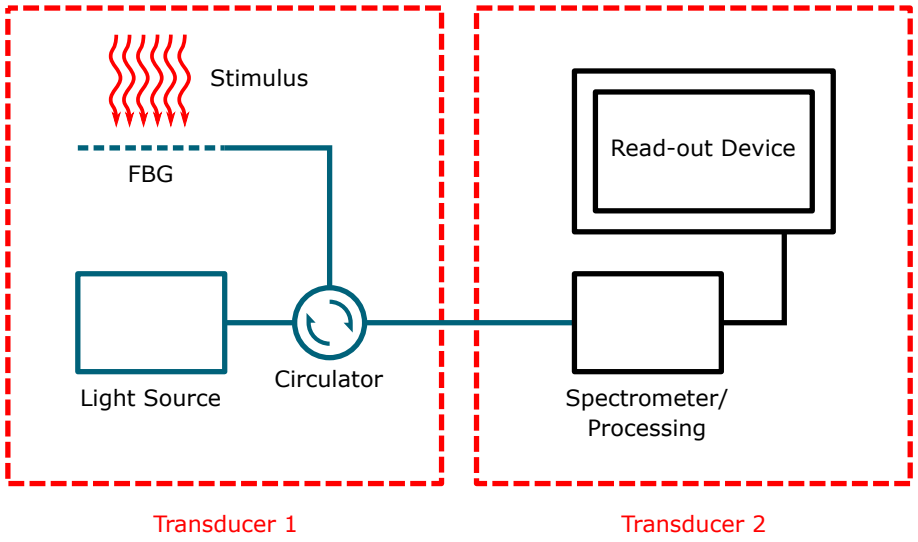


FIGURE 1.3: A schematic showing the transduction-train for a typical FBG sensor. The environmental stimulus is encoded into an optical signal using an FBG and a circulator. The optical signal is then analysed with electronics so that the measurement can be interpreted by an engineer.

$$\lambda_{Bragg} = 2n_{eff}\Lambda_{FBG} \tag{1.8}$$

where $\lambda_{Bragg}$ is the resonant wavelength (Bragg wavelength) and $n_{eff}$ is the effective refractive index of the mode. FBGs can be used as transducers because the effective index and pitch, which constitute this Bragg condition, are sensitive to environmental stimuli.

A simple FBG sensing setup, with twofold transduction, is shown in Figure 1.3. This system could work well for a stimulus like temperature, which the Bragg wavelength of the FBG is directly sensitive to [16]. By illuminating the FBG with a broadband light source and isolating the reflected signal with a circulator, information regarding the stimulus can be encoded in an optical signal. This is the function of the first transducer.

In the second transducer, the optical signal, containing information about the external stimulus, is further converted into an electrical signal. An electronic read-out device can then display, digitise or store this information. Calibration of each transducer in the chain allows the original stimulus to be inferred from the measured electrical signal on the read-out device.

A system like this, where only Transducer 1 is exposed to the stimulus, is useful in environments where electromagnetic (EM) interference is overwhelming or where electronic equipment is too bulky or otherwise incompatible. There are many industries which require sensors of this kind [14], a few examples are listed here:

- Inert, miniaturised medical sensors [17];

- Lightweight, electromagnetically immune sensors for high voltage environments [18];
- Durable, distributed sensors for structural health monitoring [19];
- Non-mechanical, lightweight gyroscopes for transport/defence [20].

### 1.3.2 Detonation Velocity Sensing

As discussed in Section 1.2, measurements of detonation velocity are crucial in the characterization of explosive performance. In order for these measurements to be accurate and reliable, an unobtrusive transduction mechanism is required which can be monitored at sufficient speed (>10 MHz). Standard optical fibres with a diameter of 125 $\mu$m are well suited to this and optical signals can be measured at GHz speeds owing to technology developed for the telecoms industry.

Despite the advantages associated with fibre optic sensing, a variety of diagnostic techniques are regularly implemented for measurements of detonation velocity. These can be loosely categorized as either *electronic*, *photographic*, *interferometric* or *fibre optic* [8] and are summarised in Table 1.1.

| **Category** | **Example Techniques** |
|---|---|
| Electronic | • Ionisation pins<br>• Piezoelectric pins<br>• Continuous resistance wire |
| Photographic | • Rotating mirror streak camera<br>• Rotating mirror framing camera<br>• Electronic streak camera |
| Interferometric | • Photonic Doppler velocimetry (PDV) |
| Fibre Optic | • Fibre-coupled light detection<br>• Drilled fibre optic probe<br>• Aluminium coated time of arrival diagnostic (TOAD)<br>• Chirped fibre Bragg grating (CFBG) |

TABLE 1.1: A summary of detonation velocity measurement techniques and their categories.

Many of these techniques, particularly those in the electronic and fibre optic categories, can be further categorized as *Time-of Arrival (TOA)* devices. A TOA device consists of a probe (*continuous TOA*), or set of probes (*discrete TOA* or *point-to-point*), that monitor the progression of a detonation shockfront via direct contact with the explosive.

### Discrete TOA

An example of an electronic discrete TOA device is the piezoelectric pin method, whose general operating principle is shown in Figure 1.4. In this scheme, pins are mounted perpendicularly along the length of an explosive charge with a known separation, $\Delta Z$. Once the detonation is initiated, the shockwave propagates through the unshocked explosive at an unknown velocity, $V$. When the shock front reaches a pin, a transient electrical impulse is triggered which can be picked up by an oscilloscope. The duration, $\Delta t$, between each triggering event can be measured to determine the detonation velocity, $V = \frac{\Delta Z}{\Delta t}$.

This is a relatively crude system, where the spatial resolution is determined by the spacing between each successive pin (the exposed sensing end of a piezoelectric pin is typically around 1 mm in diameter, but may be housed in a larger frame). However, the robustness of the concept means that the results are reliable and data acquisition is simple and easy to analyse.

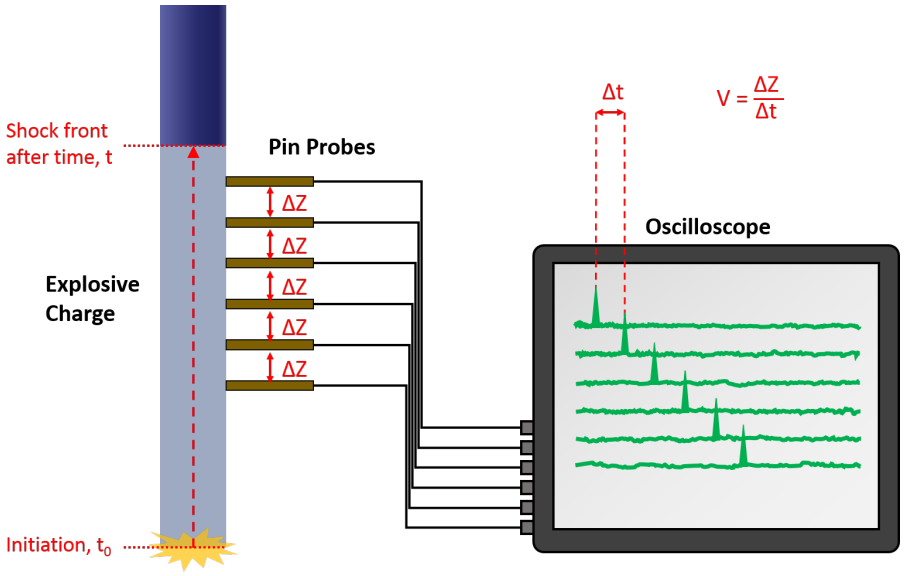


FIGURE 1.4: A schematic showing the operating principle for pin probe discrete TOA devices.

Fibre optic systems based on the same discrete TOA concept include *fibre-coupled light detection* [21, 22], *drilled fibre-optic probes* [21, 23] and the *aluminium coated time of arrival diagnostic (TOAD)* [24].

Fibre-coupled Light Detection sees fibres mounted perpendicular to the shockwave direction, in place of the pins in Figure 1.4. This time, an *optical* impulse is generated via fibre coupling of the residual explosive light, which can then be recorded using a photodetector and an oscilloscope/digitiser.

Drilled Fibre-Optic Probes are fibres which have holes drilled along their length at known intervals. A fluorescent optical impulse is generated from each hole as the air is

compressed and ionised by the shock front. In this case, only a single fibre is required, which is mounted parallel to the shockwave propagation direction and connected to a photodetector and an oscilloscope/digitiser.

These devices are affordable because they require little in the way of back-end hardware and can be implemented using standard telecom or PMMA optical fibre. Fibre-coupled Light Detection has been shown to produce well-defined impulses in experiments where crosstalk is unlikely. However, when probe fibres are in close proximity or housed in transparent media, ghost-peaks and peak-broadening can occur which makes analysis difficult. These effects can be mitigated with the use of multiple channels, but this would require a photodetector for each channel [22]. The measurement precision for fibre-coupled light detection is limited by the diameter of the core, which is less than 10 $\mu$m for standard single mode telecoms fibre.

The Drilled Fibre-Optic Probes need only a single detector, but impulse generation is not consistent. In the tests here [21], half of all cases required additional peak fitting techniques and gave velocities as far as $\sim$16% below expected. The spatial resolution in this case was 120 mm, with a maximum spatial precision (based on the hole diameter) of 0.5 mm.

The most contemporary discrete TOA device is the aluminium coated TOAD. In the TOAD device, an array of fibre end-facets are coated with a reflective layer of aluminium before being mounted on an explosive charge. When a shockwave reaches one of the fibre ends, the aluminium coating is disturbed, resulting in a sudden drop in reflectivity for that channel. This can be monitored by illuminating each fibre end with a light source and monitoring the reflected power with a fast photodetector.

This method is more robust than the Fibre-coupled Light Detection system, because it is not susceptible to crosstalk and because it does not rely on explosive luminosity. Therefore, it can also be implemented parallel to the shockwave propagation direction and on metal surfaces.

In this implementation of the TOAD system [24], each fibre was separated by just 250 $\mu$m in a 1.25 mm wide 6-by-6 array. This is a particularly good spatial resolution compared to other discrete TOA devices, but its implementation is still limited. When high spatial resolution ($\leq$ 100 $\mu$m) measurements are required to monitor dynamic changes in velocity over 10+ mm lengths, discrete TOA devices become increasingly unfeasible. In this case, continuous measurement techniques are required.

### Continuous Methods

Systems that continuously monitor detonation velocity are found in the *Photographic* and *Interferometric* categories of Table 1.1, as well as the remaining *Electronic* and *Fibre*

*Optic* techniques which can be grouped together as *Continuous TOA* methods.

### Streak Cameras

A streak camera is similar to an ordinary camera, only the dimensions are transposed. Instead of taking a single exposure which produces an X-Y photograph, a streak camera takes a continuous one-dimensional image and sweeps it across a photosensitive film resulting in an X-t photograph.

The application of streak cameras for detonation velocity measurements is illustrated in Figure 1.5. In this case, the emission of electromagnetic radiation behind the shock front is detected on a streak camera that has a known smear-rate. The resultant photograph is a distance-time graph whose gradient yields the velocity of detonation [8].

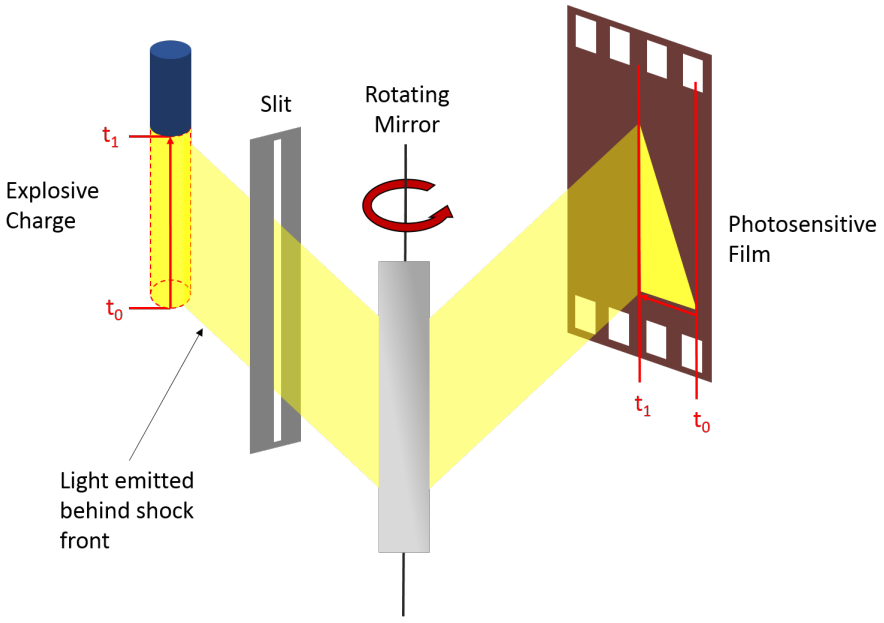


FIGURE 1.5: A schematic showing the operating principle of a streak camera.

Streak cameras can also operate electronically, where the explosive luminescence is transferred to an electron beam using a photocathode. Once in electron beam form, the image can be deflected by charged plates, which apply a time-streak in the same vein as the rotating mirror in the optical streak camera. The beam is then captured on a film behind the charged plates and a distance-time graph is acquired. This system overcomes the various limitations associated with rotating mechanical components and can, therefore, achieve higher scanning speeds [8].

The spatial resolution obtained from various kinds of streak camera photographs can be very high, corresponding to temporal resolutions down to the nanosecond [8]. However, streak camera diagnostics are not viable in all scenarios because they require direct optical access and have limited measurement duration.

### Interferometers

Interferometric techniques are distinguishable from TOA devices and streak cameras because they directly measure velocity. The transduction process is simple and exploits the doppler shift incurred by an optical signal reflecting from a moving surface. Photonic Doppler Velocimetry (PDV) is a fiberised interferometric technique for measuring the velocity of fast-moving surfaces [25].

The basic PDV operating principle is shown in Figure 1.6. Here, a fibre coupled coherent light source is incident on a moving surface. The signal reflects from the surface and undergoes a wavelength shift that is proportional to the surface velocity. Some of the doppler shifted light is coupled back into the fibre, where it is mixed with a reference signal to produce a beat frequency. Since the beat frequency is sufficiently low compared to the original signal frequency, it can be measured using high-speed photodetectors (GHz speeds). The surface velocity is then related to the beat frequency in the following way [25]:

$$v_s = \frac{f_b}{2f_0} \cdot \frac{c}{n} \tag{1.9}$$

where $v_s$ is the surface velocity, $f_b$ is the beat frequency, $f_0$ is the source frequency, $c$ is the speed of light and $n$ is the refractive index surrounding the reflecting surface. The approximate precision of this system is determined by the uncertainty principle,

$$\Delta f_b \geq \frac{1}{4\pi\tau}, \tag{1.10}$$

where $\tau$ is the time window over which the beat frequency is examined [26].

In some cases, PDV has been used as an embedded fibre optic probe for continuous detonation velocity measurements [27]. This is a surface velocity measurement where Fresnel reflections from the fibre end-facet are responsible for the Doppler induced beat frequency and can, therefore, only be implemented in tests that maintain a flat end-cleave. For this reason, PDV has not yet been used to measure detonation velocity in consolidated charges, because the pressure surrounding the fibre is not homogeneous enough to sustain a sufficiently flat surface.

### Continuous TOA

As is characteristic of all TOA methods, *Continuous* TOA devices monitor the progression of a detonation wave via direct interaction between the shockfront and the transducer. The distinguishing feature of continuous TOA devices is that they infer shock

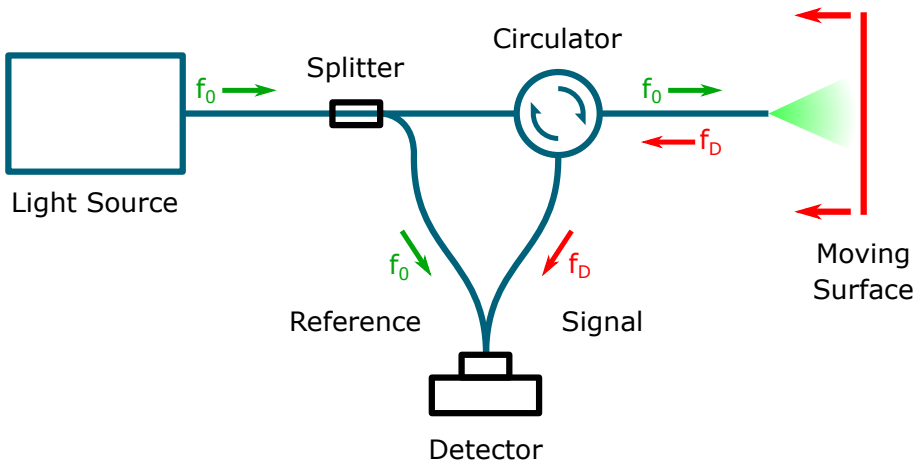


FIGURE 1.6: Schematic showing the operating principle of a photonic doppler velocimeter (PDV).

front position from the *length* of the transducer which remains intact, not the *number* of transducers which remain intact (discrete case). This means that dynamic changes in the detonation velocity, from initiation through to steady-state, can be measured. The continuous TOA principle is illustrated in Figure 1.7.

An example of an electronic system that utilises the continuous TOA principle is the Continuous Resistance Probe [28]. This consists of a pair of conducting wires which are mounted in parallel with the shockwave propagation direction and are initially insulated from one another e.g. a coaxial cable.

As the cable is destroyed by the shockwave, the two wires are crushed together, allowing a constant current to flow between them at the position of the shock-front. Since the electrical resistance of these wires depends on their length, the detonation velocity can be inferred by monitoring their potential difference over time (in accordance with Ohms law).

Conceptually, the Continuous Resistance Probe has a limitless spatial resolution, limited only by the speed and/or digitisation of the data acquisition hardware. In reality, the method can be unreliable since it depends on adequate current flow and is vulnerable to EM interference, particularly from high-voltage detonators [28]. Furthermore, for high resolution, embedded diagnostics, standard coaxial cables are too bulky. For these reasons, continuous detonation velocity probes which utilise fibre optic technology have been an active area of research over the past decade.

A fibre optic transducer which has more recently been applied to Continuous TOA systems is the Chirped Fibre Bragg Grating (CFBG) [29, 30, 31, 32]. A CFBG is an integrated fibre optic filter whose spectral bandwidth is proportional to its physical length. Similar to the Continuous Resistance Probe, the fibre containing the CFBG is mounted parallel to the shockwave propagation direction and illuminated with a broadband light source. As the CFBG is destroyed, the total reflected power from the grating decreases

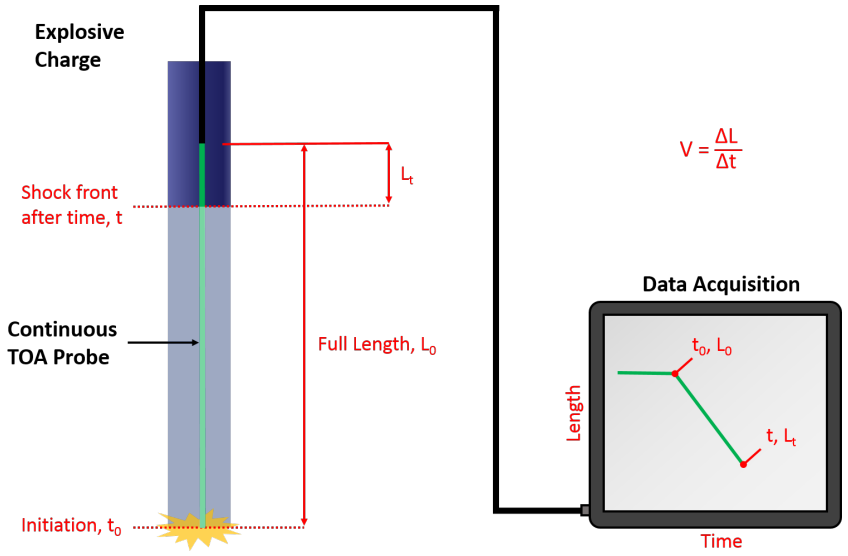


FIGURE 1.7: A schematic showing the operating principle of a continuous TOA device.

as chunks of the filter bandwidth are removed. The detonation velocity is then inferred from the rate of change of optical power reaching a photodetector.

Many early publications of the CFBG technique focus on determining an accurate length-to-wavelength mapping for each grating. Methods include destructive testing, with laser cutbacks [29, 30] and via polishing [33], as well as non-destructive calibration methods such as optical backscatter reflectometer (OBR) scanning or heat probing [34]. More recent calibration techniques have begun to look more closely at each CFBGs spectral behaviour, including how to overcome distortions [31] and how to spectrally resolve each CFBG spectrum at high speed [35].

The CFBG method for determining detonation velocity has many of the discussed benefits associated with fibre optic sensing. Like the Continuous Resistance Probe, the transduction is continuous and therefore the spatial resolution is primarily limited by the acquisition hardware – a factor which will be discussed in Section 2.2. It will also be demonstrated – in Section 3.2 – that CFBG detonation velocity probes have an inherent non-linear quality which, depending on the reflectivity and bandwidth of the probe design, can affect the accuracy of the velocity readings.

Two other fibre optic continuous TOA systems are also introduced in this report. One is an extension of the CFBG method, but utilises uniform fibre Bragg gratings (UFBG) as a measurement probe. This new method is shown – in Section 3.3 – to reduce levels of optical noise by as much as an order of magnitude.

The second technique is a modification of an active fibre velocity probe system [36], and demonstrates the use of off-the-shelf and pre-calibrated Er doped fibre sensors in explosive and laboratory tests. This simple and cost effective technique is discussed in detail in Section 4.

Together, the CFBG, UFBG and active fibre probe methods have been studied and developed in the hope of measuring shock propagation down at the 10 $\mu$m scale. Measurements on this scale offer a significant improvement over state-of-the-art discrete techniques ($\sim$250 $\mu$m resolutions) and may be able to resolve propagation through individual crystals in the explosive (Majiet and Mostert [37], for example, have studied RDX with average crystal sizes in the 30–300 $\mu$m range).

# Chapter 2

# Experimental Design

Throughout this project, a number of novel detonation velocity measurement techniques have been conceptualised and simulated as well as tested in explosive trials. In order to make a direct comparison between any new and established detonation velocity probes, each measurement system was tested under the same conditions in a series of nominally identical "cylinder tests".

In the following section, a description of the cylinder test is given, along with the motivations leading to its design. After this comes a discussion about the back-end electronic hardware and how its specifications affect the quality of recorded data in these experiments.

## 2.1 Cylinder Test

The overall aim of this project was to develop new detonation velocity measurement techniques that are capable of sub-mm spatial resolutions in non steady-state conditions. Two properties which are crucial to the fulfilment of this brief are *Probe Linearity (or Ability to be Calibrated)* and *Signal-to-Noise Characteristics*. Experimental testing should aim to isolate these properties in the following way:

**To Determine Linearity/Ease of Calibration**

- The probe should be mounted in a controlled way – any angular offsets or bends in the probe that are left unaccounted for will result in erroneous velocities and an unfair representation of the measurement system.
- The detonation characteristics should be predictable – if the behaviour of the explosive is unknown, then non-linear detonation effects cannot be decoupled from probe non-linearities.

- The expected velocity range must be above the sonic velocity of the probe – if the test explosive has a detonation velocity which is slower than this, disturbances in the probe will run ahead of the detonation wave and negatively affect results.
- Established probes should be implemented simultaneously – if multiple test methods are used simultaneously, probe and detonation behaviours can be decoupled more easily.

**To Determine Signal-to-Noise Characteristics**

- The probe should be mounted in favourable conditions – any environmental conditions that are likely to contribute to increased noise levels should be avoided. E.g. non-uniform strain on the probe could unfairly degrade signal quality if not considered.
- Established probes should be implemented simultaneously – if multiple test methods are used simultaneously, spurious noise contributions (e.g. explosive radiation) can be decoupled from the systems noise characteristics.

Based on this criteria, a cylinder expansion test setup was chosen, with a liquid explosive – sensitised nitromethane – as the main charge [38]. The setup consisted of a 300 mm long copper pipe, with a 31.75 mm external diameter and a 3.18 mm wall thickness, which was held upright on a perspex base. Inserted into the bottom of the pipe was an o-ring sealed brass plug, housing a PE8 booster charge with room for a detonator. At the top of the pipe was a nylon lid which was drilled to accommodate multiple velocity probes and a filling hole to pour in the nitromethane. A diagram of this setup is shown in Figure 2.1(a).

For practicality, and to allow the fibre to hang as straight as possible, each fibre probe was partially housed in a stainless steel tube, which was secured in place by a heat shrink wrapping. The probes could then be inserted manually into the "push-fit" lid holes, with the depth set by the length of exposed tubing. This is illustrated in Figure 2.1(b).

A photograph of the fully assembled setup is shown in Figure 2.2, along with an illustration of the fibre probe hanging inside the cylinder and the full explosive train (detonator→booster→main charge).

This setup was chosen for numerous reasons. First, using a liquid explosive allows the fibre probes to be mounted without adhesives and in direct contact with the explosive. This ensures that all probes are held in identical conditions and without significant non-uniform strain or temperature gradients along their length. The fact that the probes are fully embedded in the explosive also means that they will be destroyed smoothly by the detonation-front. Figure 2.3 shows a comparison of two similar FBG cylinder

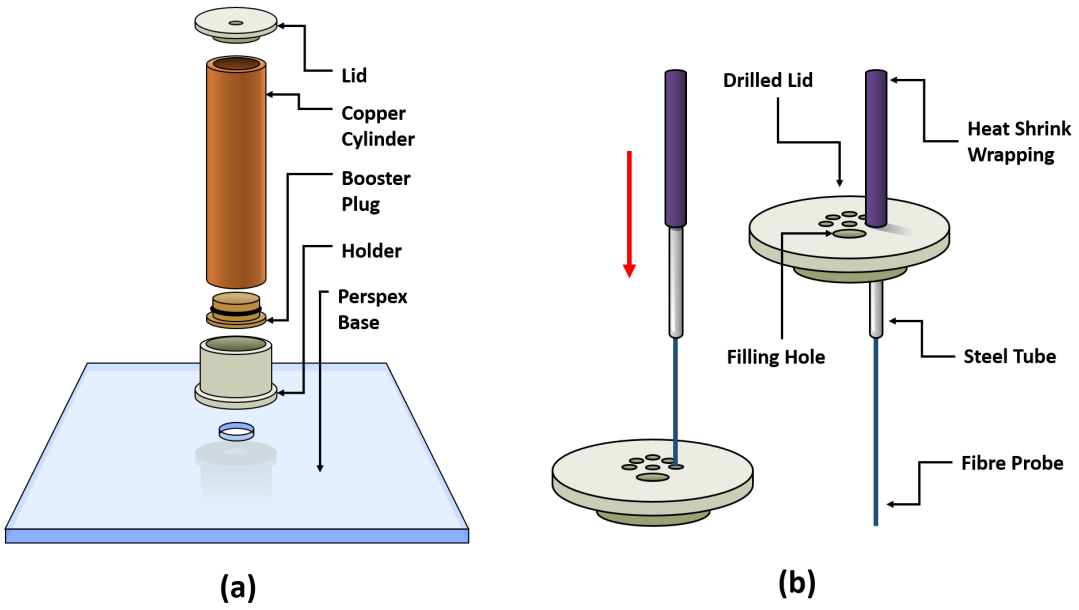


FIGURE 2.1: (a) A diagram of the cylinder test setup. (b) A detailed diagram of the drilled lid and fibre probe mounting system.

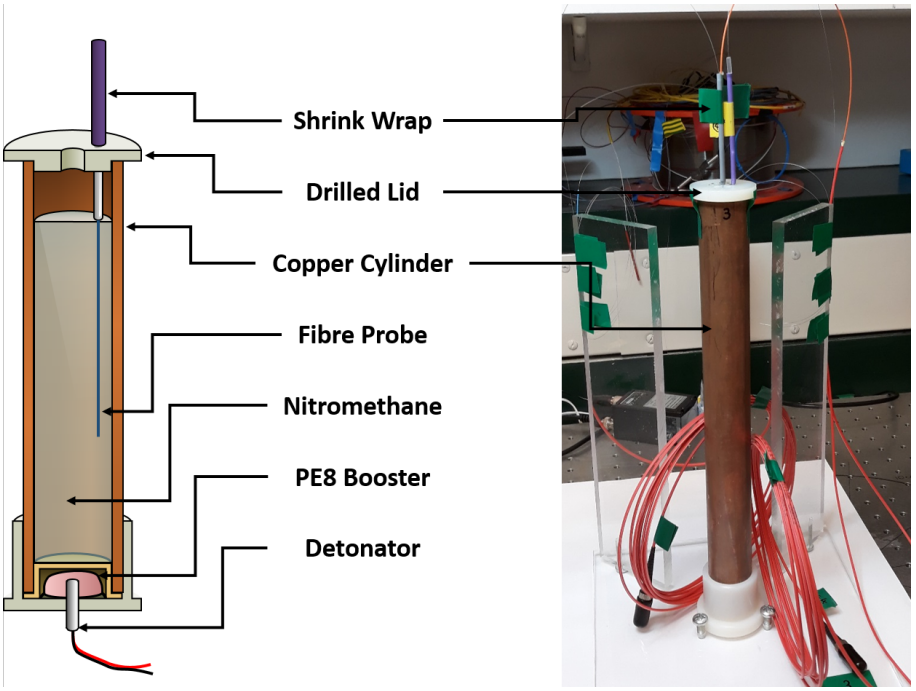


FIGURE 2.2: A photograph of the cylinder test setup, along with an illustration of the fibre probes hanging inside.

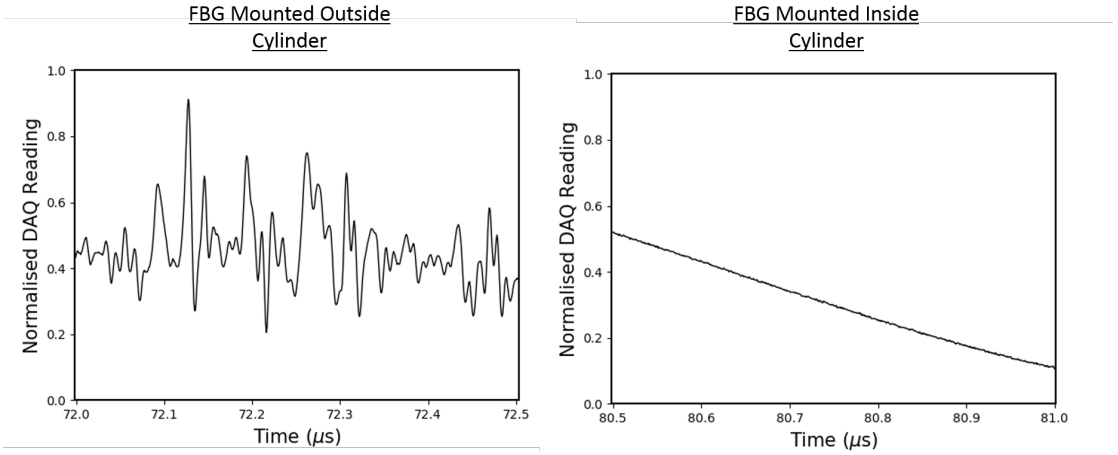


FIGURE 2.3: A 0.5 $\mu$s sample of data from two FBG velocity probes. One is mounted outside the cylinder, whilst the other is hanging inside the cylinder, immersed in a liquid explosive.

tests, where one probe is mounted on the outside of the cylinder using adhesive tape and the other is mounted on the inside using the drilled lid system in Figure 2.1(b). The additional noise from the outside mounted probe is thought to be, in part, due to small air gaps between the cylinder and fibre, causing the FBG to be destroyed in irregular intervals. There may also be additional coupling of explosive radiation into the fibre — but this is largely speculative.

Secondly, nitromethane is a well characterised and reliably detonated explosive. For the optical fibre probes used in this project – made from Ge-doped silica – the sonic velocity in the probes [39] is lower than the anticipated nitromethane detonation velocity [40]. This ensures that detonation velocity readings are based on the position of the shock-front in the *explosive* itself and not based on acoustic disturbances in the fibre probe.

To eliminate any potential non-linearities in the detonation velocity, all of the velocity probes were mounted so that they would lie in the top half of the cylinder. This is a region where the detonation is expected to have reached steady-state and propagate at a constant velocity. Whilst this is not essential for the fibre-optic probe characterisation, it does simplify analysis. If the probes were fielded in regions of non-linear velocity, the behaviour of the explosive must be extremely well characterised in order to decouple these effects from any non-linearity inherent in the probe.

One final, and very important, aspect of the test design was the multiple probe implementation. The design of the lid allowed for up to six fibre probes to be fielded simultaneously in the top half of the cylinder. Any spurious results due to non-linearity in the detonation or excessive explosive radiation can, therefore, be identified by comparing the data from each probe. Equally, any excess noise or non-linearity that is unique to each measurement system will become apparent.

In order to quantify the absolute accuracy of each new probe, a velocity reading is required that uses established methods. In these tests, a PDV (interferometric) probe was used as the benchmark. A description of this method can be found in Section 1.3.2.

## 2.2 Detectors and Oscilloscopes

The techniques demonstrated in this report determine shock-front position based on optical signal power. For the optical signal power to be monitored, it must first be converted into an electrical signal using a photodetector. A photodetector is a device, containing a photodiode, that outputs a voltage proportional to the power of an incident optical signal.

In order to monitor the voltage change in a specific time window, the output from a photodetector is sent to an oscilloscope or data acquisition system (DAQ). The result is a digital voltage trace, where foreknowledge of the probes erasure response can be used to obtain a distance-time graph of the evolving detonation.

Aside from the noise characteristics and linearity of the optical systems – the main topic of discussion throughout Sections 3 & 4 – the performance of this back-end electronic hardware is the most important element contributing to the total spatial and temporal resolution attainable.

In the context of detonation velocity sensing, the temporal resolution, spatial resolution and spatial precision of a measurement system are defined as follows:

**Temporal Resolution:** The smallest time interval between two successive readings of the signal power. This must be smaller than the duration of the event being measured.

**Spatial Resolution:** The smallest distance interval between two successive readings of the signal power. This is is primarily determined by the temporal resolution and the speed of the detonation. E.g. A probe being destroyed at a rate of 10 cm/s, measured with a detector that has a temporal resolution of 0.1 seconds will have a maximum spatial resolution of 1 cm.

**Spatial Precision:** The positional uncertainty attributed to each reading of the signal voltage. There are three main contributing factors to consider:

- *Spatial precision that is primarily limited by the smallest change in voltage that the electronic hardware can record.* E.g. A 10 cm probe, with a signal amplitude range of 10V→0V, measured on an oscilloscope that has a minimum voltage interval of 1V, will have a maximum spatial precision of ±0.5 cm.

- *Spatial precision that is primarily limited by signal noise.* E.g. A 10 cm probe, with a signal amplitude range of 10V→0V and a noise band of ±0.5V, will have a maximum spatial precision of ±0.5 cm.
- *Spatial precision that is primarily limited by the measurement setup.* E.g. if the total length or position of the measurement probe can only be known to a precision of ±0.5 cm, then the total measurement precision is also limited to ±0.5 cm.

To optimise the resolution and precision of detonation velocity measurements, a number of detector and DAQ characteristics need to be considered. These are discussed in the following sections.

### Detectors

For detonation velocity measurements, the three photodetector characteristics that are of primary concern are *bandwidth*, *noise-floor level* and *dynamic range*. The *bandwidth* of a photodetector indicates how quickly it can respond to changing optical input signals. Maximum voltage output from a detector is generally obtained when measuring DC optical signals, but it decreases for modulated signals of increasing frequency. The bandwidth of a detector is defined as the input signal frequency at which the output voltage has dropped to half (-3 dB) of the maximum and is typically given in Hertz (Hz).

This can be related to the rise (or fall) time of a detector by considering the Fourier transform of an impulse function. It is clear, in this case, that for a detector to resolve an ideal impulse function it must have an infinite bandwidth. Hypothetically, as the bandwidth of this detector is reduced from infinity, the leading (rising) and trailing (falling) edges of the impulse function cannot be fully resolved and are increasingly less steep in the detector output.

An approximation of the *rise time* for a photodetector with a bandwidth $\Delta\nu$ is

$$\tau_{rise} \approx \frac{0.35}{\Delta\nu}, \tag{2.1}$$

where $\tau_{rise}$ is the 10%–90% rise time – the minimum time it takes for the detector output to go from 10% to 90% in response to an impulse function [41]. As a figure of merit, a detectors temporal resolution, $r_\tau$, can be given as

$$r_\tau = \frac{1}{\Delta\nu}. \tag{2.2}$$

This is an approximation, because the bandwidth defines the signal frequency at which the detector output voltage is half of its maximum – signals which vary faster than this

can still be detected, but with an increasingly reduced voltage response. In any case, the bandwidth is a very useful property to consider when choosing an appropriate detector for a detonation velocity system.

If a 10 mm long detonation velocity probe is entirely destroyed by a steady-state detonation front, travelling at 10 mm/$\mu$s, the signal power reaching the detector will fall from 100%→0% in 1 $\mu$s. This is a rate of change equivalent to a 500 kHz full cycle and should, therefore, be measured using a detector which has a bandwidth exceeding 500 kHz. If variations on the mm scale need to be measured, the detector bandwidth should exceed 5 MHz, and so on.

The *noise-floor* of a photodetector is characterised by the *noise-equivalent power* (NEP) and is a measure of the minimum resolvable optical input power. A detectors NEP depends upon the following characteristics [41]:

- **Current Noise ($I_N$)**: Current fluctuations measured on a photodetector in the absence of an optical input signal (measured in A/$\sqrt{\text{Hz}}$).
- **Responsivity ($R_\lambda$)**: The current generated in a photodetector per unit of optical input power (measured in A/W). It is dependant upon the wavelength of an incident optical signal.

The NEP of a detector is the optical input power which yields a signal-to-noise ratio of one for 1 Hz operation [41]:

$$\text{NEP} = \frac{I_N}{R_\lambda}. \tag{2.3}$$

To find the minimum optical input power that a detector can resolve, the NEP should be multiplied by the square root of the detector bandwidth,

$$\text{Minimum Resolvable Signal Power} = \text{NEP} \times \sqrt{\Delta\nu}. \tag{2.4}$$

For example, a 100 MHz detector with an NEP of 100 pW/$\sqrt{\text{Hz}}$ will have a minimum resolvable power of 1 $\mu$W.

For the detonation velocity measurements in this project, the smallest optical power signal that a detector can resolve is directly equivalent to the smallest length scale over which a shock-front can be monitored. If the initial signal power from a 10 mm long fibre optic probe were 10 $\mu$W, and a 100 MHz detector monitoring this signal had a noise floor of 1 $\mu$W, the shock-front position could be determined with a maximum precision of 1 mm.

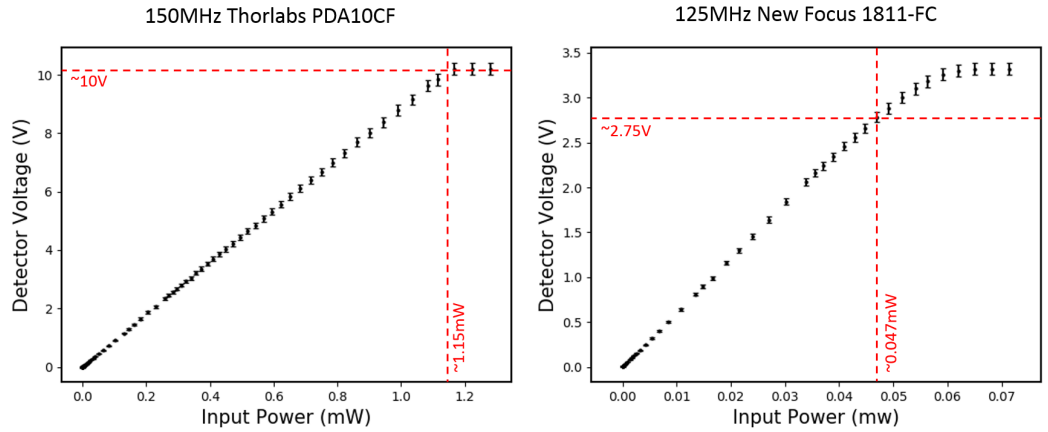


FIGURE 2.4: Plots showing the voltage response of two different photodetectors to a range of optical input powers.

If this detector, with a fixed NEP, were to make the same measurement at 1 MHz, the maximum precision would increase to 0.1 mm but the temporal resolution would be reduced by a factor of 100. Equations 2.2 & 2.4 represent this dichotomy, between a *fast* detector and a *sensitive* detector.

Finally, the *dynamic range* of a detector is determined by the *noise-floor level* and the *detector saturation level*. It describes the range of input powers that a detector can measure with good linearity – where the responsivity ($R_\lambda$) is independent of input power. It is usually given as a ratio in decibels (dB).

This is an important factor in the design of detonation velocity measurement systems for two reasons. First, analysis is simplified when voltage readings are linearly proportional to the optical power. Secondly, for maximum precision, the optical system (sources, reflective elements, filters, insertion losses etc.) should be designed to exploit the full extent of the dynamic range.

For example, a detector with a 10 mW (10 dBm) saturation level and a 0.001 mW (-30 dBm) noise floor level has a dynamic range of 40 dB. A 10 mm long velocity probe, with an initial signal power of 10 mW can be measured using this detector with a maximum precision of 1 $\mu$m – making full use of the 40 dB dynamic range. If the optical setup can only manage an initial power of 0.1 mW (-10 dBm), the maximum precision reduces to 100 $\mu$m – utilising only 20 dB of the available range.

In this project, two different detectors were used: *Thorlabs 150 MHz InGaAs PDA10CF* and *New Focus 125 MHz InGaAs 1811-FC*. In order to test the linearity and saturation level of these detectors, a variable attenuator was used to subject each one to a range of signal powers from a 1550 nm laser diode. The results are shown in Figure 2.4.

In both plots the detector saturation is visible and the approximate saturation point has been marked by two red dashed lines. For the Thorlabs detector, the output voltage plateaus at approximately 10 V for input powers $>$ 1.15 mW (0.6 dBm). In the case of

the New Focus detector, the output voltage undergoes a more gradual roll-off, starting at approximately 2.75 V for input powers $> 47$ $\mu$W (-13.3 dBm).

The NEP for the Thorlabs detector is given as 12 pW/$\sqrt{\text{Hz}}$ for a 1590 nm incident signal [42]. From Equation 2.4, this corresponds to a noise-floor level of 0.15 $\mu$W (-38 dBm) at 150 MHz operation. For the New Focus Detector, the NEP is given as 22.5 pW/$\sqrt{\text{Hz}}$ [43] (unspecified wavelength), which corresponds to a 0.25 $\mu$W (-36 dBm) noise-floor level at 125 MHz operation. Therefore, the dynamic range of each detector is approximately 39 dB and 23 dB, respectively.

### Oscilloscopes and DAQs

Oscilloscopes and DAQs are used to monitor and permanently store the time-varying voltage output from a detector (throughout this section, both devices are referenced by the abbreviation DAQ). These devices sample the voltage at discrete time intervals and then quantise the readings into a set of voltage "bins" based on the available *bit-depth*. These two processes have a considerable effect on the spatial and temporal resolution of a detonation velocity probe.

The bandwidth of a DAQ has a considerable effect upon the temporal resolution of the final results. It is a similar quantity to the aforementioned photodetector bandwidth – the input voltage frequency at which the DAQs amplitude reading has fallen to half (-3dB) of the input amplitude. Like a detector, the bandwidth of an oscilloscope should exceed the frequency of the signal it is attempting to measure.

Quantisation of an input signal voltage is carried out using an *analogue-to-digital converter* (ADC). The sampling rate of these devices contributes to the total bandwidth of the oscilloscope and the bit-depth determines the maximum number of voltage "bins". Typical bit-depths for DAQs are 8bit, 10bit and 12bit, which correspond to 256, 1024 and 4096 voltage bins, respectively.

To infer the position of a detonation front to a high precision, a high number of voltage bins is preferable. However, the bit-depth alone does not determine the voltage precision. Depending on the levels of noise intrinsic to the DAQs hardware, there may be several voltage bins which become degenerate. This degeneracy can be used to reconsider the number of useful voltage bins and define the *effective number of bits* (ENOB). The ENOB for a DAQ is always less than the bit-depth of its ADC.

For this project, a National Instruments PXIe-5160 was the chosen DAQ system. The maximum bandwidth of this system is 500 MHz, with a sampling rate up to 2.5 GSamples/s. The ADC has a bit-depth of 10 bits and the ENOB is specified as 7.1–7.6 for input signals up to 100 MHz.

## 2.3 Summary

In order to compare multiple fibre optic velocity probes, a test setup was required that could assess both the probe linearity and the signal-to-noise characteristics of each. To this end, the nitromethane copper cylinder test was designed, with a specially made lid for simultaneous implementation of multiple probes.

A summary of the crucial design elements of this test are given below:

- The fibre probes can be easily embedded into the explosive medium.
- The detonation velocity of nitromethane exceeds the sound speed in standard single-mode fibre.
- Established velocity measurement techniques can be tested alongside new methods.
- The tests are conducted in a region where the detonation is anticipated to have reached a steady state.

Furthermore, a discussion on the appropriate use of back-end electronic hardware lead to the following conclusions:

- For an oscilloscope or detector, the bandwidth is a figure of merit, quantifying the approximate temporal resolution that is attainable in detonation velocity measurements.
- A higher bandwidth signifies a higher potential temporal resolution, but also a higher noise floor level.
- The effective number of bits (ENOB) for an oscilloscope is a limiting factor for the spatial precision of a detonation velocity measurement.
- The dynamic range of a detector is a significant factor in determining the best case signal-to-noise ratio for a measurement system — it is directly related to the spatial precision/uncertainty.

# Chapter 3

# Fibre Bragg Grating Probes

This section introduces fibre Bragg gratings (FBGs) and how they can be used as detonation velocity sensors. To start with, a general conceptual and theoretical background is given, where the crucial characteristics of an FBG are introduced. Sections 3.2 and 3.3, which follow, discuss a recently optimised chirped FBG detonation velocity measurement technique and a novel uniform FBG detonation velocity measurement technique.

## 3.1 Background

An FBG is a wavelength filtering element, that exists within the core of an optical fibre. It consists of a periodic refractive index (RI) perturbation, that is resonant for a specific band of input wavelengths. If an incident optical signal is within the resonant bandwidth of an FBG, it will undergo a reversal in propagation direction due to an accumulation of phase matched Fresnel reflections. The extent to which this occurs is called the *reflectivity* or the *diffraction efficiency* and depends on both the specific design of the FBG and the exact signal wavelength [15].

Beyond these basic properties, which are generally descriptive of all FBGs, a considerable variety of FBGs may be fabricated which have different lengths, filter shapes, reflectivities and dispersion characteristics.

### 3.1.1 Uniform fibre Bragg Gratings

A *uniform* FBG (UFBG) is a periodic refractive index structure that has a fixed periodicity and amplitude along its entire length. In this case, optimal phase matching occurs at a single wavelength — the *Bragg wavelength* ($\lambda_B$)— which corresponds to a peak in the reflectivity ($R_{peak}$).

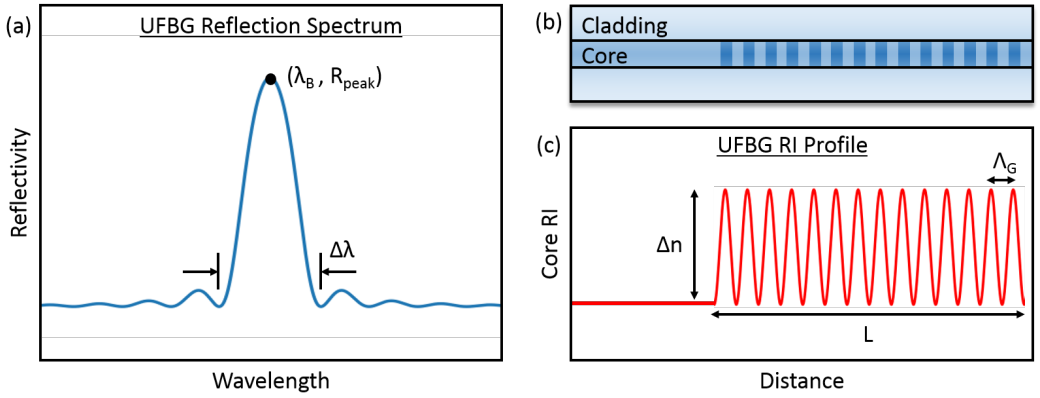


FIGURE 3.1: (a) A reflection spectrum typical of a uniform FBG. (b)- (c) An illustration of how the refractive index may vary in an optical fibre to form a uniform FBG.

Figure 3.1 (a) shows a UFBG reflection spectrum, where the Bragg wavelength and peak reflectivity are labelled by the point ($\lambda_B$, $R_{peak}$). Figures 3.1 (b) and (c) illustrate the refractive index change for a UFBG, where the constant periodicity, $\Lambda_G$, and the constant modulation amplitude, $\Delta n$, are labelled.

As seen in Figure 3.1 (a), the reflection spectrum for a UFBG is *sinc* shaped and has a finite bandwidth, $\Delta\lambda$, despite the fact that the structure is only fully phase matched at the Bragg wavelength. Conceptually, this is due to the uncertainty principle for a periodic structure of finite length — as the grating length, $L$, is increased, the Bragg wavelength is increasingly well defined and the bandwidth, $\Delta\lambda$, becomes narrower.

For an FBG of finite length, incidental phase matching can also occur at a variety of out-of-band wavelengths. This results in the existence of side-lobes, which can be seen as a periodic ripple in the reflection spectrum, Figure 3.1 (a). Furthermore, for refractive index patterns which are non-sinusoidal (e.g. akin to a square-wave), multiple Bragg peaks may emerge which correspond to the non-fundamental wavelength components.

The peak reflectivity, $R_{peak}$, of a UFBG is determined by the refractive index modulation, $\Delta n$, and by the number of grating periods, $\frac{L}{\Lambda_G}$. For an FBG with a very high RI modulation, the effective number of grating periods (and hence the effective length, $L_{eff}$) is reduced, because incident signals cannot fully penetrate the structure. As a result, the grating bandwidth will be broader than a lower reflectivity grating of the same total length.

In order to quantify the grating parameters shown in Figure 3.1 and design FBGs for various fibre optic systems, a more analytical approach is required. A popular method, and the one adopted in this report, is to use coupled-mode theory to produce a pair of differential equations that characterise the amplitude evolution of a counter-propagating mode from a periodically perturbed waveguide.

A thorough evaluation of coupled-mode theory can be found throughout literature [44, 45, 46], however, it is Kashyap's notation that is primarily used in this report [47].

### *Coupled-Mode Theory*

In general, coupled-mode theory is used to quantify the transfer of energy between two or more resonant modes in a system. In fibre optics, for example, a transverse mode may couple between multiple adjacent cores — the mechanism exploited in a fibre optic *coupler*.

For an FBG, orthogonal modes that are counter-propagating can begin to couple if the periodic phase modulation imparted by the grating meets the necessary resonance conditions. As an example, we consider the coupling of two counter-propagating modes (wavelength, $\lambda$), which are identical aside from their direction of travel (in $\pm z$ direction). The difference between the propagation constants ($\beta_{1,2}$) of the two modes is,

$$\begin{aligned} \delta\beta &= \beta_1 - \beta_2 \\ &= \frac{2\pi n_{eff}}{\lambda} - (-\frac{2\pi n_{eff}}{\lambda}) \\ &= \frac{4\pi n_{eff}}{\lambda}, \end{aligned} \tag{3.1}$$

where $n_{eff}$ is the effective refractive index.

If a periodic structure is introduced, such that the deficit, $\delta\beta$, between the two modes is accounted for, then the two modes will become resonant and the system is said to be *phase-matched*. For an FBG with a periodicity, $\Lambda_G$, phase-matching occurs at the Bragg wavelength, $\lambda_B$, when

$$\begin{aligned} \frac{2\pi}{\Lambda_G} &= \delta\beta \\ &= \frac{4\pi n_{eff}}{\lambda_B}, \end{aligned} \tag{3.2}$$

leading to the well-known Bragg condition,

$$\lambda_B = 2n_{eff}\Lambda_G. \tag{3.3}$$

Coupled-mode theory can now be applied to find the amplitude and phase characteristics of each mode as it interacts with the FBG. As before, the total electric field, $E(x, y, z)$, in

the fibre is assumed to consist of two identical counter-propagating modes (with mode-field distribution $\xi(x, y)$), which have slowly varying and complex amplitudes $A(z)$ and $B(z)$,

$$E(x, y, z) = \frac{1}{2}(A(z)\xi(x, y)e^{i(\omega t-\beta z)} + B(z)\xi(x, y)e^{i(\omega t+\beta z)}). \tag{3.4}$$

To find solutions for $A(z)$ and $B(z)$, the electric field, $E$, can be substituted into Maxwell's wave equation, which can be modified to include a periodic refractive index pattern. For simplicity, the perturbation is assumed to be sinusoidal and of a fixed periodicity — corresponding to a uniform grating. It is given by Kashyap [47] in terms of an additional polarisation term, $P_{pert}$,

$$P_{pert}(x, y, z) = 2n\varepsilon_0\big[\overline{\Delta n} + \frac{\Delta n}{2}e^{i(\frac{2\pi}{\Lambda_G}z)}\big]E(x, y, z), \tag{3.5}$$

where $\varepsilon_0$ is the vacuum permitivity and $n$, $\overline{\Delta n}$ and $\Delta n$ are the refractive index of the core, average refractive index change and maximum refractive index change respectively.

This polarisation term is appended to Maxwell's wave equation to get,

$$\nabla^2 E = \mu_0\varepsilon_0\varepsilon_r\frac{\partial^2 E}{\partial t^2} + \mu_0\frac{\partial^2 P_{pert}}{\partial t^2}, \tag{3.6}$$

where $\mu_0$ is the vacuum permeability and $\varepsilon_r$ is the relative permittivity.

The substitution and rearrangement of Equations 3.4-3.6 eventually leads to the coupled-mode equations [47],

$$\frac{\partial B(z)}{\partial z} = i\kappa_{dc}B(z) + i\kappa_{ac}A(z)e^{-i\Delta\beta z}, \tag{3.7}$$

$$\frac{\partial A(z)}{\partial z} = -i\kappa_{dc}A(z) - i\kappa^*_{ac}B(z)e^{i\Delta\beta z}, \tag{3.8}$$

where $\kappa_{ac}$ and $\kappa_{dc}$ are the so-called coupling coefficients. These coefficients contain the refractive index perturbation and an overlap integral with the forward and backward propagating mode fields. They can be evaluated and re-written in the form,

$$\kappa_{ac} = \frac{v\pi\Delta n_{eff}}{\lambda}, \tag{3.9}$$

$$\kappa_{dc} = \frac{2\pi\Delta n_{eff}}{\lambda}, \tag{3.10}$$

where $v$ is the visibility and $\Delta n_{eff}$ is the RI modulation amplitude, $\Delta n$, multiplied by the fraction of modal power in the core, $\eta$ [47].

The $\Delta\beta$ term corresponds to the phase matching condition between the forward and backward propagating modes (Equations 3.1 and 3.2) and is given as,

$$\Delta\beta = \delta\beta - \frac{2\pi}{\Lambda_G}. \tag{3.11}$$

When $\Delta\beta$ is zero, the modes are phase matched and the mode-coupling is maximised. If a forward propagating mode, amplitude $A(z_0) = 1$, interacts with a grating at its resonant frequency, then a backward propagating mode will emerge due to the coupling $\frac{\partial B(z_0)}{\partial z} = i\kappa_{ac}$.

### *Uniform FBG Characteristics*

Now that the coupled-mode equations have been found, it is possible to predict the spectral characteristics of a uniform FBG based on its length, periodicity and RI modulation amplitude.

In order to find the reflectivity of a uniform FBG at an arbitrary wavelength, Equations 3.7 and 3.8 can be rearranged and solved to find the ratio of input wave amplitude and reflected wave amplitude,

$$\rho = \frac{-\kappa_{ac}\sinh(\alpha L)}{\delta\sinh(\alpha L) - i\alpha\cosh(\alpha L)}, \tag{3.12}$$

where $\rho$ is the reflectivity amplitude coefficient, $\alpha = \sqrt{|\kappa_{ac}|^2 - \delta^2}$, $\delta = \kappa_{dc} + \frac{\Delta\beta}{2}$ is the detuning and $L$ is the grating length [47].

The peak reflectivity corresponds to a detuning of $\delta = 0$, which gives,

$$\rho_{max} = tanh(\kappa_{ac}L), \tag{3.13}$$

$$R_{peak} = |\rho|^2_{max} = tanh^2(\kappa_{ac}L), \tag{3.14}$$

where the amplitude reflectivity has been squared to give the peak *power* reflectivity, $R_{peak}$.

Moreover, by using Equation 3.12 to find the first reflection minimum, the grating bandwidth can be found. This equates to minimising the sinh term, by setting $\alpha L = i\pi$, and rearranging to give a grating bandwidth of [47],

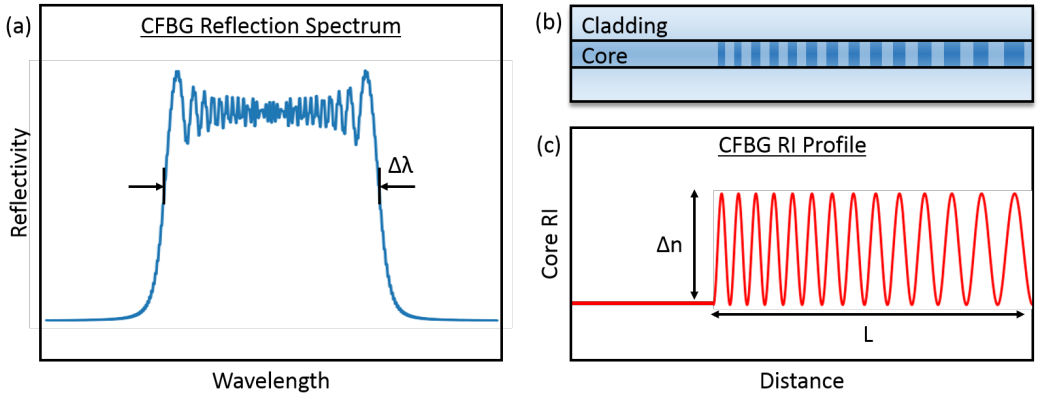


FIGURE 3.2: (a) A reflection spectrum typical of a chirped FBG. (b)- (c) An illustration of how the refractive index may vary in an optical fibre to form a chirped FBG.

$$\Delta\lambda = \frac{\lambda_B^2}{\pi n_{eff}} \sqrt{\kappa_{ac}^2 + \left(\frac{\pi}{L}\right)^2}. \tag{3.15}$$

Equations 3.14 and 3.15 reinforce the assertions made in Section 3.1.1 regarding the Fourier properties of gratings. For gratings with a low refractive index contrast, the bandwidth is dominated by the length, $L$, of the grating, which tends towards a delta function as the length approaches infinity. For gratings with a high refractive index contrast, the incident signal only "sees" a limited portion of the grating and, hence, the bandwidth is dominated by the $\kappa_{ac}$ term.

### 3.1.2 Non-Uniform FBGs

There are two fundamental ways in which an FBG may be non-uniform. First, the RI modulation period, $\Lambda_G$, can vary along the length of the grating, $\Lambda_G(z)$. In this case, the grating has a continuous spectrum of Bragg wavelengths and is said to be "*chirped*". Figure 3.2 (a) shows the reflection spectrum of an FBG that has a monotonic and linearly increasing grating pitch — a *linearly chirped grating* (CFBG).

The reflection spectrum of a CFBG does not have a single Bragg peak, like a UFBG, but oscillates around a fixed average reflectivity, giving it an approximately square-shaped profile in comparison. Furthermore, the bandwidth, $\Delta\lambda$, of a CFBG can be arbitrarily broad, because each successive grating period is resonant with a unique signal wavelength. The rate of change in Bragg wavelength over a specific section of an FBG is called the *chirp-rate* and is typically given in units of nm/cm.

Similar to Equation 3.14 for a UFBG, the reflectivity profile of a CFBG can be calculated using the formula,

$$TL(z) = (\eta(z) \cdot \Delta n(z))^2 \cdot \frac{1.478}{|CR(z)|}, \tag{3.16}$$

where $\eta(z)$ is the fraction of modal power in the core, $\Delta n(z)$ is the refractive index modulation amplitude (in units of $10^{-4}$) and $CR$ is the chirp-rate (nm/cm) [48]. $TL(z)$ is the transmission loss in decibels (dB) and is related to the linear grating reflectivity in the following way,

$$R(z) = 1 - 10^{-\frac{|TL(z)|}{10}}. \tag{3.17}$$

The other way in which an FBG may be non-uniform, is by having an RI modulation amplitude, $\Delta n$, which varies along the length of the grating, $\Delta n(z)$. For a UFBG with a low peak reflectivity ($R_{peak} < 50\%$), the shape of the reflection spectrum will be similar to the Fourier transform of the RI profile, $\Delta n(z)$.

For filtering applications, the oscillations in Figure 3.2 (a) and/or the side-lobes in Figure 3.1 (a) can be minimised by tapering the RI modulation at either end of the grating [46]. This is an FBG design feature known as *apodisation*.

### 3.1.3 FBG Fabrication

In this section, a brief outline of various FBG fabrication methods is given. This leads on to a description of the specific fabrication method used throughout this project, to make uniform FBGs and FBG arrays.

#### *Background*

There are two fundamental mechanisms required in the fabrication of FBGs: **(1)** A way to alter the RI in the core of an optical fibre; **(2)** A way to make these RI alterations periodically.

In a step-index optical fibre, the RI of the core is raised relative to the RI of the cladding, so that total internal reflection can occur. This is often achieved by doping the core with germanium to produce germanosilicate — a glass with a slightly increased RI, dependent on the dopant concentration. A side-effect of this process is that germanosilicate, and hence the core of many standard optical fibres, is *photosensitive*. Photosensitivity is the property of a material to undergo permanent changes in its local refractive index, when exposed to light of a specific wavelength and/or intensity [49]

This was first observed in optical fibres by Hill et al. [15], who launched a 488 nm argon-ion laser into a germanosilicate core. Fresnel reflections from the end facet of the fibre

set up a standing wave pattern and the first 'Hill Grating' was created. Subsequent optimisation of the photosensitive effect found that germanosilicate was particularly sensitive to radiation at around 244 nm [50], coinciding with a GeO absorption peak [51]. It was also realised that, due to the transparency of the silica cladding at this wavelength, the RI of the core could be affected through the side of the fibre [52].

There are several ways to exploit this effect, in order to create periodic refractive index patterns in the core. These can be loosely categorised as either *holographic* or *point-by-point* methods.

Holographic methods use wave interference to create a periodic UV intensity pattern in free-space. FBGs are then formed by exposing the photosensitive core of an optical fibre to this intensity pattern, where each UV intensity peak produces a local peak in the RI. Two popular holographic methods are the two-beam interference method and the phase mask method.

In the two-beam interference method, a periodic UV intensity pattern is created by overlapping two UV beams at a fixed angle [52]. At the point where the two beams intersect, an intensity pattern is formed with a periodicity,

$$\Lambda = \frac{\lambda_{uv}}{2\sin(\frac{\theta}{2})}, \tag{3.18}$$

where $\lambda_{uv}$ is the UV source wavelength and $\theta$ is the angle between the two beams [53]. This method requires precise alignment, but allows the FBG periodicity to be tuned over a huge range — for a 240 nm UV source, the FBG could theoretically be tuned to any pitch >240 nm.

In the phase mask method, a periodic UV intensity pattern is created by overlapping the $\pm 1$ diffraction orders from an appropriately designed, zero-order-nulled phase grating. The resultant intensity pattern has a periodicity of,

$$\Lambda = \frac{\Lambda_{pm}}{2}, \tag{3.19}$$

where $\Lambda_{pm}$ is the pitch of the phase grating. In this case, the pitch tuning range is very limited in comparison to the two-beam interference method, but it is considerably simpler to setup and very repeatable [50].

Point-by-point methods of FBG fabrication use a single laser source to locally modify the RI of the core, one grating interface at a time. A periodic structure is produced by modulating the laser intensity as the fibre is mechanically moved in increments of the grating pitch, $\Lambda_G$.

This method requires a level of sophistication above that of the holographic methods, because the laser modulation and the mechanical control of the fibre must occur synchronously and with great precision. However, point-by-point methods allow an extreme level of control — building a grating plane by plane means that an arbitrarily complex phase and amplitude pattern can be achieved [54].

### *UFBG and UFBG Array Fabrication*

For this project, a simple phase-mask setup was assembled in order to fabricate UFBGs and UFBG arrays. High chirp-rate CFBGs were also fabricated using this setup, but were later rejected due to their low-reflectivity profile (often below 10%).

A diagram of the setup is shown in Figure 3.3, and worked in the following way:

1. A frequency quadrupled Nd:YAG laser (266 nm) was reflected from two mirrors and focused by a cylindrical plano-convex lens.
2. The beam was initially directed towards the wall of an aperture.
3. Behind the aperture was a 10 mm phase mask and an un-coated optical fibre, which was mounted so that it was perpendicular to the direction of the beam.
4. The phase-mask was aligned so that its back face (relative to the direction of the laser) was as close as possible to the fibre (<0.5 mm away).
5. The second mirror, which was mounted on a translatable stage, was then moved by approximately 10 mm in the y-direction so that the beam would sweep across the phase mask and stop again on the opposite wall of the aperture.

The fabrication of the FBG occurs when the UV source is swept past the phase mask. Therefore, to increase/decrease the reflectivity of the resultant grating, the exposure time could be adjusted by changing the sweep speed of the second mirror.

Furthermore, the required exposure time could be decreased if the fibre had been *hydrogen-loaded* prior to UV exposure. Hydrogen loading is a process where the photosensitivity of a fibre is heightened by storing it in a high pressure hydrogen-filled container [55]. In this case, the fibres were stored at 60°C in ∼120 bar hydrogen for 7–10 days.

To write a UFBG with a reflectivity of 20–30% in hydrogen-loaded Fibrecore PS1250/1500, a sweep speed of around 1 mm/s was sufficient. This was with the UV source set to an average power of ∼12mW and a beam cross-section of approximately 0.4 $mm^2$ (0.9 mm × 0.6 mm in diameter). The source was also pulsed, with a 20Hz repetition rate and a fluence of ∼140 $mJ/cm^2$/pulse — appropriate settings for the writing of Type-I FBGs [49].

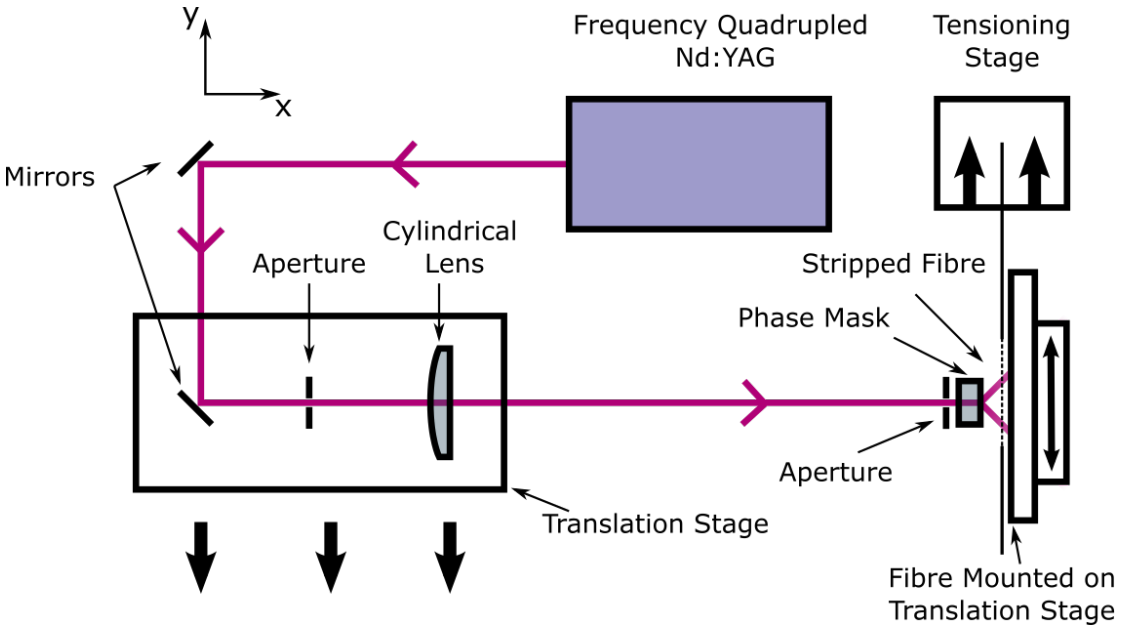


FIGURE 3.3: A diagram showing the setup used to fabricate UFBGs and UFBG arrays for the UFBG detonation velocity probes.

As an extension to the basic setup, another translatable stage and a tensioning dynamometer were added to the fibre mounting platform. This allowed for the fabrication of UFBG arrays which were evenly spaced in wavelength and position. The additional steps, in this case, were:

1. After the fabrication of the first grating, the *fibre* stage was translated in the y-direction by at least 10 mm. whilst the laser remained incident upon the aperture wall.
2. The tensioning stage was then used to strain the fibre by a fixed amount, depending on the wavelength separation required.
3. The second mirror could be moved again (see point 5 above) to sweep back across the phase mask and write a second FBG.

This process was repeated several times, to create UFBG arrays that consisted of 5–6 gratings, separated by 3 mm and with a 0.8 nm wavelength spacing.

### 3.1.4 FBG Simulations - Transfer Matrix Method

For measurements of detonation velocity, it is especially crucial that the response of an FBG to changes in *length* — its *"erasure characteristics"* — are well characterised. In order to predict the erasure characteristics of an FBG, a simulation method is required, where the grating period, $\Lambda_G(z)$, refractive index profile, $\Delta n(z)$, and length, $L$, can be specified to give the grating reflectivity as a function of wavelength, $R(\lambda)$.

For this purpose, the simulations in this project utilise the *transfer-matrix (T-matrix)* method [47][56][57], implemented in the *Python* programming language.

The T-matrix method fundamentally relies on the principle that uniform, chirped or apodised gratings can be modelled as a concatenation of short uniform sub-gratings. If the sub-gratings are sufficiently small in comparison to any variations in the grating properties ($\Lambda_G(z)$ or $\Delta n(z)$), then an accurate digitized version of the full grating can be created by varying the characteristics of each sub-grating.

The general form of the T-matrix, for a single sub-grating, is as follows,

$$\begin{bmatrix} R_{in}(\rightarrow) \\ S_{out}(\leftarrow) \end{bmatrix} = \begin{bmatrix} T_{11} & T_{12} \\ T_{21} & T_{22} \end{bmatrix} \begin{bmatrix} R_{out}(\rightarrow) \\ S_{in}(\leftarrow) \end{bmatrix}, \tag{3.20}$$

where the $R$ and $S$ components are the optical mode amplitudes entering and leaving the grating at either end and the $T_{nm}$ elements represent the sub-grating characteristics [47]. For a normalised input signal, $R_{in} = 1$, and assuming no input signal from the far-end, $S_{in} = 0$, we get a reflected mode amplitude that is $S_{out} = \frac{T_{21}}{T_{11}}$.

By assuming that each sub-grating is uniform, the matrix elements $T_{mn}$ can be determined by solving the coupled-mode equations (Equations 3.7–3.8) to get,

$$T_{11} = \cosh(\alpha \Delta L) - \frac{i\delta \sinh(\alpha \Delta L)}{\alpha} \tag{3.21}$$

$$T_{22} = \cosh(\alpha \Delta L) + \frac{i\delta \sinh(\alpha \Delta L)}{\alpha} \tag{3.22}$$

$$T_{12} = -\frac{i\kappa_{ac} \sinh(\alpha \Delta L)}{\alpha} \tag{3.23}$$

$$T_{21} = \frac{i\kappa_{ac} \sinh(\alpha \Delta L)}{\alpha}, \tag{3.24}$$

where $\Delta L$ is the sub-grating length, $\alpha = \sqrt{|\kappa_{ac}|^2 - \delta^2}$ and $\delta = \kappa_{dc} + \frac{\Delta\beta}{2}$ [47].

It is then straight forward to simulate a concatenation of $N$ sub-gratings by multiplying a T-matrix for each one of them in the following way,

$$\begin{bmatrix} R_{in}(\rightarrow) \\ S_{out}(\leftarrow) \end{bmatrix} = \begin{bmatrix} T^1_{11} & T^1_{12} \\ T^1_{21} & T^1_{22} \end{bmatrix} \times \begin{bmatrix} T^2_{11} & T^2_{12} \\ T^2_{21} & T^2_{22} \end{bmatrix} \times ... \times \begin{bmatrix} T^N_{11} & T^N_{12} \\ T^N_{21} & T^N_{22} \end{bmatrix} \begin{bmatrix} R_{out}(\rightarrow) \\ 0 \end{bmatrix}. \tag{3.25}$$

Once a grating has been constructed in this manner, it is possible to simulate its erasure characteristics by removing one sub-grating matrix at a time and recording the reflected amplitude $S_{out}$ for a set of incident wavelengths.

## 3.2 Chirped Fibre Bragg Grating Probes

For the measurement of detonation velocity, FBG methods offer a low-profile, continuous, non-electrical and easy to implement alternative to the various techniques outlined in Section 1.3.2. These benefits are summarised as follows:

- **Low-Profile:** The cross-sectional area of a standard optical fibre (125 $\mu$m diameter) is just 0.012 mm$^2$. This allows an FBG sensor to be directly embedded into an explosive with minimal invasiveness.
- **Continuous:** The theoretical limit on spatial resolution, for an FBG detonation velocity sensor, is the grating period, $\Lambda_G$. This length is usually considerably shorter than the total sensor length, $\Lambda_G << L$, such that the measurement can be considered continuous.
- **Non-Electrical:** Fibre optic sensors are insensitive to electrical noise and safe to use where electrical wires are undesirable.
- **Simple to Implement:** The mechanical flexibility of an optical fibre, as well as its continuous measurement capabilities, mean that attachment is simple compared to discrete methods, where the measurement accuracy is limited by the alignment precision during setup.

Conceptually, FBGs can be used as detonation velocity sensors because their spectral characteristics are *length dependant*. Assuming that an embedded fibre will be near-instantaneously destroyed by a traversing detonation shock-front, the timewise position of this shock-front can be determined by monitoring the FBG reflection spectrum.

In this project, both uniform and chirped FBGs are used to measure detonation velocity. In each case, the spectral response of the grating is different and a different interrogation setup is required.

In this section, the use of CFBGs as detonation velocity sensors is explored. First, the basic concepts from literature are discussed in relation to the FBG properties introduced in Section 3.1.2. After this, a more in-depth look at CFBG behaviour, using the T-matrix method (Section 3.1.4), is used to highlight some undesirable non-linear CFBG characteristics which may degrade velocity measurement accuracy. Finally, experimental data is shown and analysed in order to demonstrate the optimal CFBG design criteria for detonation velocity measurements [58].

### 3.2.1 Concept

A CFBG has a continuum of resonant (Bragg) wavelengths, which each correspond to a specific spatial position along the grating length. In this way, a CFBG can be utilised as a *bandwidth - length* transducer, where the chirp-rate is a constant of proportionality,

$$\Delta\lambda(t) = CR \times L(t). \tag{3.26}$$

If a CFBG is subjected to a continuous change in length — due to destruction by a shock-front, in this case — the rate of change in length is related to the rate of change of bandwidth as follows,

$$\frac{d}{dt}[\Delta\lambda(t)] = CR \times \frac{dL(t)}{dt}. \tag{3.27}$$

Equation 3.27 shows that, for a CFBG embedded in an explosive and with a known chirp-rate, the detonation velocity, $D = \frac{dL(t)}{dt}$, can be inferred as long as the reflection bandwidth can be monitored. The practical difficulty, in this case, is how to measure the bandwidth at sufficient speed to be able to resolve the shockwave propagation, when the detonation velocity, $D$, can reach in excess of 10 km/s.

At such high speeds, the sampling rate of a conventional spectrum analyser is too low, requiring that the CFBG bandwidth be monitored by some other means. The two methods adopted so far in literature are: **(1)** Inference of the bandwidth by measuring the integrated reflected power [11, 29, 31, 32]; **(2)** Measurement of the bandwidth via dispersion induced time-streak [35].

In this project, the integrated power method is adopted, primarily due to its simpler and cheaper construction. Figure 3.4 shows the typical setup used for CFBG detonation velocity measurements, utilising the integrated power measurement scheme. In this case, a broadband (incoherent) amplified spontaneous emission source (ASE) is used to illuminate the full bandwidth of a CFBG, with the reflected signal sent to a photodetector via an optical circulator. Due to the availability of high-speed photodetectors and oscilloscopes, this system is capable of measurement speeds in the GHz range — easily enough to achieve sub-millimetre spatial resolutions.

In general, for an ASE source with a power spectral density (PSD), $S_{psd}(\lambda)$, illuminating a CFBG with reflectivity, $R(\lambda)$, the total reflected power reaching a photodetector will be,

$$P = \int_{\lambda_{start}}^{\lambda_{end}} S_{psd}(\lambda) \cdot R(\lambda) \cdot d\lambda, \tag{3.28}$$

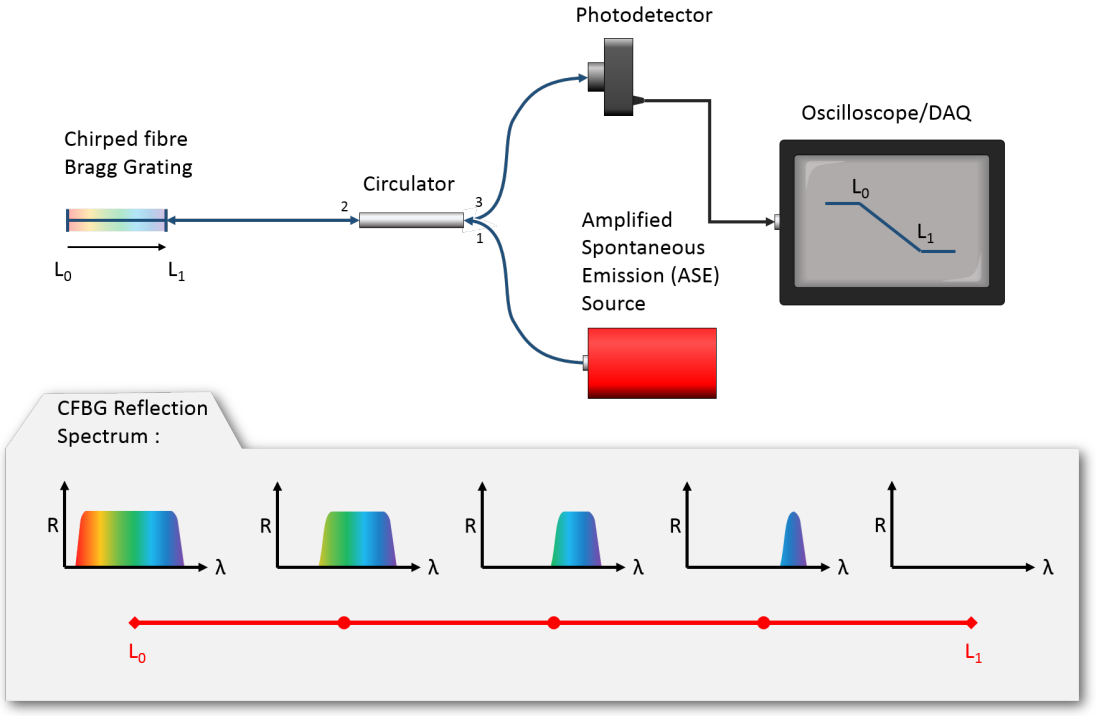


FIGURE 3.4: The typical setup used for CFBG detonation velocity measurements, utilising the integrated power measurement scheme.

where $\lambda_{start}$ and $\lambda_{end}$ are the bandwidth limits of the CFBG.

To demonstrate the equivalence of bandwidth, length and reflected power, we can consider a simplification to Equation 3.28, where the ASE source is perfectly gain-flattened, $S_{psd}(\lambda) = S_0$. In this model, the CFBG has a time varying length, $L(t)$, a chirp-rate, $CR$, and a lower wavelength limit, $\lambda_0$. If we further assume that the CFBG spectrum is rectangular, with a constant reflectivity, $R(\lambda) = R_0$, then the reflected power reaching the detector is,

$$\begin{aligned} P(t) &= \int_{\lambda_0}^{\lambda_0 + L(t) \cdot CR} S_0 \cdot R_0 \cdot d\lambda, \\ &= L(t) \cdot CR \cdot R_0 \cdot S_0, \end{aligned} \tag{3.29}$$

and, therefore,

$$\frac{P(t)}{P(t_0)} = \frac{L(t)}{L(t_0)}. \tag{3.30}$$

In this idealised case, Equation 3.30 shows that the relative change in reflected power reaching the photodetector, is directly equivalent to the relative change in CFBG length. This is essentially how the integrated power measurement scheme works, except that for

a non-rectangular $R(\lambda)$ and $S_{psd}(\lambda)$, an extra calibration step is required along the lines of Equation 3.28, so that the measured power, $P(t)$, can be compared to the expected power at a given CFBG length,

$$P(L) = \int_{\lambda_{start}(L)}^{\lambda_{end}(L)} S_{psd}(\lambda) \cdot R(\lambda, L) \cdot d\lambda. \tag{3.31}$$

In real-life cases, the precise determination of $R(\lambda, L)$ for a CFBG is non-trivial, because only two of the grating characteristics are known to the user: **(1)** The initial length of the grating, $L_0$; and **(2)** The initial reflection spectrum, prior to its destruction, $R(\lambda, L_0)$. However, in the next section, it is shown that $R(\lambda, L)$ can be approximated easily and with good accuracy for certain "optimised" CFBG designs.

### 3.2.2 Optimisation

By definition, a CFBG (linearly chirped FBG) is fabricated such that it has a linearly increasing Bragg resonance along its length. On this basis, it is reasonable to assume that the *bandwidth* of a CFBG is also linearly dependant on its length, as described by Equation 3.26. Using this assumption, the calibration standard, $P(L)$, can be obtained from the initial CFBG spectrum, $R(\lambda, L_0)$, as

$$P(L) = \int_{\lambda_0}^{\lambda_0 + L \cdot CR} S(\lambda) \cdot R(\lambda, L_0) \cdot d\lambda. \tag{3.32}$$

In this simplified case, a CFBG that has been erased down to its terminal grating plane will have a very narrow bandwidth (small $L \cdot CR$) — perhaps a factor of $10^{-5}$ times smaller than its original bandwidth.

However, this is clearly non-physical, because it is known from the simple Fourier arguments in Section 3.1.1 that a single grating plane constitutes a poorly defined resonant wavelength and hence has a very broad reflection bandwidth. Analytically, this is shown in Equation 3.15 for the bandwidth of a uniform FBG. In the case of a weak RI modulation, such that $\kappa_{ac}$ is negligible, this equation can be rearranged to give the minimum bandwidth limit for *any* FBG of length, $L$, as

$$\Delta\lambda = \frac{\lambda_B^2}{n_{eff}} \cdot \frac{1}{L}. \tag{3.33}$$

The implication of Equation 3.33 is that the linear bandwidth approximation, in Equation 3.26, will eventually break down at a length corresponding to the CFBGs transition into a uniform FBG. For a low RI modulation CFBG this transition will occur at a length,

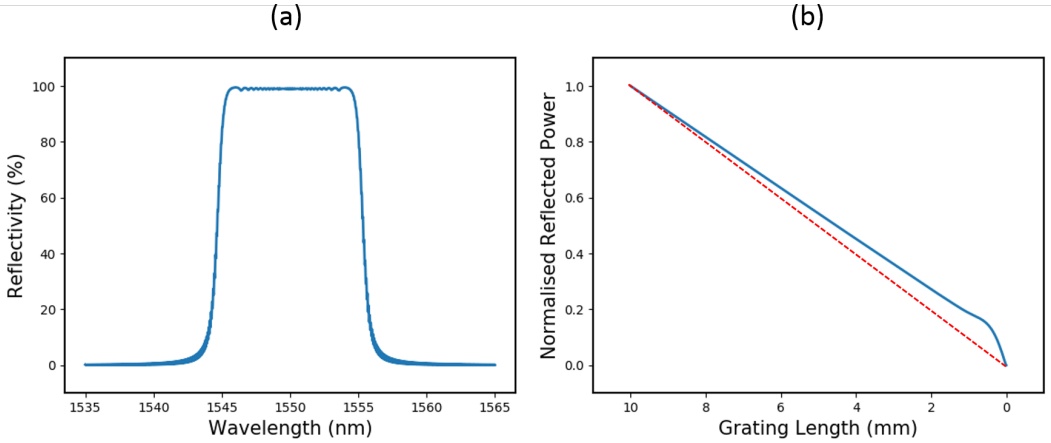


FIGURE 3.5: (a) Shows the simulated reflection spectrum of a 10 mm, 99% reflectivity, 10 nm bandwidth chirped grating. (b) Shows how the total reflected power reduces as the grating is destroyed. The power scales linearly until the final $\sim$ 1.5 mm, where it becomes non-linear. The dashed red line shows the ideal case, where reflected power is linearly proportional to grating length.

$$L_t = \frac{\lambda_B}{\sqrt{n_{eff} \cdot CR}}, \tag{3.34}$$

where $\lambda_B$ is an appropriate wavelength, somewhere within the CFBG bandwidth. This lower length limit will increase for CFBGs that have a non-negligible RI modulation and, hence, $R(\lambda, L)$ will diverge more quickly from the linear bandwidth approximation.

To illustrate this divergence, a T-Matrix simulation is shown in Figure 3.5 of a 10 mm long, 99% reflectivity, 10 nm bandwidth grating. Figure 3.5(a) shows the initial CFBG spectrum, which is then dismantled, one sub-grating at a time, and integrated to show the total reflected power at each stage. Figure 3.5(b) is a normalised plot of the reflected power as a function of length and is equivalent to the signal that would be measured by a photodetector during detonation — this represents an accurate form of the calibration standard, $P(L)$.

The dashed red line shows the *ideal* erasure signal, given by Equation 3.30. This line also corresponds closely to the function, $P(L)$, that would be obtained from the linear bandwidth approximation using Equation 3.32.

In Figure 3.5(b) it can be seen that, over the initial $\sim$85% of the CFBG erasure, the reflected power scales approximately linearly with grating length. Following this, at a length of approximately 1.5 mm, the CFBG begins its transition into the UFBG regime, where the erasure becomes distinctly non-linear.

In previous implementations of the CFBG detonation velocity method, the linear region of the erasure was assumed to uphold the proportionality relationship, Equation 3.30, and the detonation velocity was inferred from the gradient over this region. However,

there is a clear gradient offset between the ideal and simulated erasure, which in this case would result in a velocity error of around 8.7% if it were ignored.

For practical reasons, it is simpler to try and minimise this inherent non-linearity by optimising the specific CFBG design, than to attempt to accurately recreate a CFBG in a T-Matrix simulation, based solely on its initial spectrum. Essentially, the aim of this optimisation is to find CFBG designs that are congruent with the linear bandwidth approximation and allow an accurate calibration standard, $P(L)$, to be found from the method in Equation 3.32.

#### *Origin of the Non-Linearity*

So far, it has been established that, at a certain length, $L_t$, a CFBG will effectively become a UFBG due to the bandwidth limitation, Equation 3.33–3.34. This length is more commonly known as the *coherence length* of the grating structure and is approximately fixed for $\Delta\lambda << \lambda$. This means that every grating section of length, $L_t$, is effectively a UFBG in isolation and, hence, the non-linear region at the end of a CFBG erasure is not due to any kind of structural asymmetry i.e. it cannot be removed by cutting off one end of the grating.

Instead, the asymmetry that causes the gradient offset and non-linear power-drop is imposed on the CFBG once light is launched into either end. At this point, the signal power reflected from each UFBG length section is front-loaded with respect to the incident signal. Throughout most of the CFBG structure, the front-loaded power distribution averages out across the bandwidth and the power lost per unit length is approximately constant. This breaks down for the last remaining UFBG section, which receives the full, uninhibited, PSD of the source across its entire bandwidth.

Figure 3.6 shows the change in power per unit length for a 10 mm long, 10 nm bandwidth, 99% reflectivity CFBG. In this case, a significant spike in the reflected power is seen to come from the first ∼0.5 mm, before eventually converging to a constant power per length of ∼0.09 $\text{mm}^{-1}$.

This results in:

- **A non-linear power-drop at the end of the erasure:** because the power distribution over the last remaining UFBG section is non-uniform (i.e. between 1.5 mm and 0 mm in Figure 3.6).
- **A gradient offset:** because a disproportionate amount of power is reflected by the front-end spike. This is demonstrated in Figure 3.6, where the constant back-end region plateaus at approximately 0.09 $\text{mm}^{-1}$ — when the grating is half destroyed, the power has dropped by a factor $5 \times 0.9 = 0.45$.

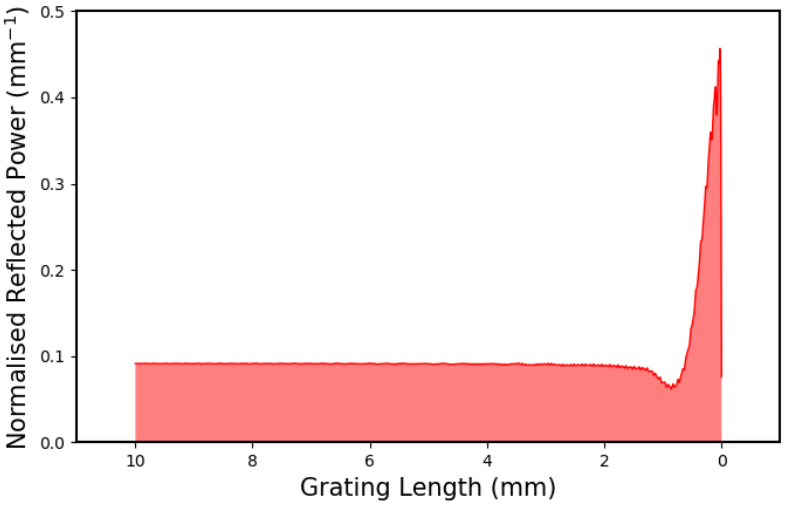


FIGURE 3.6: Graph showing the power distribution along the length of a 10 mm long, 10 nm bandwidth, 99% reflectivity CFBG. This is the differentiated power erasure (Figure 3.5(b)) and is, therefore, in units of mm$^{-1}$. The total power has been normalised so that the area under the entire curve is 1.

***Reduction of the Non-Linearity***

There are two ways to reduce the severity of these non-linear effects: **(1)** Shorten the coherence length of the grating in order to shrink the affected region; **(2)** Reduce the front-loading effect by increasing the *effective length* of each UFBG section.

In the simplified case of a negligible RI modulation, Equation 3.34 shows that the coherence length of a CFBG is inversely proportional to its chirp-rate. For a non-negligible RI modulation, a more general non-linear length can be found by substituting Equation 3.26 into Equation 3.15 and rearranging for $L$. Alternatively, Figure 3.7 shows a plot of the two equations for a variety of chirp-rates (3–20 nm/cm) and RI modulation amplitudes ($10^{-6}$–$10^{-3}$), where the intersection of the two lines indicates the length of the non-linear region (coherence length).

It is illustrated in Figure 3.7, using arrows, that a CFBG with a low RI modulation and a high chirp-rate will have a shorter non-linear region than a CFBG with a low chirp-rate and a high RI modulation. Over such an extreme variety of RI modulation amplitudes, it is also clear that the primary factor determining the length of the non-linear region is the chirp-rate. Therefore, in regards to the proposed solution **(1)** (above), the first CFBG design principle is:

> *A CFBG detonation velocity sensor should be designed with a high chirp-rate, to ensure a minimal non-linear length region.*

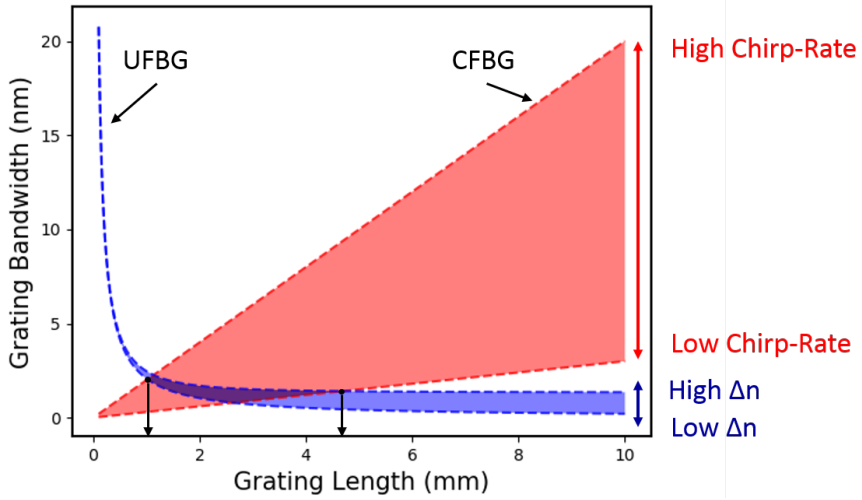


FIGURE 3.7: In blue: a plot of uniform grating bandwidth as a function of grating length over a range of index modulations. In red: a plot of chirped grating bandwidth over a range of chirp rates. For a CFBG with a specific chirp-rate and index modulation, the start of the non-linear region corresponds to the intersection of these two plots, where the CFBG transitions into a uniform grating.

The effective length (or *penetration depth*) of a UFBG is a figure of merit, quantifying the extent to which an incident signal is depleted as it travels through an FBG. As discussed in Section 3.1.1, a highly reflective UFBG may diffract a significant proportion of input light over the first quarter of the grating length, such that the signal only "sees" a much shorter FBG than actually exists. More specifically, the effective length is defined based on its group-delay [59] — for an FBG that is uniformly illuminated, the average delay time corresponds to an effective reflection point at the position, $z = \frac{L}{2}$, which is its effective length.

This is equivalent to the front-loading effect shown in Figure 3.6 and can, therefore, be used to optimise the CFBG design — over each UFBG section (most noticeably, the last remaining section), the effective length, $L_{eff}$, should be maximised so that it approaches half the non-linear length, $\frac{L_t}{2}$. This is equivalent to an ideally even power distribution.

Barmenkov et al. [59] define the effective length of a UFBG (at its Bragg wavelength) in terms of its reflectivity,

$$L_{eff} = \frac{L_t \cdot \sqrt{R}}{2\,\mathrm{atanh}(\sqrt{R})}, \tag{3.35}$$

$$\frac{L_{eff}}{L_t} = \frac{\sqrt{R}}{2\,\mathrm{atanh}(\sqrt{R})}, \tag{3.36}$$

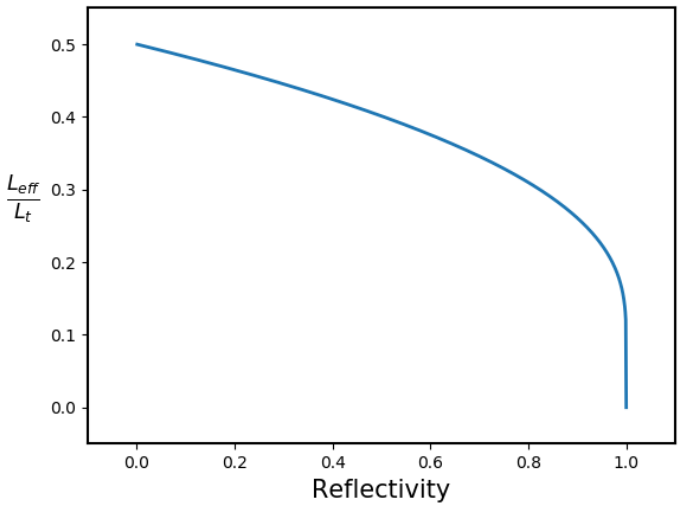


FIGURE 3.8: A plot of the effective length of a UFBG, at its Bragg wavelength, for different grating reflectivities. A value, $\frac{L_{eff}}{L_t} = 0.5$, corresponds to an ideal power distribution throughout the entire FBG length.

where the general UFBG length, $L$, has been replaced by $L_t$ so that it applies to a CFBG. Equation 3.36 is plotted in Figure 3.8, where it is demonstrated that a low reflectivity/low RI modulation UFBG has a longer effective length. This implies that the front loading effects seen in Figure 3.6 are exacerbated in a high reflectivity CFBG, and disappear in the limiting case of a zero reflectivity grating. Therefore, in regards to the proposed solution **(2)** (above), the second CFBG design principle is:

> *A CFBG detonation velocity sensor should be designed with a low reflectivity, to ensure a minimal gradient offset.*

As a final demonstration of how the bandwidth and reflectivity of a CFBG can reduce the severity of any non-linear erasure characteristics, two additional simulations have been carried out that are comparable to Figure 3.5. Figure 3.9(a) shows the reflected power vs length scaling for a 10 mm long, 20 nm bandwidth, 99% reflectivity CFBG. The gradient offset from this deign is approximately 6.2%, compared to the 8.7% offset when the bandwidth was only 10 nm. From visual inspection, the deviation from linearity also appears to start at a length of around 1 mm, as opposed to 1.5 mm for the lower chirp-rate grating.

Figure 3.9(b) shows the reflected power vs length scaling for a 10 mm long, 10 nm bandwidth, 20% reflectivity CFBG. In this case, the effect of a reduced reflectivity is immediately apparent — the gradient offset is reduced to less than 0.1% and is no longer visible. This is an example of why a low reflectivity design should be prioritised over a high chirp-rate design. Theoretically, even a uniform FBG with a low enough reflectivity will have an appreciably linear erasure response.

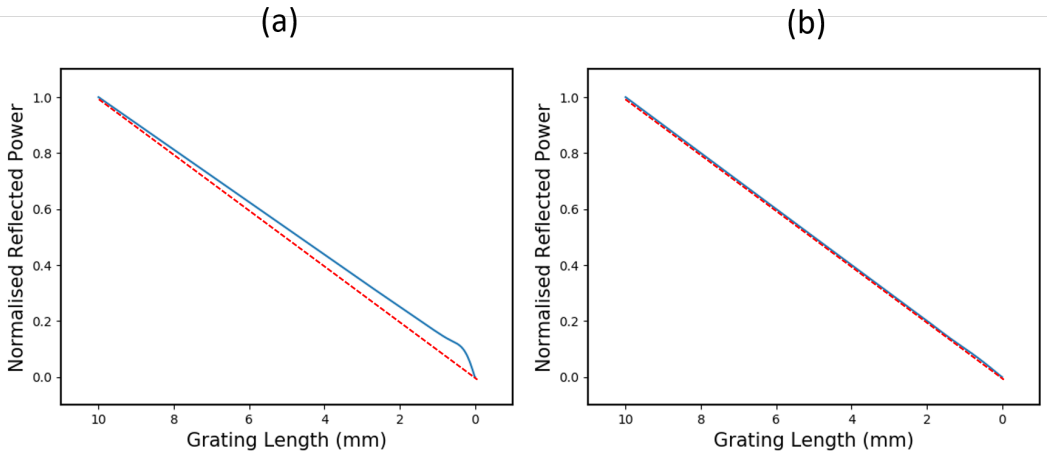


FIGURE 3.9: (a) A plot of the characteristic reflected power scaling for a 10 mm long, 20 nm bandwidth, 99% reflectivity CFBG. (b) A plot of the characteristic reflected power scaling for a 10 mm long, 10 nm bandwidth, 20% reflectivity CFBG.

### *Apodisation*

One further CFBG design feature, which should be considered for detonation velocity sensing, is the use of apodisation. As discussed in Section 3.1.2, an apodised CFBG is one in which the RI modulation amplitude is tapered at either end. This is done in order to minimise group-delay ripple effects, as well as reduce oscillations in the reflection spectrum. For these reasons, commercially manufactured CFBGs may be apodised by default, especially when a uniform reflectivity is specified.

Despite the *initial* "smoothing" effect of apodisation, it should be realised that once one end of the CFBG has been destroyed, the grating ceases to be fully apodised. Instead, the CFBG will be half-apodised, with the usual reflectivity ripple reappearing over its back half. In order to examine the effects of apodisation in detonation velocity measurements, a T-matrix erasure simulation has been carried out for a 10 mm long, 20% reflectivity, 10 nm bandwidth CFBG with a 10% sine-shaped apodisation at either end. This is shown in Figure 3.10.

It can be seen, in Figure 3.10, that the tapered RI modulation of an apodised CFBG results in a roll-in/roll-off effect in the erasure characteristics. This is because the lower RI modulation at either end contributes less reflected power per length than the other 80% of the grating. If this effect is not considered during analysis, then the predicted velocity could be erroneous — by comparing the ideal reading (red dashed line), to the apodised CFBG erasure, there is a clear gradient offset that, in this case, would result in a velocity error of over 10%.

Overall, there are no discernible benefits to using apodised CFBGs in detonation velocity measurements. This leads to the final CFBG design principle:

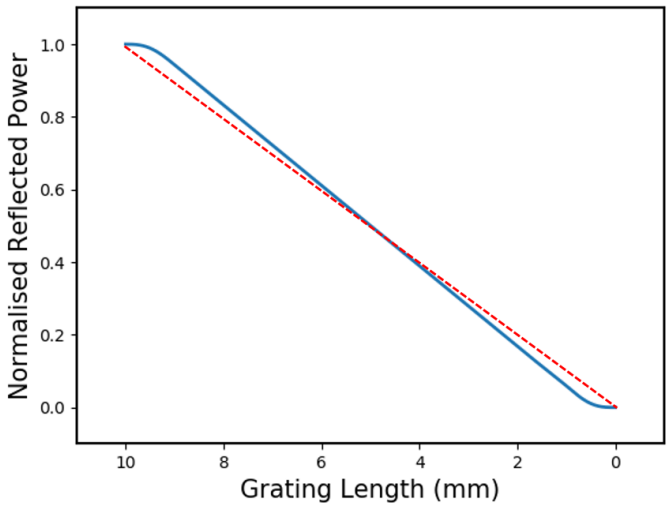


FIGURE 3.10: Graph showing how apodisation affects CFBGs in detonation velocity tests. The grating is 10 mm long, 20% reflectivity, with a 10 nm bandwidth and a 10% sine-shaped apodisation at either end. The apodisation can be seen as roll-in/roll-off in power as each end of the grating is destroyed. The dashed red line shows the ideal case, where reflected power is linearly proportional to grating length.

*A CFBG detonation velocity sensor should be designed without apodisation, to avoid unnecessary additional analysis.*

### 3.2.3 Results

To test the first two design principles, established in Section 3.2.2, a set of nine CFBGs were used as detonation velocity sensors in a series of cylinder tests (see Section 2). These nine CFBGs were designed to cover all permutations of the grating chirp-rates: $\frac{5}{12.25}$ **nm/cm,** $\frac{10}{12}$ **nm/cm,** $\frac{20}{11.5}$ **nm/cm**; and grating reflectivities: **<40%, 60–70%, >90%**. The corresponding spectra are shown in Figure 3.11, along with an additional 24 cm long CFBG to demonstrate the potential scalability of this method.

The raw data from a 115 mm long, 20 nm bandwidth, 96% reflectivity CFBG test is shown in Figure 3.12 and is representative of all the CFBG tests completed in this project. First, the data shows a considerable noise level (standard deviation of around ±1%) prior to detonation, which gradually diminishes as the detonation wave progresses. This is thought to arise due to the incoherence of the ASE source and its interaction with a structure that is prone to phase errors and time-delay fluctuations [60].

Secondly, the raw data is seen to be S-shaped, corresponding to PSD variations from the ASE source. In line with the simple calibration method, described in Equation 3.32, a calibration standard was generated to overcome this by integrating the ASE illuminated CFBG spectrum whilst sections of bandwidth were digitally removed. Assuming the

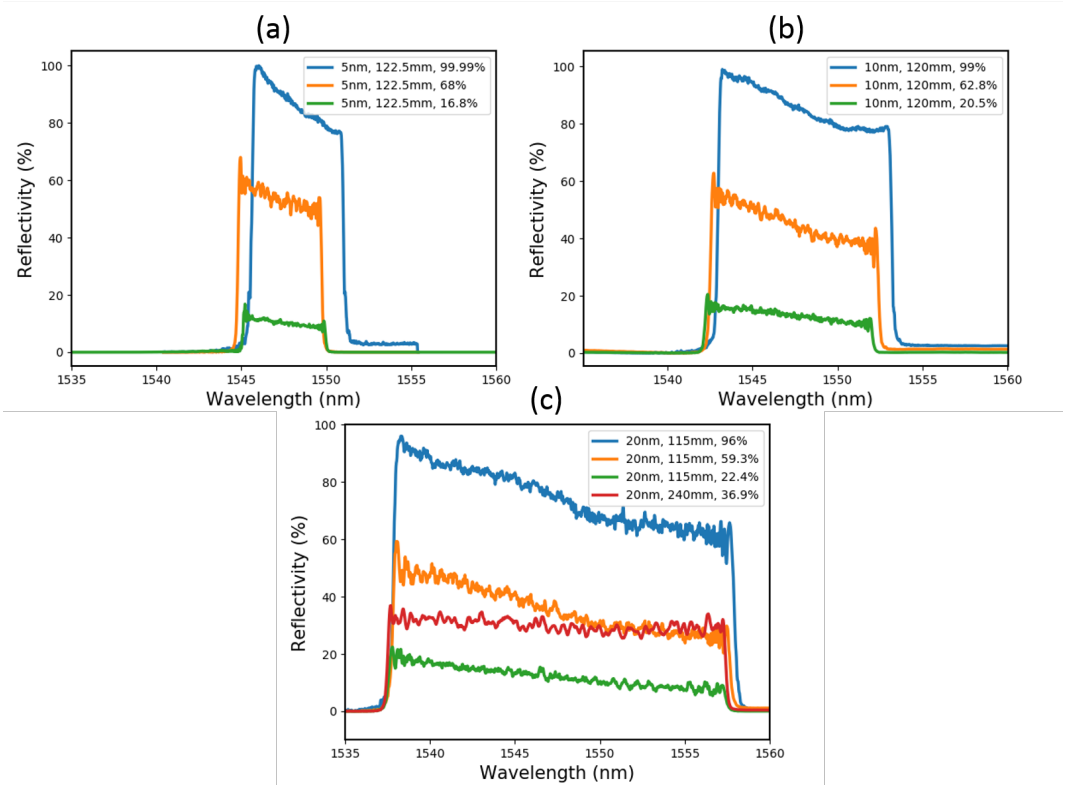


FIGURE 3.11: Grating spectra of the (a) 5 nm, (b) 10 nm and (c) 20 nm CFBGs used in the detonation velocity tests.

chirp-rate is known, this calibration standard can be compared to the raw data in order to obtain a distance-time plot of the traversing detonation shock-front.

The calibrated data for all three 20 nm bandwidth CFBGs is shown in Figure 3.13. These three CFBG tests are shown in descending order, based on their maximum reflectivity, from 96–22%. At the top of each plot, the fully calibrated data is shown, with a linear regression fit giving the average detonation velocity. In order to clearly reveal the underlying response of the CFBGs, any high-frequency voltage fluctuations have been removed using a 20 MHz low-pass filter.

Underneath each distance-time plot is a residual plot showing the deviation from linearity of each grating. A shaded box is used to highlight the non-linear region at the end of each erasure, where it can be seen that the high-reflectivity CFBG exhibits the most significant non-linearity.

An approximate, quantitative, breakdown of each plot is shown in Table 3.1, which gives the residual fluctuation over the highlighted region and the length of the highlighted region as a percentage of the total grating length.

Based on the arguments in Section 3.2.2, it was anticipated that the severity of the

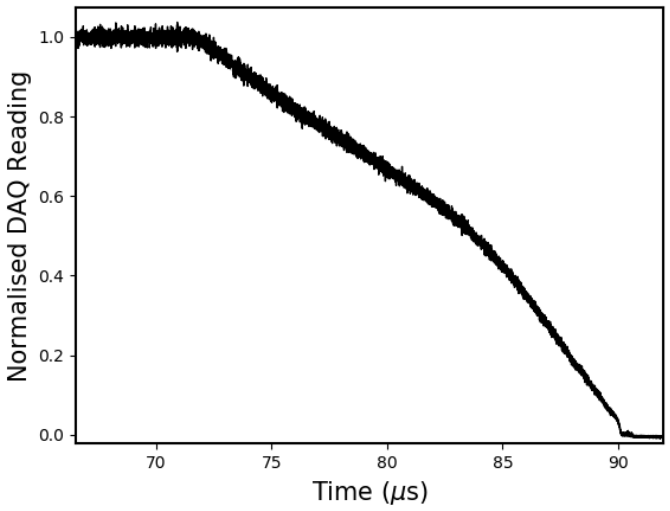


FIGURE 3.12: Normalised raw data from 20 nm bandwidth, 96% reflectivity, 115 mm CFBG test.

gradient offset (equivalent to the fluctuations in Table 3.1) would be greatest for high-reflectivity CFBGs. This is demonstrated in Table 3.1, which shows a noticeable fluctuation decrease from 2.01±0.04 % down to 0.48±0.09 % for the corresponding reflectivities, 96% and 59%. Beyond this, between 59% and 22%, there is no noticeable change in the residual fluctuation. This is thought to be a result of the fluctuation level becoming comparable in magnitude to the background noise level.

Simulations of three similar CFBGs show the same trend, with a 1.66% fluctuation for the 96% reflectivity grating decreasing to 0.48% for the 59% reflectivity grating. In the absence of noise, the 22% reflectivity grating is anticipated to show a fluctuation of around 0.12%.

Table 3.1 also shows a modest decline, of 0.87%, in the non-linear length when going from the highest to the lowest reflectivity. This was predicted in Figure 3.7, where the non-linear length shows a slight sensitivity to RI modulation amplitude. This is also seen again in the T-matrix simulated results, where a 3.15% non-linear length reduces to 2.31% between the 96% and 59% reflectivity gratings.

| **CFBG Reflectivity** (%) | **Fluctuation over Highlighted Region** (%) | **Relative Length of Highlighted Region** (%) |
|---|---|---|
| 96 | 2.01 ±0.04 | 2.87 ±0.32 |
| 59 | 0.48 ±0.09 | 2.12 ±0.65 |
| 22 | 0.48 ±0.13 | 2.00 ±0.54 |

TABLE 3.1: Table showing the properties of the non-linear region for different reflectivity CFBG tests.

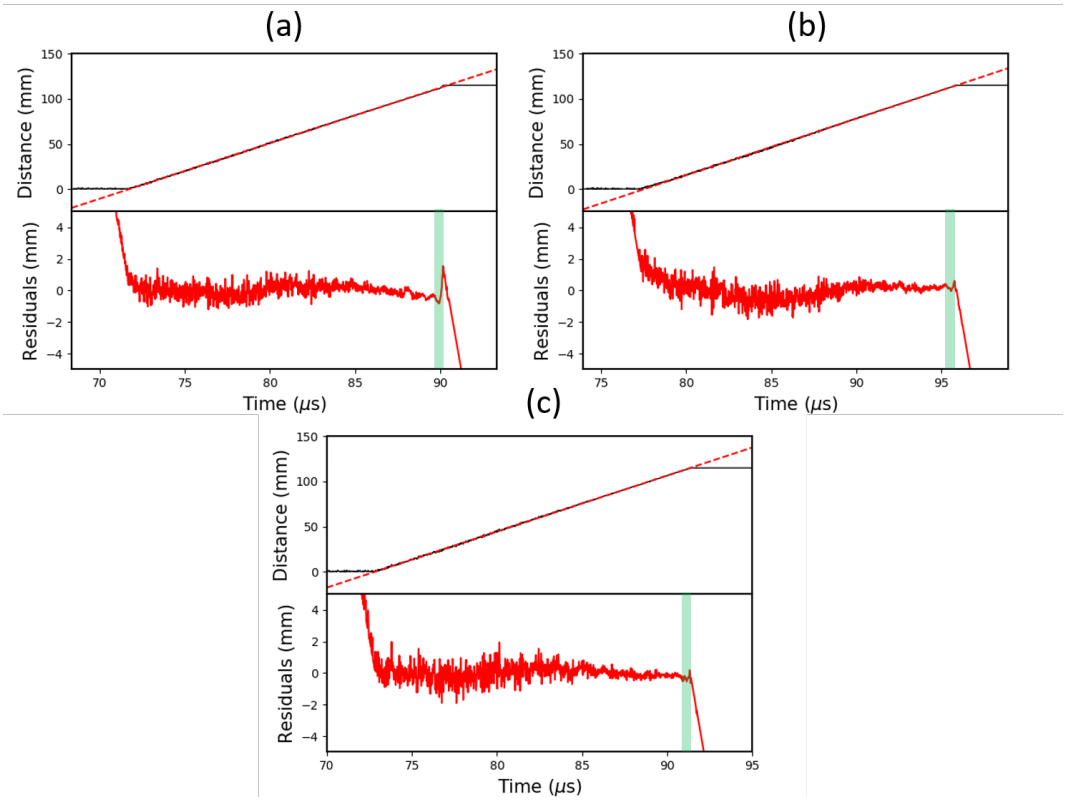


FIGURE 3.13: Graphs showing the calibrated and low-pass filtered (20 MHz) data from three 20 nm CFBG tests with (a) 96%, (b) 59% and (c) 22% reflectivity. Each CFBG is approximately 120 mm long. Plotted underneath are the residuals from the linear regression. The non-linear region, highlighted in green, is most prominent in the 96% reflectivity CFBG.

A similar analysis is shown in Table 3.2, for the plots in Figure 3.14. This time, three CFBG tests are shown for various ascending bandwidths (5 nm, 10 nm, 20 nm) and the reflectivity of each grating is kept within a similar range (59–68%). In this case, the highlighted non-linear region is seen to shrink as the bandwidth (chirp-rate) increases, from 4.88±0.67% down to 2.12±0.65%. This is congruent with Figure 3.7, which predicts that the non-linear length is particularly sensitive to changes in chirp-rate. Furthermore, T-matrix simulations of the same gratings yield a non-linear length of 5.22%, 3.46% and 2.31% for the 5 nm, 10 nm and 20 nm gratings respectively, demonstrating a very similar trend.

An additional effect, which has not so far been discussed, is the reduced gradient offset (fluctuation) for higher chirp-rates. In Table 3.2, the fluctuation is seen to decrease from 1.44±0.08% down to 0.48±0.09% between the bandwidths of 5 nm and 20 nm. This is because, as the chirp-rate increases, the coherence length *decreases* but the reflectivity stays the same — referring to Equation 3.36, this results in a smaller *absolute* effective length. When the effective length shrinks, relative to the total CFBG length, the front-loading spike seen in Figure 3.6 also shrinks and, hence, less of the total power is reflected from this region.

Again, the same decrease in fluctuation is noticeable in the simulated data for gratings of increasing bandwidth. In this case, the fluctuation goes from 1.08% for the 5 nm bandwidth grating down to 0.48% for the 20 nm bandwidth grating.

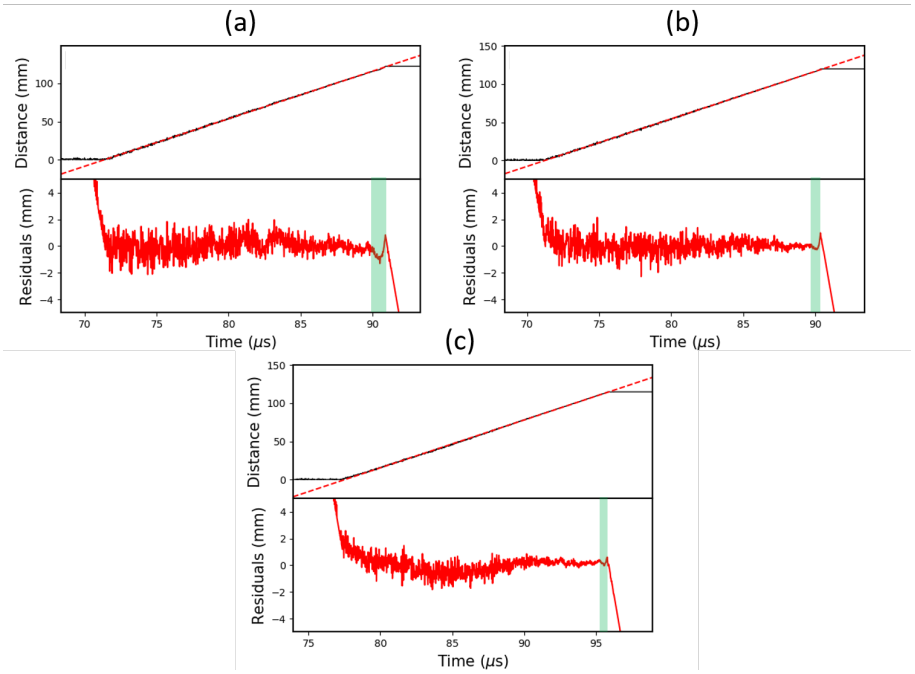


FIGURE 3.14: Graphs showing the calibrated and low-pass filtered (20 MHz) data from three 60-68% reflectivity CFBG tests with (a) 5 nm, (b) 10 nm and (c) 20 nm bandwidths. Each CFBG is approximately 120 mm long. Plotted underneath are the residuals from the linear regression. The non-linear region, highlighted in green, is longest for the 5 nm bandwidth CFBG.

| **CFBG Bandwidth** (*nm*) | **Fluctuation over Highlighted Region** (%) | **Relative Length of Highlighted Region** (%) |
|---|---|---|
| 5 | 1.44 ±0.08 | 4.88 ±0.67 |
| 10 | 1.03 ±0.04 | 3.22 ±0.24 |
| 20 | 0.48 ±0.09 | 2.12 ±0.65 |

TABLE 3.2: Table showing the properties of the non-linear region for different bandwidth CFBG tests.

To demonstrate the potential scalability of the CFBG detonation velocity sensor, one last test was conducted using a 24 cm long grating. This CFBG was designed following the design principles laid out in Section 3.2.2, with a broad 20 nm bandwidth and a 37% reflectivity. Figure 3.15 shows a plot of the results, with the corresponding analysis shown in Table 3.3.

In comparison with the previous test data, the results in Table 3.3 demonstrate further consistency in relation to the proposed optimisations. The residual fluctuation of

0.26±0.04% is comparable to the fluctuation measured by the low reflectivity 20 nm CFBGs in Table 3.1, except that it is approximately halved due to the difference in grating length. Furthermore, the relative length of the non-linear region is approximately half as long as the 10 nm CFBG, shown in Table 3.2. This was anticipated, because both gratings have identical chirp-rates, but the 24 cm CFBG is twice as long as the 12 cm grating — hence the *absolute* length of the non-linear region is the same, but the relative length is halved.

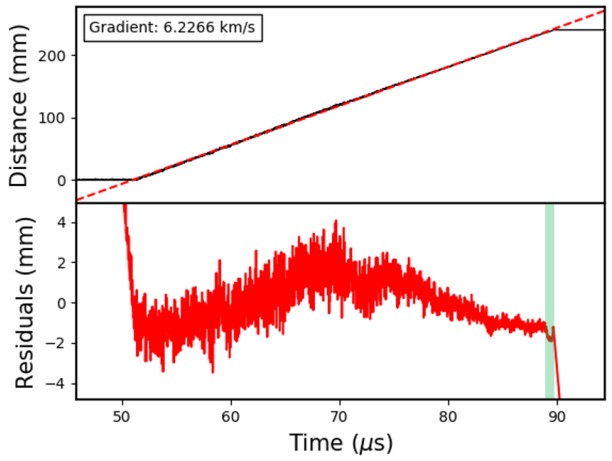


FIGURE 3.15: Plot showing the data from a 24 cm, 20 nm bandwidth, 37% reflectivity CFBG test.

| **Fluctuation over Highlighted Region** (%) | **Relative Length of Highlighted Region** (%) |
|---|---|
| 0.26 ±0.04 | 1.60 ±0.12 |

TABLE 3.3: Shows properties of the non-linear region for a 24cm, 20nm bandwidth, 37% reflectivity CFBG test.

### 3.2.4 Design Summary

In this section, the optimal CFBG design parameters for detonation velocity measurements are reiterated, but with more emphasis and discussion on the practicalities of implementing these gratings. A brief summary of this information is given in Table 3.4.

#### *Reflectivity*

It has already been established that a low-reflectivity CFBG will exhibit reduced non-linear effects during detonation velocity measurements. Based on the tests shown in

Section 3.2.3, a reflectivity range of 20–60% can achieve good results, but this must be considered alongside the characteristics of the interrogation setup.

For example, if a given photodetector is likely to be saturated by the full reflected power of the CFBG, then using a lower-reflectivity grating may be preferable to using an attenuator. Conversely, if more power is required for an insensitive photodetector, a higher-reflectivity CFBG may be preferable to using an amplifier.

#### *Chirp-Rate & Bandwidth*

There are two major benefits to using broad bandwidth CFBGs. First, as demonstrated in Section 3.2.3, a high-chirp rate results in a minimised non-linear region. Secondly, for low-reflectivity CFBGs, a higher total reflected power can be achieved by broadening the bandwidth.

However, the following caveats apply:

- Due to the requirements on the RI modulation amplitude, it can be difficult to fabricate CFBGs that have a high chirp-rate *and* a high reflectivity [48].
- The full bandwidth of the CFBG must be suitably matched to (i.e. sufficiently smaller than) the source bandwidth.
- The full bandwidth of the CFBG must be considered in regards to the *responsivity* of the chosen photodetector.

#### *CFBG Filters*

In some scenarios, it could be considered beneficial to employ an extra CFBG as a filter (immediately prior to the photodetector), with the aim of cutting out unwanted Fresnel reflections and coupled explosive radiation. However, it is expected, based on Figure 3.12, that the presence of another CFBG in the setup may contribute, considerably, to the total signal noise. Thus, in some cases, there may be a net deterioration in signal quality when using a CFBG as a filter.

#### *Launch End*

In general, CFBGs should be implemented so that the probe signal is incident on the short wavelength end — for detonation velocity measurements, the long wavelength end is destroyed first. This is so that cladding-mode coupling does not deplete the signal power reaching the back-end of the grating [61].

| **Design Parameter** | **Optimal Implementation** | **Explanation** |
|---|---|---|
| CFBG Chirp-Rate/Bandwidth | ✓ High Chirp Rate | A high chirp-rate minimises the length of the non-linear region. |
| CFBG Reflectivity | ✓ Low Reflectivity | A low reflectivity reduces the severity of the non-linear region and simplifies fabrication of high chirp-rate gratings. |
| Signal Input/Output End | ✓ Short Wavelength End | Source light should enter and leave the grating from the short wavelength end to avoid cladding-mode loss. |
| Additional CFBG Filtering | − Apply with Caution | Some applications may require additional filters, but in other cases the extra CFBG could contribute more noise than it filters out. |
| Source Attenuation | − Can be Avoided | Attenuation can be avoided by designing CFBGs whose reflected power is below the detector saturation level. |
| CFBG Apodisation | ✗ No Apodisation | Apodisation will tend to delinearise the length vs reflected power at each end of the grating. |

TABLE 3.4: Shows a summary of design considerations for CFBG detonation velocity tests.

## 3.3 Uniform Fibre Bragg Grating Probes

Whilst the CBFG method of measuring detonation velocity is well established and has been successfully demonstrated a number of times, it is deficient in one aspect — it appears to suffer from high levels of *optical* noise. This is seen in Figure 3.12 and is a limiting factor for the maximum spatial resolution that can be achieved.

In this section, a new technique is described where CFBG velocity probes are replaced with UFBGs [62]. The ultimate aim of this new technique is to increase the spatial resolution that can be measured using fibre optic methods and allow researchers to look in more detail at dynamic changes in the propagation of a detonation shockwave.

### 3.3.1 Concept

A uniform fibre Bragg grating (UFBG) has a single resonant wavelength, $\lambda_B$, which has been shown, in Section 3.1.1, to correspond to a peak reflectivity,

$$R_{peak}(L) = tanh^2(\kappa_{ac}L). \tag{3.37}$$

Off-resonance wavelengths also incur some level of phase-matching and are subject to a (more general) grating reflectivity,

$$R(\lambda, L) = \frac{|\kappa_{ac}\sinh(\alpha L)|^2}{|\delta\sinh(\alpha L) - i\alpha\cosh(\alpha L)|^2}, \tag{3.38}$$

which is the square of Equation 3.12 in Section 3.1.1.

Based on Equations 3.37 and 3.38, there two ways in which a UFBG can be used to measure detonation velocity. First, similar to the CFBG method, a UFBG may be illuminated with a broad bandwidth source, so that the total reflected power is proportional to the grating length as follows,

$$P(L) = \int_{\lambda_0}^{\lambda_1} R(\lambda, L)\cdot S_{psd}(\lambda)\cdot d\lambda, \tag{3.39}$$

where $S_{psd}$ is the power spectral density of the broadband probe source. From now on, this will be referred to as the *hybrid method*, since it requires the substitution of a UFBG directly into the CFBG setup, Figure 3.4.

Alternatively, if a very narrow bandwidth source is used to illuminate the UFBG at its Bragg wavelength, the reflected power is proportional to the grating length as,

$$P(L) = \int_{\lambda_0}^{\lambda_1} R(\lambda, L) \cdot S_0 \cdot \delta_{\lambda\lambda_B} \cdot d\lambda, \tag{3.40}$$

where $S_0$ is the source power and $\delta_{\lambda\lambda_B}$ is a Kronecker delta function,

$$\delta_{\lambda\lambda_B} = \begin{cases} 0 & \text{if } \lambda \neq \lambda_B \\ 1 & \text{if } \lambda = \lambda_B. \end{cases} \tag{3.41}$$

Using Equation 3.37, this simplifies to,

$$P(L) = S_0 \cdot R_{peak}(L) = S_0 \cdot tanh^2(\kappa_{ac} L). \tag{3.42}$$

This method will be referred to as the *narrowband method* and is the primary focus of this section, due to its novelty, simplicity and low-noise characteristics.

A simulation of these two methods is shown in Figure 3.16. Figure 3.16(a) shows a variety of 10 mm long UFBG reflection spectra with different peak reflectivities. Of particular interest here is the 99% reflectivity grating, which is noticeably broader in bandwidth and more rectangular in shape than the other three.

Figure 3.16(b) illustrates the difference between the hybrid and the narrowband schemes. In this plot, each overlaid spectrum shows a different stage of a UFBGs erasure, from its initial state (90% peak reflectivity, 10 mm long), to its final state (grating totally erased). The black dots represent the change in peak reflectivity that is monitored in the *narrowband* method, whereas the shaded region under each spectrum is representative of the total power monitored in the *hybrid* method.

The narrowband tehcnique is explored further in Figure 3.16(c), where the peak reflectivity, of each grating from Figure 3.16(a), is plotted during its deconstruction, from 10–0 mm. In this case, the high-reflectivity UFBG has a primarily convex erasure — the lack of signal power reaching the back-end of the grating means that the peak reflectivity is relatively insensitive to length changes over the first ∼5 mm. On the other hand, the 10% reflectivity UFBG shows a concave erasure, where the peak reflectivity is *more* sensitive to length changes over the back-half than the front. These plots follow a characteristic atanh$^2$ shape, in line with Equation 3.42.

In Figure 3.16(d), the same simulation is done, but for the hybrid scheme. In this case, like the narrowband method, the high-reflectivity UFBG has a convex erasure due to a front-loaded power distribution. Unlike the narrowband scheme, however, the lower-reflectivity gratings do not have an increasingly concave erasure, but instead approach linearity.

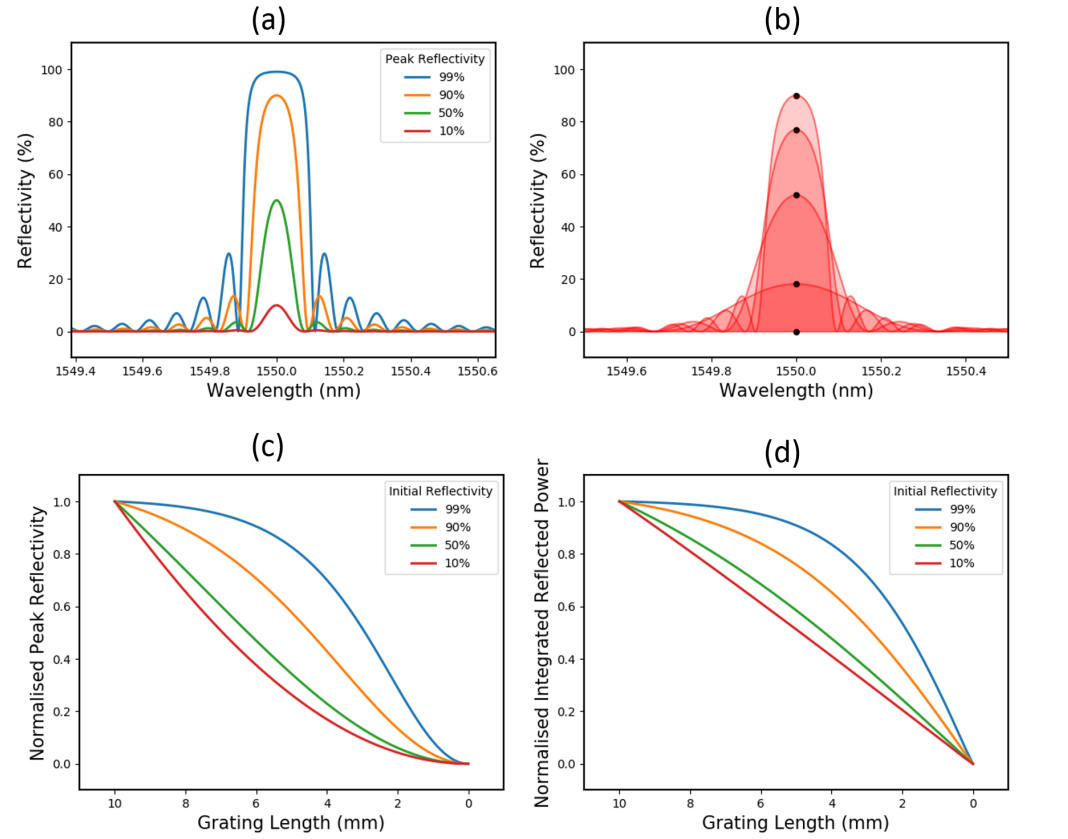


FIGURE 3.16: (a) Shows the simulated spectra of four UFBGs, each with a different peak-reflectivity. (b) Shows spectra for a simulated 10 mm long UFBG, which has an initial reflectivity of 90%. Each successive plot shows the grating shortened by 2.5 mm, with a dot highlighting the peak-reflectivity. (c) Shows how the peak-reflectivity of each UFBG scales with length in the narrowband scheme. (d) Shows how the peak-reflectivity of each UFBG scales with length in the hybrid scheme.

In the hybrid method, the ability to use low-reflectivity UFBGs as linear probes without significant calibration is a considerable benefit. However, as it will be demonstrated shortly, the hybrid method suffers from: **(1):** Optical noise that is visibly similar to that seen in the CFBG tests; **(2):** A signal strength that is considerably lower than a CFBG of similar length — for a gain flattened 1 mW/nm ASE input source, a 10 mm long, 10 nm bandwidth, 50% reflectivity CFBG will reflect an initial signal power of ∼7 dBm. In comparison, a 10 mm long, 50% reflectivity UFBG in the hybrid scheme will reflect an initial signal power of around -10 dBm.

In the narrowband method, an excellent signal to noise ratio can be achieved, because the entire source power is concentrated within the grating bandwidth. Figure 3.17 shows the setup used to make detonation velocity measurements with the narrowband UFBG scheme. The main difference between this setup and the CFBG setup, aside from the use of a UFBG, is that the ASE source has been replaced by a narrow bandwidth, tunable laser source that is set to the Bragg wavelength of the probe.

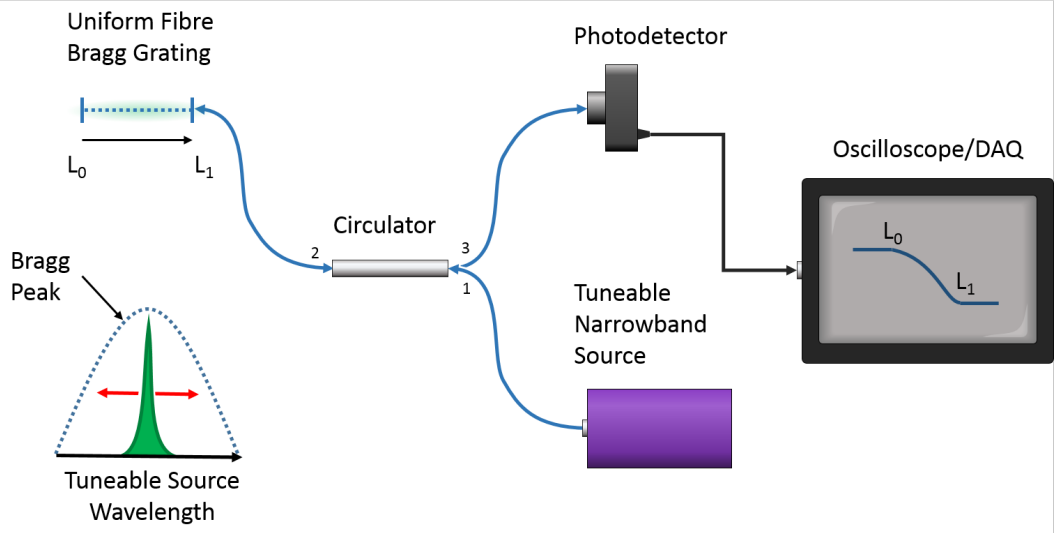


FIGURE 3.17: Schematic showing the interrogation setup for UFBG velocity probes in the narrowband scheme. A narrow bandwidth source is tuned to the Bragg wavelength of a grating. The reflected signal passes through a circulator and is collected on a photodetector.

### 3.3.2 Results and Discussion

This section is divided into two parts, documenting the evolution of the UFBG technique as it happened chronologically. It shows, first, the results obtained in a series of pilot tests using the *hybrid* method which, at the time, was seen as the logical successor to the CFBG technique.

These hybrid tests were carried out using *arrays* of short UFBGs, in order to increase the scalability and reflected power per unit length, as well as to allow the use of *wavelength division multiplexing* (WDM) filters. In the case of the WDM tests, it was hoped that such severe filtering would dramatically increase the optical signal-to-noise ratio in comparison to the CFBG methods and that using a single detector per ∼10 mm would lessen the effects of quantisation error.

However, upon the discovery that a significant amount of noise arose from *within* the grating bandwidth, the hybrid method was set aside in favour of the narrowband method. In the second part of this section, the results from a series of narrowband tests is shown — these tests emphasised the simultaneous implementation of multiple velocity probes and, hence, a direct comparison can be made between the CFBG, narrowband UFBG and PDV (see Section 1.3) techniques.

#### *Hybrid Method*

As shown in Figure 3.16(d), a lower UFBG reflectivity corresponds to a more linear erasure response in the hybrid scheme. To test this, two types of UFBG array were

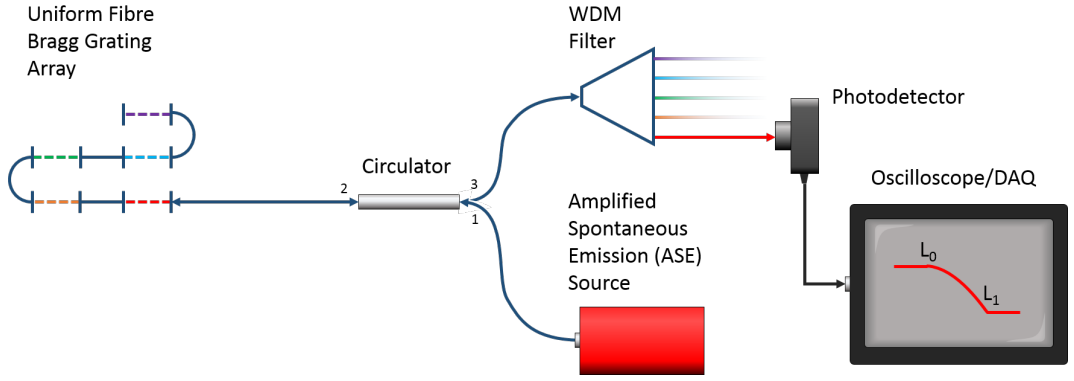


FIGURE 3.18: Schematic showing the interrogation setup for UFBG velocity probes in the hybrid WDM scheme. A broad bandwidth ASE source is used to illuminate an array of wavelength separated UFBGs. The reflected signal passes through a circulator and is then either collected on a photodetector, or separated using a WDM array onto a bank of photodetectors (shown).

fabricated: **(1)** A $5 \times 10$ mm array of low-reflectivity gratings ($\sim$35%) and; **(2)** A $5 \times 10$ mm array of various reflectivity gratings. The intention of design (1) was to make a probe that was approximately linear and could be used as a direct alternative to the CFBG. The array, type (2), was fabricated in order to validate the simulations shown in Figure 3.16 and to try and find an optimal middle ground between linearity and signal-to-noise ratio. Both types of array were fabricated so that their Bragg wavelengths were matched to the channels of a 100 GHz *arrayed waveguide grating* (AWG) filter (i.e. a 0.8 nm separation) — this allowed them to be used with one detector per 10 mm grating, as illustrated in Figure 3.18.

As an initial experiment, to see if the arrays and WDM would work as anticipated, a *cutback test* was carried out. In this test, the configuration in Figure 3.18 was setup, but with the photodetectors replaced by power meters. The UFBG array could then be incrementally cut down in length by a razor blade, taking care to apply a drop of RI matching fluid to each cut, with the total reflected power noted at each stage.

Figure 3.19 shows two examples of cutback tests, with an example of a type (1) UFBG array spectrum shown in Figure 3.19(a). In the first case, Figure 3.19(b), a type (1) array was tested without an AWG filter and can be seen to fit the theory well, with an average deviation of 1%. In Figure 3.19(c), the results from an AWG filtered UFBG array are shown, where each AWG channel has been normalised and is plotted together to show all five grating erasures in one graph. Again, the results fit well to the simulations, with an average deviation of just over 2%.

Whilst these cutback tests offer some vindication that the hybrid method should work, an uncertainty remains over the practicality of using such sensors in explosive tests. More specifically, whether the signal power will be significant enough to use high-speed detectors and still achieve an acceptable signal-to-noise ratio.

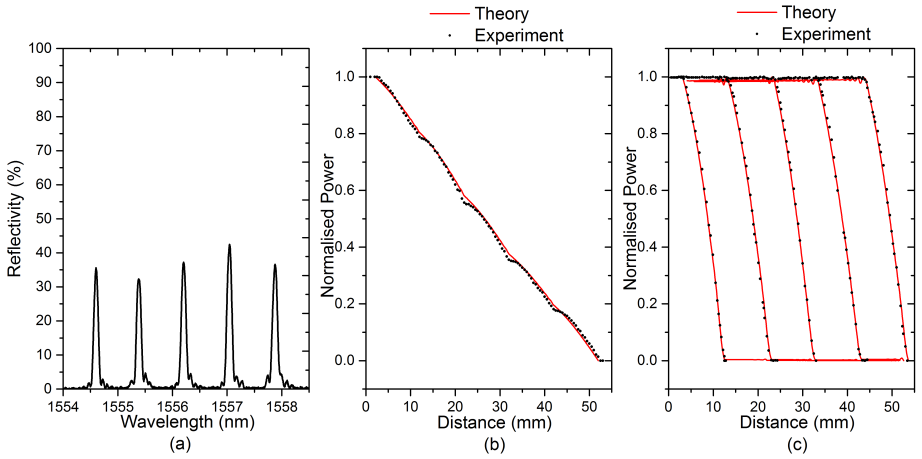


FIGURE 3.19: (a) A type (1) UFBG array spectrum, showing five gratings, separated by 0.8 nm, and with a similar reflectivity (37±5%). (b) An unfiltered UFBG cutback test comparing the experimental and simulated results. (c) An AWG filtered UFBG cutback test comparing the experimental and simulated results for each filter channel.

In a set of pilot cylinder tests, a small number of UFBG arrays were implemented, both with and without an AWG filter, to assess their capability as detonation velocity sensors. In these tests, Thorlabs 150 MHz InGaAs PDA10CF photodetectors were used to monitor the reflected power, with either a 16 GHz Lecroy 816Zi oscilloscope or its 4 GHz equivalent (when five channels were required for the WDM hybrid setup) at the back-end. Furthermore, it was noticed in the cutback tests that the gratings were not perfectly back-to-back in the array. This was thought to be due to incidental exposure "washing out" part of each adjacent grating during fabrication. To overcome this, the UFBG arrays used in the pilot tests were fabricated so that there was a 3 mm gap between each one.

The data from an unfiltered UFBG array cylinder test is shown in Figure 3.20. First, Figure 3.20(a) shows the results prior to low-pass filtering, so that the extent of the signal noise can be clearly seen. At its maximum, immediately prior to detonation, the noise on the signal has a standard deviation of ±4% — equivalent to a spatial uncertainty of around ±2.5 mm.

This noise appears to accumulate as the signal travels through the UFBG array, because it significantly reduces as the detonation wave destroys the gratings farthest from the source. For this reason, it is understood that the noise is primarily carried by the *optical* signal and is not dominated by any *electronic* effects. Once the entire grating is destroyed, a signal fluctuation of ±0.7% (±0.43 mm) persists and is likely to be due to electronic noise.

In Figure 3.20(b), the same data is shown, but this time a 20 MHz low-pass filter has been applied in order to minimise the high-frequency noise. A linear regression fit gives the average velocity over the entire erasure and yields a value of 6.21 km/s. This is within 0.5% of the PDV velocity (6.24 km/s) for the same test. The final grating in

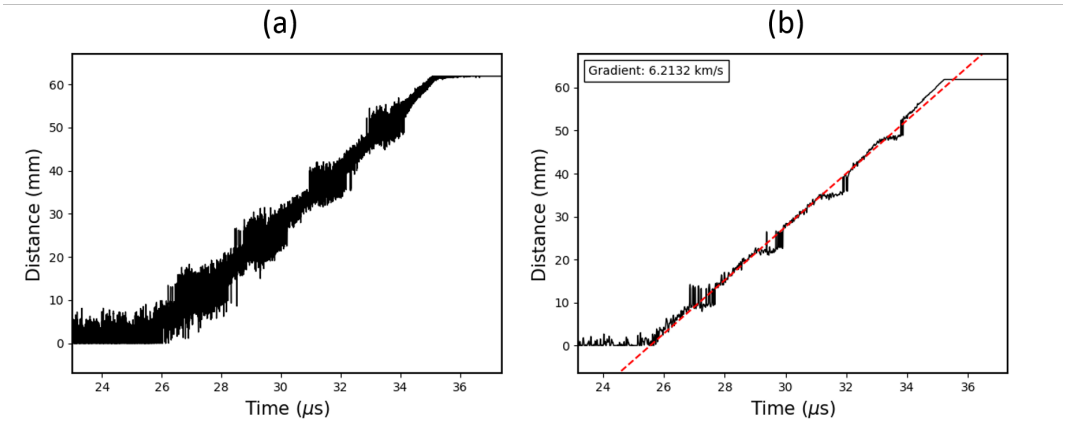


FIGURE 3.20: (a) A type (1) hybrid UFBG test *without* an AWG filter and with no low-pass filter applied. (b) A type (1) hybrid UFBG test *without* an AWG filter, but with a 20 MHz cutoff low-pass filter applied and a linear regression fit showing the average velocity over the entire erasure.

the array clearly diverges from the linear regression fit, giving a velocity of over 7 km/s. such an extreme increase in velocity was neither anticipated, nor seen in the PDV trace, and is likely to be due to an error in calibration.

Next, an AWG filter was added to the setup, Figure 3.18, and a type (2) array was implemented as the velocity probe. The intention of this test was to isolate the various reflectivity UFBGs and find an optimal design. It was also, originally, hoped that the AWG filter would drastically reduced any unwanted optical signal noise.

Figure 3.21(a) shows the normalised, but uncalibrated, data from each channel of the AWG, prior to any low-pass filtering. The influence of optical signal noise is very clear from these plots, and peaks at ±12% (±1.2 mm) before the first grating is destroyed. Once the entire array has been consumed, a residual noise level of ±1.3% (±0.13 mm) indicates the amount of electronic noise coming from the photodetectors and oscilloscope.

The type (2) array in this test consisted of five gratings of *ascending* reflectivity (the first grating to be destroyed was also the lowest reflectivity), from ∼40–90%. Whilst there is a clear reduction in noise, going from the low to the high reflectivity gratings, it is not easy to decipher whether this is due to the grating design or just the same noise reduction seen in Figure 3.20 for a type (1) array. The noise also masks any appreciable change in the erasure shape between each grating.

In Figure 3.21(b), the calibrated data is plotted, with a 20 MHz low-pass filter having been applied. The data from each AWG channel has also been shifted in 13 mm intervals to show the full progression of the detonation wave. The dashed red line is not a linear regression fit, but is drawn in manually to help visualise the trend.

To calculate the average velocity over the full 62 mm structure, a linear regression fit is required for each individual grating, which can then be combined to give a total average.

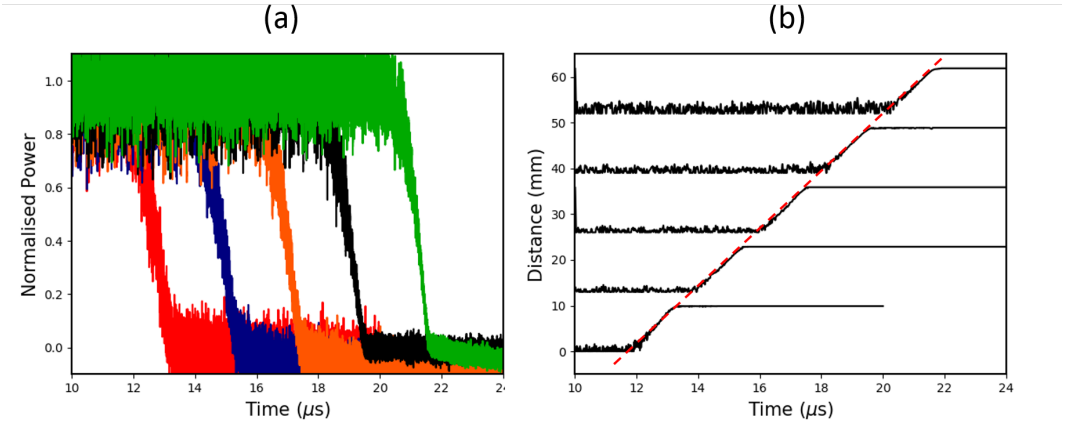


FIGURE 3.21: (a) An uncalibrated type (2) hybrid UFBG test *with* an AWG filter and with no low-pass filter applied. (b) A type (2) hybrid UFBG test *with* an AWG filter and a 20 MHz cutoff low-pass filter applied. The data from each AWG channel has also been shifted to show the progression of the shockwave, with a red dashed line added manually to help illustrate its linearity.

From start to finish, the velocity of each grating is found to be 7.07 km/s, 6.14 km/s, 6.37 km/s, 6.15 km/s, 5.99 km/s, which gives a total average velocity of 6.34 km/s. This velocity is approximately 1.3% higher than the average velocity from the PDV trace; 6.26 km/s.

From a practical point of view, the WDM UFBG method is more challenging to implement, in comparison to the other fibre optic methods presented in this report. First, the wavelength spacing of the UFBG array is critical and should fit the channels of an AWG filter. Secondly, prior to detonation, the AWG filter must be temperature tuned to the match the FBG resonances, which are likely to have shifted due to the ambient temperature of the test facility. Lastly, for accurate calibration, the AWG filter shape must be included in the FBG erasure simulation.

However, in comparison to the unfiltered UFBG array method, the WDM method does appear to show a slight improvement in noise levels ($\pm$2.5 mm peak uncertainty in the unflitered case; $\pm$1.2 mm in the filtered case). This could be due to a combination of higher average grating reflectivity, and reduced quantisation error from the multi-detector setup.

In summary, detonation velocity measurements using the hybrid scheme can be used to obtain average velocities to within 2% of the expected value. The method is also more scalable than the CFBG technique, and hybrid UFBG array setups with very short FBGs could conceivably be used to make discrete velocity measurements — where each short FBG is analogous to a pin in a pin-probe setup. However, spatial uncertainties in the mm scale are too high for the resolution sought in this project (sub-mm, ideally below 100$\mu m$).

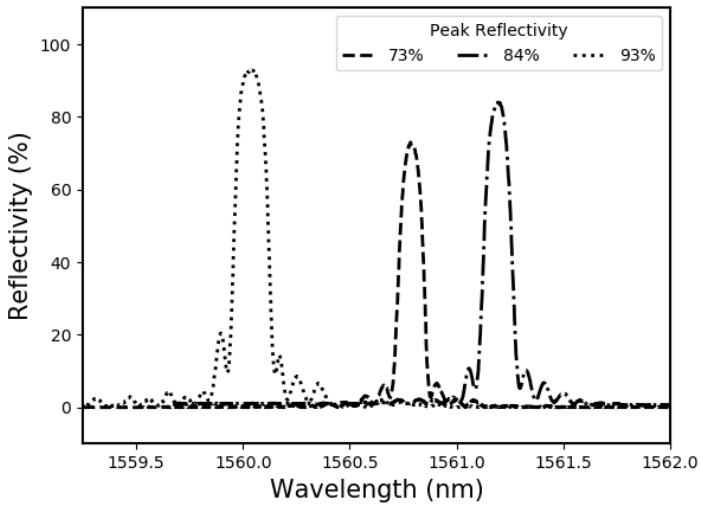


FIGURE 3.22: Reflection spectra for the three UFBGs used in the narrowband tests. The gratings are 9.90±0.03 mm long and have initial peak-reflectivities of 73%, 84% and 93%.

***Narrowband Method***

During the pilot testing phase, the narrowband method was trialed for the first time. These tests failed to give reasonable velocity measurements due to an unidentified systematic fault, but the signal recorded was very clean — the high levels of optical noise, that could be seen in the CFBG and hybrid UFBG methods, were lost beneath the electronic noise of the detector and oscilloscope. The narrowband method was then re-tested in a more formal set of cylinder tests, where it could be directly compared to results from the CFBG method.

To reiterate; in the narrowband method, a narrow bandwidth interrogation source is used to monitor changes in the peak reflectivity of a UFBG, where a change in reflectivity is proportional to a change in the UFBG length (see Figure 3.16(c)).

The setup that was used for these narrowband tests is shown in Figure 3.17. In this case, a coherent input signal was provided by a Tunics-SW (3642 HE 15) tunable laser source, the photodetector was a 150 MHz InGaAs Thorlabs-PDA10CF and the DAQ system was a 10-bit National Instruments PXIe-5160 oscilloscope, with the sampling rate set at 1.25 GSamples/s.

The three UFBGs that were used in these tests are shown in Figure 3.22. Each grating was 9.90±0.03 mm long, with an initial peak-reflectivity of 73%, 84% and 93% respectively. The gratings all had a bandwidth of at least 160 pm ($\sim$ 20 GHz), which was significantly broader than the bandwidth and wavelength stability of the $<$ 100 kHz bandwidth source. This allowed for the laser wavelength to be *manually* tuned to the UFBG Bragg wavelength, without too much difficulty.

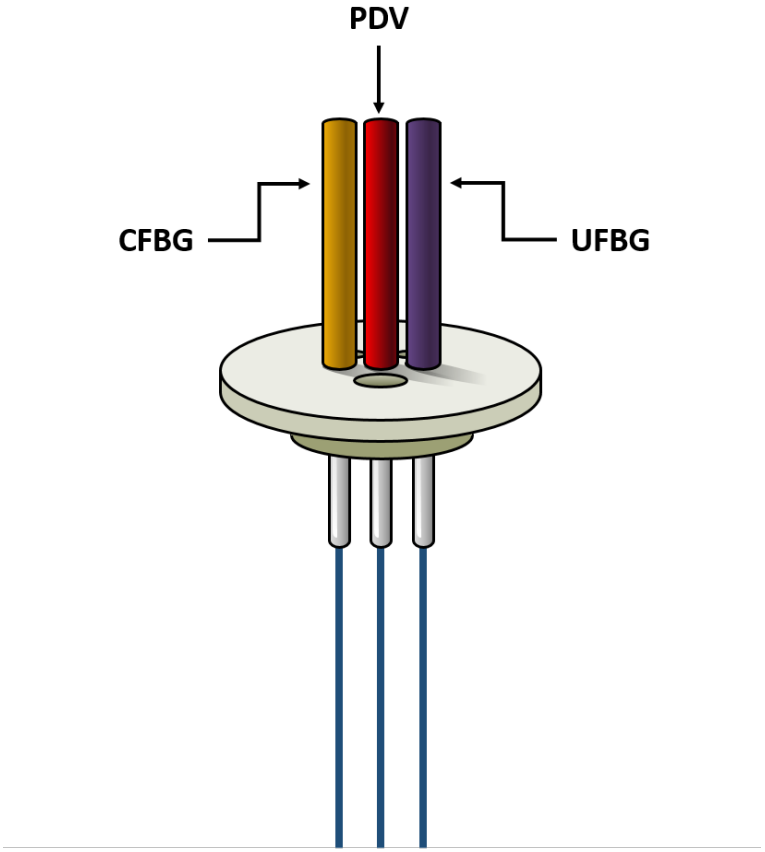


FIGURE 3.23: Illustration of the lid setup for the UFBG simultaneous probe tests. The PDV measurement was always taken from the centre of the cylinder, where the detonation wave was expected to be approximately planar.

Alongside each of these UFBG tests, a PDV and CFBG velocity measurement were also setup, to allow a direct comparison between all three methods under near-identical conditions — as shown in Figure 3.23, the PDV probe was mounted in the centre of the cylinder, with the UFBG and CFBG probes either side.

In Figures 3.24(a)–(c), the normalised raw data from each of the three narrowband tests is shown. Figures 3.24(d)–(f) show the simulations used to calibrate the experimental data, and were calculated using Equation 3.37. At a glance, the shape of the experimental data matches well to the simulations and the signal noise is significantly lower than previously seen in the CFBG and hybrid UFBG tests.

Figure 3.25 shows the calibrated narrowband UFBG data, which has been averaged to account for the eight-fold oversampling of the oscilloscope. The red dashed lines show the results of a linear regression fit for each data set, giving average velocities of 6.250 km/s, 6.247 km/s and 6.396 km/s in ascending order of reflectivity.

As an initial comparison, the data from the PDV, CFBG and narrowband UFBG are all plotted together in Figure 3.26. The PDV data, which is recorded as a velocity–time

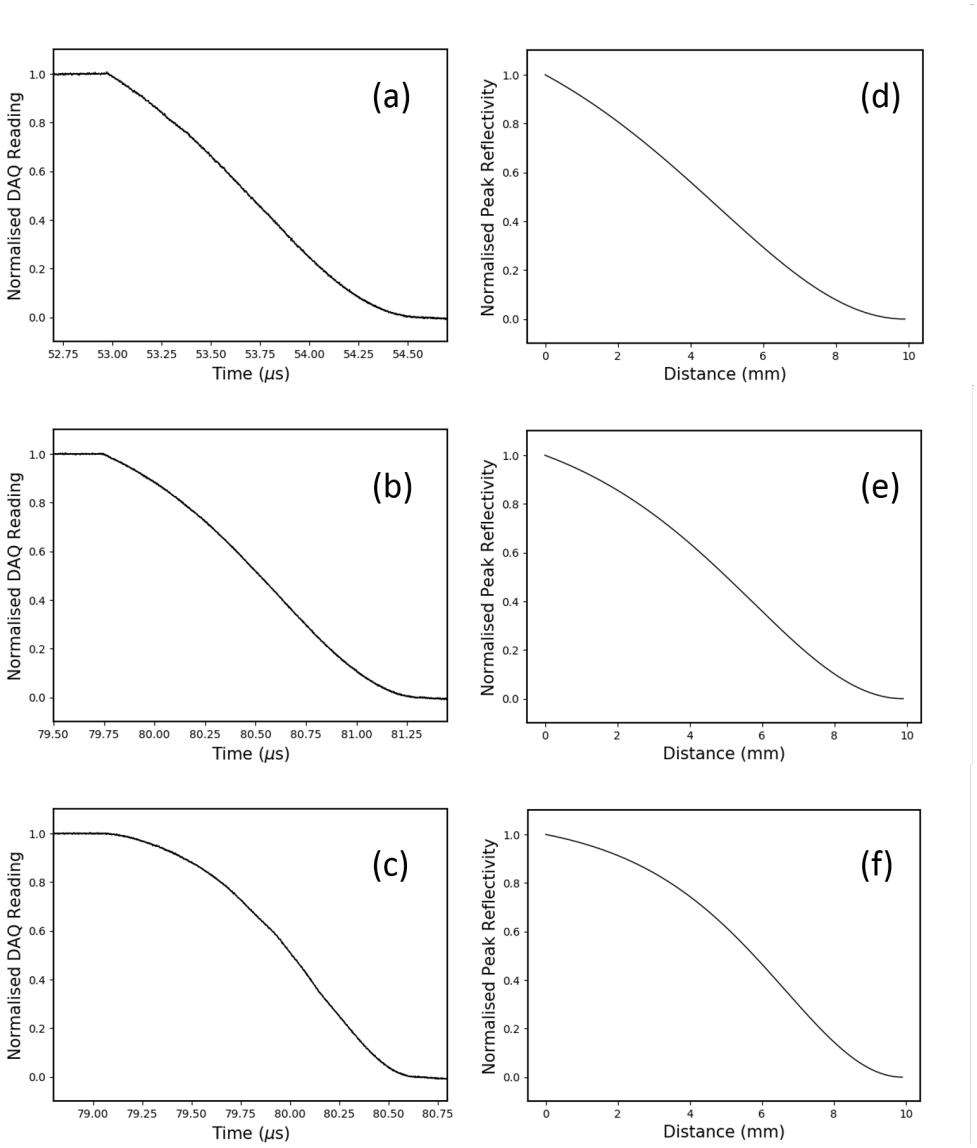


FIGURE 3.24: (a)-(c) shows the normalised raw DAQ data from the three UFBG tests. The gratings have an initial peak-reflectivity of (a) 73%, (b) 84% and (c) 93%. (d)-(f) show the corresponding simulations, which are used to calibrate the raw data.

trace, has been integrated to get a distance–time plot. The two FBG measurements are shown in their calibrated, but unfiltered state and all three measurements have been manually overlaid for comparison.

When plotted side-by-side, all of the measurements appear to show a similarly linear trend, but the noise levels of the CFBG method become very noticeable in contrast to the narrowband UFBG and PDV results. It should be noticed, however, that the length difference between the FBG techniques exaggerates the relative noise difference in favour of the UFBG.

A more analytical comparison of the narrowband UFBG, CFBG and PDV measurement characteristics is given in Table 3.5.

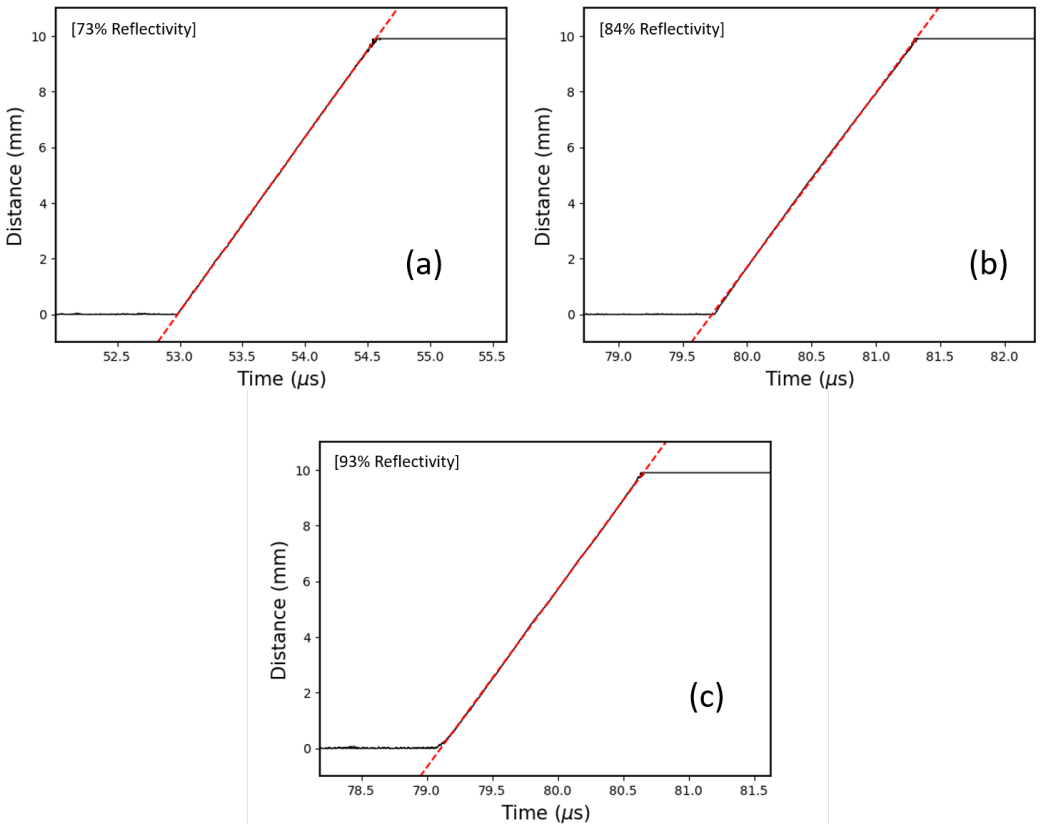


FIGURE 3.25: Plots of the fully calibrated UFBG test data. A linear regression has been calculated and plotted to show the linearity of the results, as well as to get an average velocity reading for each test.

In the "Velocity Difference" column, the average velocities from the CFBG and narrowband UFBG readings are compared with the PDV velocity, which is taken as the benchmark in this idealised scenario. By comparing the velocity difference with the uncertainty contributions from grating length and percentage noise, all but one of the FBG test velocities fall within their respective error range.

The anomalous result, from the 93% reflectivity UFBG, is likely to be due to a calibration error. This is because the calibration standard, plotted in Figure 3.24(f), assumes that the laser wavelength was tuned to *exactly* the Bragg wavelength. However, as discussed in Section 3.1.1, high-reflectivity UFBGs have a less well-defined, more rectangular resonance peak and so it is likely that the actual laser wavelength was offset from the Bragg wavelength.

The "Length Uncertainty" column quantifies how variable the lengths of each FBG could be. For the CFBGs, which were fabricated a few grating planes at a time, the length uncertainty is very low. However, optical time domain reflectometry (OTDR) data from batches of similar, phase-mask fabricated UFBGs, showed a variation in length of approximately $\pm 0.03$ mm.

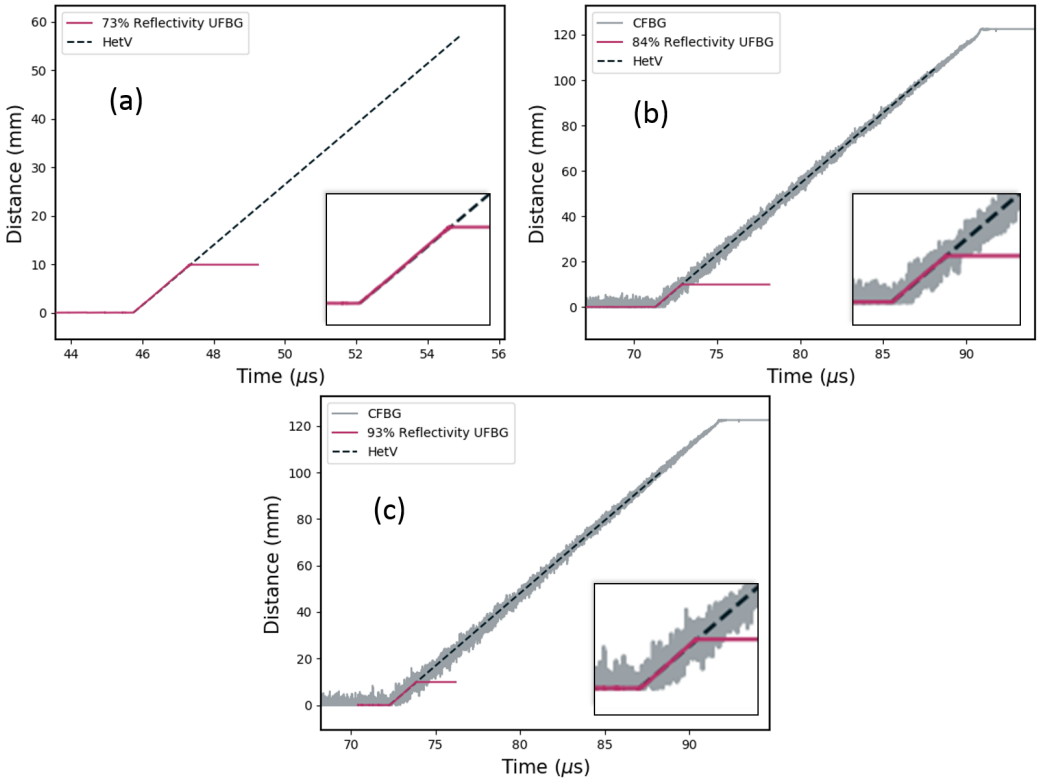


FIGURE 3.26: Plots comparing the PDV, CFBG and narrowband UFBG for each test. The results from each probe have been overlayed for comparison, and a magnification of the UFBG data is shown in an inset of each plot.

Finally, the "Noise Percentage" column shows the noise:signal ratio, which is based on the peak standard deviation of the signal, prior to detonation and without any post-processing.

Averaging across all three experiments, the UFBG peak noise comes out at ±0.077%. This is equivalent to a spatial uncertainty of ±7.6 $\mu$m for a 9.9 mm long grating. In comparison, the noise from the two CFBG tests averages to ±1.23%. This is equivalent to a spatial uncertainty of ±1.48 mm for a 120 mm long grating, or ±122 $\mu$m for a 9.9 mm long grating.

Considering the bit-depth of the DAQ (10-bit), it is likely that the spatial precision of this UFBG system is limited by quantisation error (to just under 10 $\mu$m). Equally, with an angular uncertainty of ±2°, the mounting precision is comparable in magnitude to the standard deviation noise levels.

In most practical circumstances, if the narrowband illumination system exhibits negligibly low optical noise, the acquisition hardware and/or mounting precision will provide the primary limiting factor on spatial precision. However, there is also a theoretical limit on the spatial precision, determined by the pitch of the FBG probe. In this case, with a Bragg resonance at ∼1550 nm, the minimum resolvable length change is around

| **Probe Type** | **Velocity** | **Velocity Difference** | **Length Uncertainty** | **Noise Percentage** |
|---|---|---|---|---|
| | $km/s$ | % | % | % |
| UFBG (73%) | 6.250 ±0.004 | 0.1 | ±0.3 | ±0.09 |
| PDV | **6.242** | – | – | – |
| UFBG (84%) | 6.247 ±0.006 | 0.0 | ±0.3 | ±0.08 |
| CFBG | 6.232 ±0.003 | 0.2 | $< 0.1$ | ±1.23 |
| PDV | **6.247** | – | – | – |
| UFBG (93%) | 6.396 ±0.01 | 2.5 | ±0.3 | ±0.06 |
| CFBG | 6.306 ±0.005 | 1.0 | $< 0.1$ | ±1.23 |
| PDV | **6.242** | – | – | – |

TABLE 3.5: Velocity comparisons between the PDV, CFBG and narrowband UFBG measurement techniques. "Velocity Difference" is the percentage difference between the grating probes and the PDV probe measurements. "Noise Percentage" is the noise:signal ratio for the data, based on the standard deviation of the signal prior to detonation.

500 nm. The only way to reduce this fundamental limit of FBG probes would be to lower the Bragg wavelength – the minimum length limit for an FBG in the visible range (e.g. 600 nm) would be around 200 nm.

Nevertheless, the low noise-levels demonstrated in this first implementation of the UFBG narrowband technique mark a considerable step toward the accurate measurement of shock-propagation over 10 $\mu$m length scales.

### 3.3.3 Design Summary

In this section, the optimal design parameters and practicalities of the narrowband UFBG setup are discussed.

#### *Reflectivity*

For narrowband UFBG measurements, the optimal grating should be around 50–80% peak reflectivity. If the reflectivity is too high:

- It will be difficult to set the probe wavelength at exactly the Bragg wavelength;
- The erasure shape will be very convex, making it particularly difficult to find the *start* of the erasure.

If the reflectivity is too low:

- The erasure shape will be very concave, making it particularly difficult to find the *end* of the erasure.

Fortunately, the total signal power can be tuned by amplifying/attenuating the input signal, so this does not need to come into consideration for FBG reflectivity.

#### *Length*

In theory, the narrowband UFBG concept is arbitrarily scalable. However, there are practical considerations which may limit its usable length.

First, long gratings have narrow bandwidths — a low-reflectivity, 100 mm long UFBG will have a bandwidth of around 16 pm, for example. In this case, a temperature fluctuation of just 1°C would offset the Bragg wavelength by almost an entire bandwidth, leaving the laser locked-on to a side-lobe. For this reason, if narrowband UFBG test lengths of over 10 mm are required, a peak tracking system is advisable. This is so that the laser automatically adjusts to any changes in the Bragg wavelength.

The second practical difficulty when using long UFBGs in the narrowband setup, is that the structure must remain coherent throughout. This means that any non-uniform strain or temperature across the grating, once mounted, will spoil the results. In some scenarios, therefore, it may be easier to use multiple shorter UFBGs, than to use one long UFBG.

## 3.4 Summary

For CFBG probes, which remain the longest FBG based detonation velocity probes so far, non-linearities based on fundamental bandwidth limitations can occur that result in an underestimation of the measured velocity. It has been demonstrated, using simulations and explosive cylinder tests, that this effect is mitigated if CFBG probes are designed with a high chirp-rate and a low reflectivity.

A new, low-noise alternative to the CFBG method, is the narrowband UFBG method. This method has been demonstrated, with an average noise-limited spatial precision of $\pm 0.077\%$ of the total length — just $\pm 7.6$ $\mu$m for a 9.9 mm long probe.

# Chapter 4

# Active Fibre Probes

It has been established that the low-profile, electromagnetically immune and chemically inert qualities of a standard optical fibre make it ideal as an embedded detonation velocity probe.

So far, a variety of FBG based sensing elements have been discussed, in which a narrow or broad bandwidth source is used to illuminate a grating and infer its length based on the total signal power that it reflects. These methods have been shown to yield detonation velocities to within 2% of the expected value, and with potential spatial uncertainties as low as $\pm 10$ $\mu$m.

However, FBG velocity probes are prone to the following weaknesses:

- FBGs are intricate periodic structures that are affected by non-uniform strain or temperature along their length. This means that, especially when testing consolidated charges, the fibre should be mounted with great care — probably requiring a level of expertise or training to perform properly.
- FBG erasures are not linear, but are some function of the grating design in combination with the power spectral density of the interrogation source. This may require an accurate simulation in order to calibrate the results effectively.

In this chapter, an alternative fibre optic technique for measuring detonation velocity is introduced. This method uses rare-earth doped fibre, in place of the FBG probes in Chapter 3, to create a velocity probe that is simpler, cheaper, more scalable and immune to non-linear strain.

This concept was first introduced in 1994 by Weiss [36], who used Neodymium and Phosphorous co-doped, elongated-cladding optical-fibre probes to measure shock propagation in up to 19 m lengths of detonating cord. Fan et al. [63], in 1995, adopted a similar technique, utilising Er doped fibres for slower, crack-detection applications.

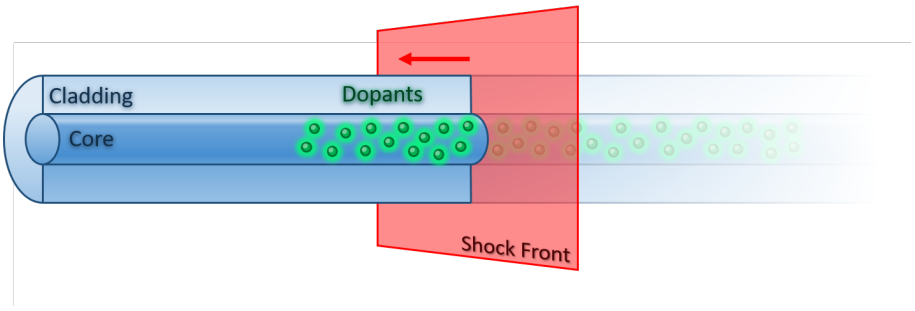


FIGURE 4.1: An illustration of the active fibre probe concept. As the fluorescent region of the fibre is destroyed, the total fluorescent power decreases because the rare-earth dopants are depleted.

The aim of the work presented here, is to demonstrate a linearisation of Fan et al.'s technique, using both standard off-the-shelf Er fibre, as well as some in-house fabricated high-concentration Er/Yb fibre. The concept is then extended to detonation velocity measurements, in both linear and non-linear geometries [64].

## 4.1 Concept

In the active fibre probe method, a length of rare-earth doped fibre is embedded into a test explosive and optically pumped, so that the rare-earth molecules begin to *spontaneously* emit photons at a longer wavelength.

When the detonation is initiated, the fluorescing fibre will be destroyed by the oncoming detonation wave, and the number of fluorescent molecules will be depleted. This concept is illustrated in Figure 4.1. If the total fluorescent power from the active region of the fibre is monitored at sufficient speed, then the progression of the detonation wave can be inferred.

The setup used for this technique is illustrated in Figure 4.2, where a pump diode illuminates a region of rare-earth doped fibre and any counter-propagating fluorescence is filtered out with a WDM coupler before being collected by a photodetector.

Conceptually, this system was designed so that the fluorescent power recorded on the oscilloscope was linearly proportional to the length of the active region. However, for this to occur, the following two effects must be balanced against one another:

- **Front-End Pump Absorption:** Since the pump light is absorbed by the ground-state rare-earth molecules, a lower pump power is received at the back-end in comparison to the front-end. If the initial pump power from the diode is too low, then a disproportionate amount of fluorescence will come from the front of the active region and the length-power relationship will be non-linear.

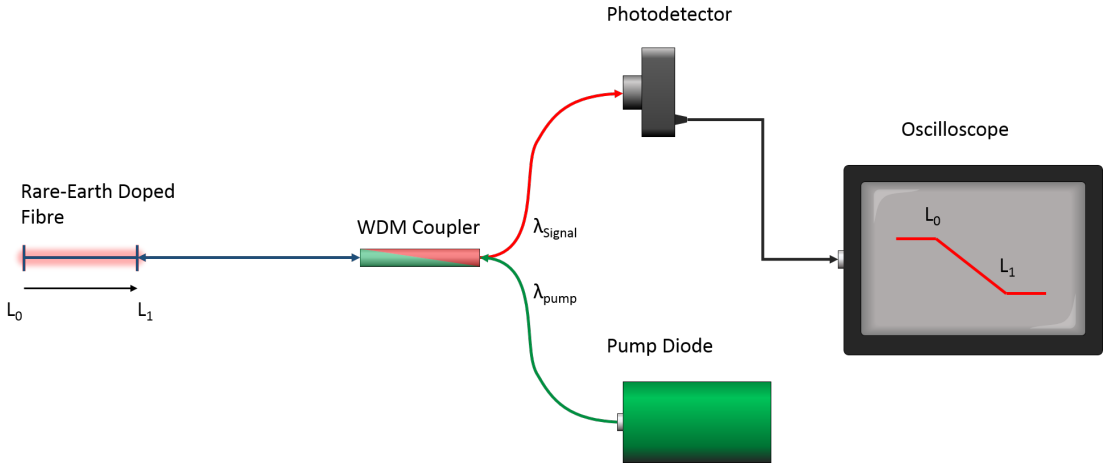


FIGURE 4.2: Schematic showing the basic setup for an active fibre detonation velocity probe. A Rare-Earth Doped fibre is pumped with a diode laser. The ASE fluorescence is filtered through a WDM coupler and collected on a photodetector.

- **Amplified Spontaneous Emission (ASE):** Due to the greater interaction length, photons emitted at the back-end of the active region are more likely to be amplified via the stimulated emission of front-end excited states. If the initial pump power from the diode is too high, then a disproportionate amount of ASE power will come from the back of the active region and the length-power relationship will be non-linear.

Optimising this setup to achieve a linear length-power relationship is a multi-variate problem, concerning: the choice of rare-earth dopant, the concentration of rare-earth molecules, the pump wavelength, the pump power and the length of the active region. Therefore, an experimental approach was taken in order to optimise/calibrate a variety of rare-earth fibres for velocity sensing — this is the subject of the following section.

Aside from the prospect of a good linearity, another benefit of using Er or Er/Yb doped fibres for detonation velocity measurements, is that the cost of each probe is dramatically reduced. Whilst a 10 mm long FBG could cost in the region of \$200[1], a typical Er-doped fibre might be found for only \$3.31–9.75[2] per meter.

Due to this reduced cost, as well as the long lengths of rare-earth fibre that can be drawn, the active fibre probe technique can be scaled to multi-meter lengths. Combined with the immunity of rare-earth fibres to non-uniform strain, this technique allows long velocity measurements to be carried out in interesting, non-linear geometries, and without specialist know-how.

[1]Based on a single unit quote from *O/E LAND INC.*
[2]Based on a quote from *Fibrecore* for <100m of their I-12 and I-25 fibres.

## 4.2 Cutback Tests

***Setup***

To verify the active fibre probe concept, a series of cutback tests were conducted. The setup for these tests is shown in Figure 4.2, with a 977 nm laser diode as the pump source and a power meter in place of the photodetector and oscilloscope.

Like the cutback tests carried out on the UFBG arrays (see Section 3.3), the essential idea was to destroy the probe incrementally using a razor blade, whilst monitoring the return signal on a power meter. Each time a length of the fibre was removed, the intact probe was re-measured, a drop of index matching fluid was applied to the exposed end and the total fluorescent power was noted down.

To assess the optimal pump power for a given probe length, dopant and/or dopant concentration, the pump power was adjusted several times after each cut to get multiple signal power readings. The aim of this process — finding the "optimal" pump power — is to see how linear an active fibre velocity probe could be and at what pump power maximum linearity occurs. Similar tests were conducted by Fan et al. [63] on Er doped fibre, although linearity was not the desired outcome in this case.

The three rare-earth doped fibres that were primarily used in this project are:

- Fibrecore's I-12 Er-doped fibre, with a pump absorption of 11.6dB/m at 980 nm. This fibre was used for probes of up to 1 m in length.
- Fibrecore's I-25 Er-doped fibre, with a pump absorption of 23.9dB/m at 980 nm. This fibre was used for probes of up to 10 cm in length.
- An in-house fabricated Er/Yb-doped fibre, with a pump absorption of >1000dB/m at 980 nm. This fibre was used for probes of up to 10 mm in length.

To be able to do cutback tests on short probes, with an initial length of 10 mm or so, a system was required that could measure length changes to within $\pm 100$ $\mu$m. This lead to the design and assembly of the setup shown in Figure 4.3.

In this case, an active fibre probe was fixed onto a steel plate, which was grooved to make sure that the fibre lay straight. The steel plate was placed onto a sliding stage, which could be adjusted using a digital micrometer. Above the sliding stage was a microscope with a camera unit that sent a live-feed to a television screen. Stuck to the television screen was a triangular piece of tape, with its tip pointing at the groove/fibre.

The cutback procedure was as follows:

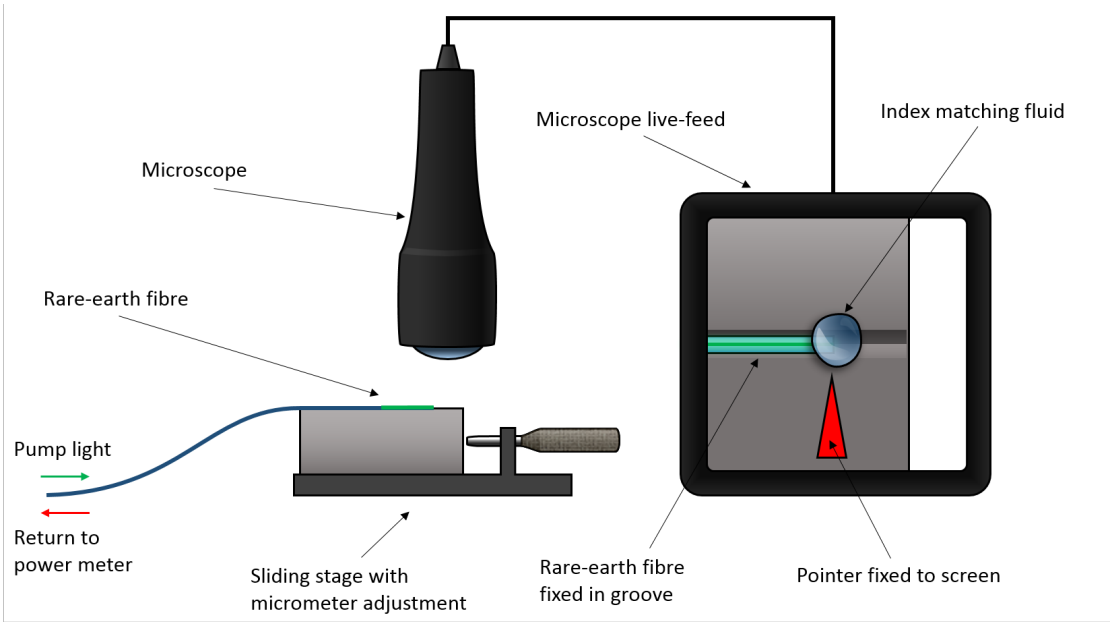


FIGURE 4.3: An illustration of the cutback measurement scheme used on short active fibre probes. This system allowed for at least 10 data points to be taken over a 10 mm length.

1. The micrometer stage was adjusted until the triangle on the screen pointed to the end of the fibre probe. The scale was set to zero.
2. A drop of index matching fluid was applied to the end of the fibre probe.
3. The pump diode was set to various output powers (monitored using a 50/50 splitter and a power meter), with the total fluorescent power measured in each case.
4. A small section of the fibre (typically <1 mm) was removed by a razor blade.
5. The micrometer stage was adjusted, again, until the triangle on the screen pointed to the end of the fibre probe. The micrometer readout was indicative of the length of fibre that had been removed.
6. Steps 2–5 were repeated until the probe was totally destroyed — noting down the length change of the probe each time.

### *Data*

The cutback data from a 1 m length of Fibrecore I-12 Er-doped fibre is plotted in Figure 4.4. Figure 4.4(a) shows the total fluorescence power as a function of the probe length, for the pump powers 0.8–6.6 mW. It is clear from this plot that a higher pump power corresponds to a higher total fluorescence power — this is due to an increase in the number of excited states throughout the Er-doped fibre region.

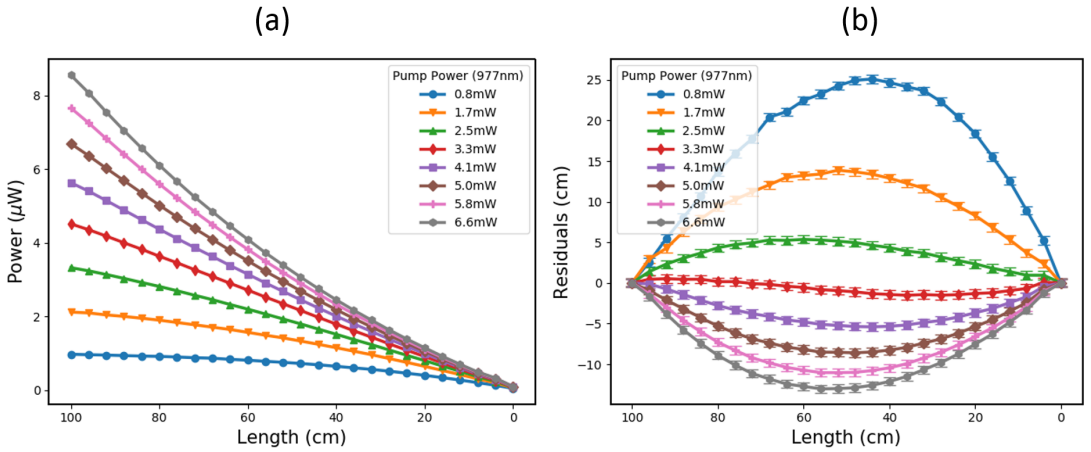


FIGURE 4.4: (a) Shows the ASE Power vs Length of a 1 m long Er-doped fibre (Fibrecore I-12) for a range of pump powers. (b) Shows the residuals compared to an ideal, linear Power vs Length relationship.

Figure 4.4(b) shows a residual plot of the cutback data, which reveals the characteristic shape of each pump power data set in Figure 4.4(a). Here, the effects of pump power absorption and ASE can be seen.

For low pump powers ($\leq$2.5 mW in this case) the power-length relationship is increasingly convex, as the front-end excited states absorb a greater proportion of the total pump light.

On the other hand, when the pump powers are higher ($\geq$4.1 mW) and the Er molecules are excited more uniformly along the probe length, the power-length relationship is increasingly concave. This is thought to be due to an accumulation of gain for photons emitted at the far-side of the probe, resulting in a higher total power contribution from the back-end.

Based on this data, it was determined that for a 1 m length of Fibrecore I-12 Er fibre, the pump power should be between 2.9–3.7 mW to ensure a good linearity (a residual fluctuation within approximately $\pm$2% of the full probe length).

The same cutback data for a high-concentration Er/Yb fibre is plotted in Figure 4.5. This data was collected using the micrometer stage setup (Figure 4.3) to get over 30 data points from a 10 mm length.

In this case, a considerably higher pump power range (from 6.6–24.1 mW) was required to be able to see the shape change from convex to concave. This is because the high-concentration Er/Yb fibre absorbs over 1000 dB/m of 980 nm pump light. The optimal pump power for this fibre was found to be between 14.1–16.6 mW.

One other difference between the high concentration Er/Yb fibre and the Fibrecore I-12, is the fluorescent power per unit length. For a 3.3 mW pumped I-12 fibre, the total

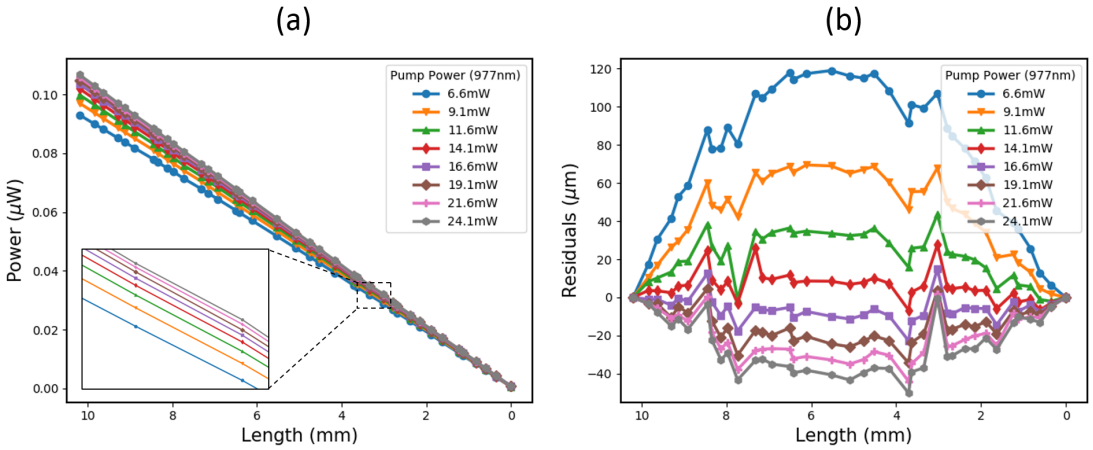


FIGURE 4.5: (a) Shows the ASE Power vs Length of a 10 mm long, high concentration (>1000 dB/m @ 980nm) Er/Yb-doped fibre for a range of pump powers. (b) Shows the residuals compared to an ideal, linear Power vs Length relationship.

| **Fibre** | **Absorption** dB/m (@980 nm) | **Pump Power** mW | **Length** cm | **Initial Power** (Approx.) |
|---|---|---|---|---|
| Fibrecore I-12 | 11.6 | 2.9–3.7 | 100 | -25 dBm |
| Fibrecore I-25 | 23.9 | 2.5–3.3 | 10 | -32 dBm |
| In-house Er/Yb | >1000 | 14.1–16.6 | 1 | -40 dBm |

TABLE 4.1: Comparison of optimal parameters (pump power and length) for three fibres with different pump absorption: **Er Fibrecore I-12** (11.6 dB/m), **Er Fibrecore I-25** (23.9 dB/m), **in-house fabricated Er/Yb** (>1000 dB/m).

power measured from a 1 m length was approximately 4.5 $\mu$W. This gives a power per unit length of 4.5 nW/mm. For the high-concentration fibre, the total power measured from a 14.1 mW pumped, 10 mm length, was approximately 0.1 $\mu$W. This corresponds to a power per unit length of 10 nW/mm — over double that of the I-12 fibre.

This analysis was also repeated for a 100 mm length of Fibrecore I-25 fibre. A full summary, giving the optimal pump power for the I-25, I-12 and the high-concentration Er/Yb fibre is shown in Table 4.1.

This table shows the length at which each fibre could achieve a linear length-power response (maximum residuals within 2% of the total length). For longer lengths, the residuals become increasingly S-shaped as the effects of pump absorption and gain accumulation combine.

Using these values as guidelines, the active fibre probe method was ready to be tested properly as a detonation velocity sensor, in a series of cylinder tests (see Section 2).

## 4.3 Explosive Testing

***Setup***

The interrogation setup that was used to test the active fibre method is shown in Figure 4.2, with the addition of a 50/50 coupler inserted immediately after the pump diode in order to monitor the pump power. The pump diode operated at 977 nm.

To monitor the fluorescent signal, a 125 MHz New Focus 1811-FC detector was used in conjunction with a 1.25 GSamples/Second, 10-bit National Instruments PXIe-5160 DAQ system.

Due to the differences in usable length between each of the three rare-earth fibres, two different techniques were required in order to mount them to the test cylinder. The high-concentration Er/Yb fibre and the Fibrecore I-25 fibre were both mounted in the top of the lid using a stainless steel tube, as described in Section 2. These probes were 10 mm and 100 mm long, respectively.

To show the scalability of this technique and to maximise the available fluorescence power, the Fibrecore I-12 fibre was mounted on the *outside* of the cylinder, in a helical geometry. The full length of the probe was approximately 1 m, so that it could be wrapped around ∼10×, with a vertical displacement of 10 mm per wrap. A photograph of the helical setup is shown in Figure 4.6.

This arrangement demonstrates a 10× magnification of the spatial precision in the shock propagation direction — an implementation that would be much more difficult to achieve using strain sensitive FBG probes. In the extreme case, a wrapping displacement of 125 $\mu$m could be used to get an 800× magnification in the spatial precision (dependant on the speed of the interrogation hardware).

Alongside each active fibre probe, in the centre of the cylinder, a length of standard un-doped fibre was mounted in order to get a comparative PDV measurement.

***Data***

Due to the low signal power from the Fibrecore I-25 and the high-concentration Er/Yb fibre probes, no discernible signal was detected from any of these tests. This was primarily due to the choice of detector (New Focus 1811-FC), which was incorrectly identified as having a low noise floor (∼-45dBm), but actually had a higher noise floor than the comparable Thorlabs detector used in the FBG tests (see Section 2 for a comparison).

Results from an earlier set of pilot tests, which were conducted using the Thorlabs PDA10CF detectors, yield a small erasure signal after low-pass filtering is applied. Figure 4.7 shows the 20 MHz low-pass filtered DAQ signal from a 100 mm long Fibrecore

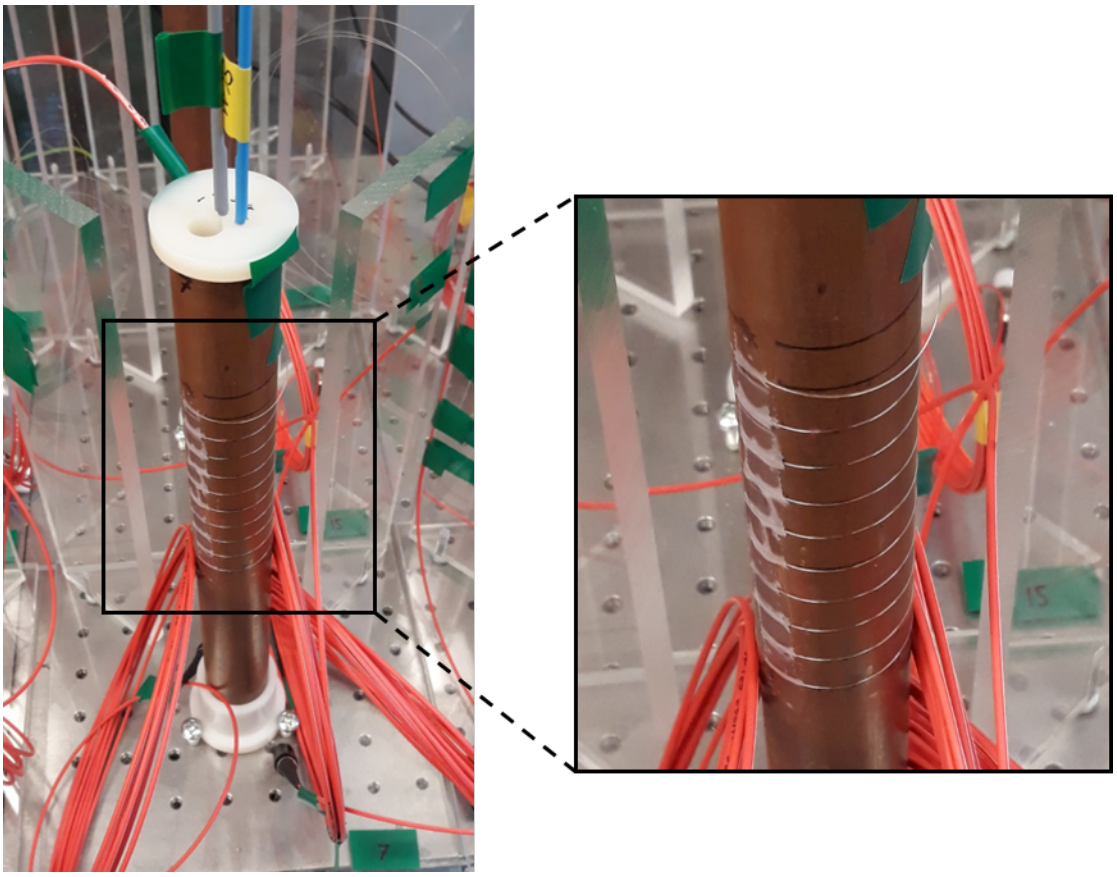

FIGURE 4.6: Photograph showing the cylinder test setup, with a 1m length of Er-doped fibre wrapped around in a helix.

I-25 probe. The erasure of the probe can be seen between approximately 25–35 $\mu$s and gives an erroneous velocity of over 8 km/s when fully processed. In the raw, unfiltered data, a very high noise level is present, with a standard deviation of over ±60% — this corresponds to a spatial uncertainty of over ±60 mm.

A noticeable feature in many of the active probe tests, and especially in Figure 4.7, is that there are spurious signal fluctuations before and after destruction. Between 0–25 $\mu$s, the signal appears to increase prior to the shockwave reaching the probe. After 35 $\mu$s, a large spike is seen that is larger in amplitude than the original signal level prior to destruction. The origin of these effects is unknown.

Due to the length of the helical Fibrecore I-12 probes, a significantly higher total signal power was achieved — the initial signal power, when the pump power was set at an optimal ∼3.2 mW, was over 10 dBm greater than from the 10 mm long Er/Yb probe.

The calibrated and 20 MHz low-pass filtered data from these tests is shown in Figure 4.8. Since the I-12 fibre probes had been setup to receive an optimal pump power, the conversion of voltage to distance was particularly straight forward. Assuming that the power-length relationship was approximately linear, the voltage-time data could be

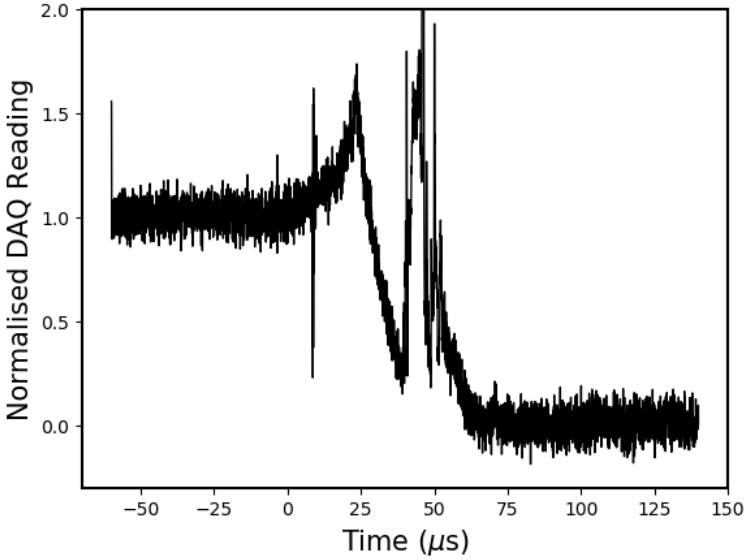


FIGURE 4.7: Plot showing the 20 MHz low-pass filtered DAQ signal from a 100 mm long Fibrecore I-25 active probe test. The shockwave is detected in the range 25–35 $\mu$s, with spurious signal fluctuations either side.

normalised to give the fraction of the remaining probe length. This could then be multiplied by the initial length of the probe to get the distance-time progression of the traversing shock-front.

Alongside the active fibre probe data, an integrated PDV trace from the same test is shown in Figure 4.8 as a red dashed line. Upon visual inspection, these two data sets appear to show a similarly linear trend — an indication that the pre-test linearisation of the probes was successful.

By taking a linear regression fit of both the PDV and active fibre probes, an average detonation velocity can be acquired and compared. From the two PDV probes, which are taken as the benchmark for these tests, the average velocities were found to be 6.25 km/s and 6.24 km/s. The velocities measured from the corresponding helical probes were 6.37 km/s and 6.34 km/s respectively, which are offset from the PDV measurement by +1.9% and +1.6%. This discrepancy is likely to be due to the ±2.5% uncertainty in the probe length, which is a result of the practical difficulty when mounting the fibre in a helical arrangement.

Whilst both plots in Figure 4.8 are from nominally identical tests, a substructure in Figure 4.8(b) is particularly noticeable and appears to correspond to the ten turns of the helical probe. This was not setup intentionally, but it does demonstrate the ability of these sensors to measure changes in velocity over a 10 cm length scale (or just 1 cm length scales in the direction of the shockwave propagation).

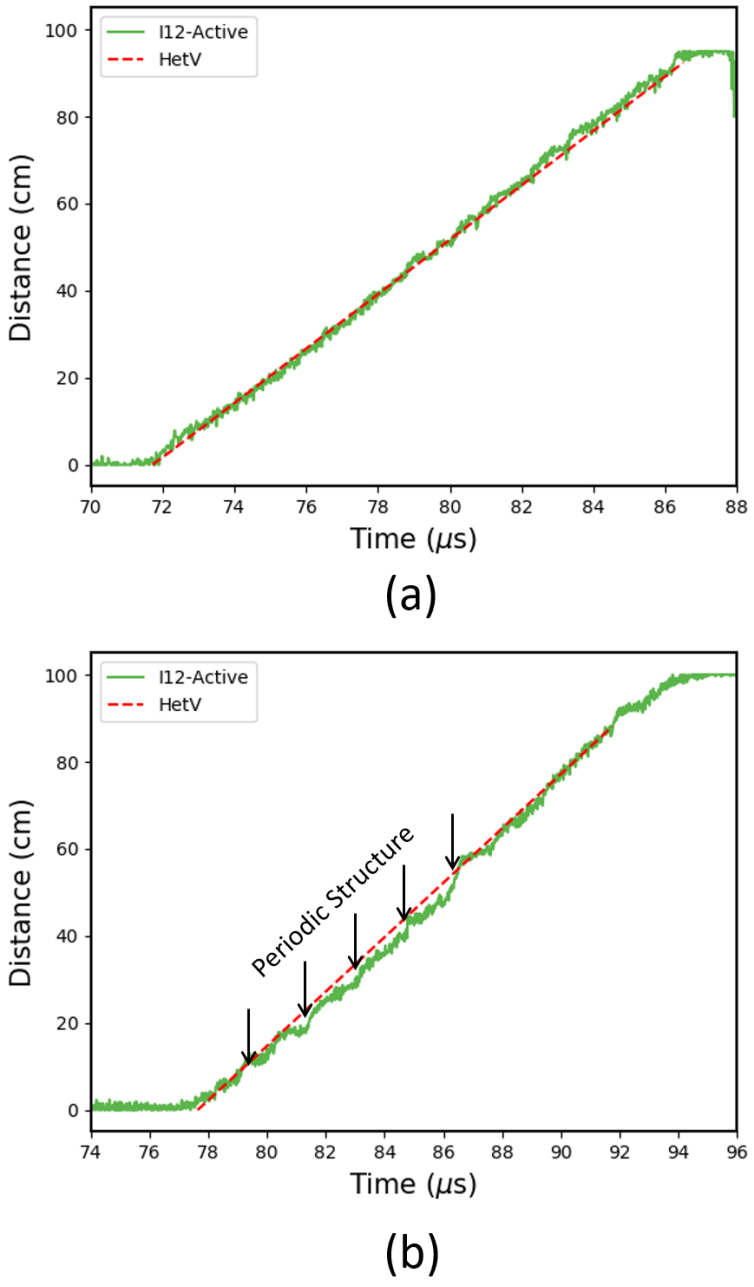


FIGURE 4.8: Plots showing the data from two 1m long Er-doped fibre detonation velocity tests (Fibrecore I-12). For comparison, the data has been overlaid with the corresponding PDV results. The results shown in (a) and (b) are from two nominally identical cylinder tests. However, a substructure, thought to be due to the helical mounting geometry, is particularly present in (b). This data has been calibrated and low-pass filtered (20 MHz cutoff).

By taking the standard deviation of the signal noise from these cylinder tests, an indication of the maximum spatial uncertainty for the helical Fibrecore I-12 probes can be obtained. This analysis was done on the unfiltered, raw data, and repeated after a 60 MHz and 20 MHz low-pass filter had been applied. The results give a percentage uncertainty of approximately ±1.6% (unfiltered), ±1.2% (60 MHz low-pass) and ±0.6% (20 MHz low-pass) — this is essentially the noise/signal ratio and appears to be fixed even after the probe is destroyed, indicating that the noise is primarily electronic. In the direction of the shock propagation, where the total measurement length is 0.1 m, this corresponds to a maximum spatial uncertainty of ±1.6 mm in the unfiltered case, ±1.2 mm in the 60 MHz low-pass filtered case and ±0.6 mm in the 20 MHz low-pass filtered case.

The uncertainty due to the calibration residuals is in a similar range, at around ±2 mm. These are shown in Figure 4.4, and contribute to the uncertainty because the probe was assumed to be linear in post-processing.

Similar results were obtained in crack detection tests by Fan et al. [63], who managed a statistical error of just under 3 mm over a 0.4 m length. In these tests, however, the measurements were taken using an optical spectrum analyser instead of a fast photodetector and the fibre was pumped at higher power since linearisation was not desired.

Whilst similar analysis was not done explicitly for the Nd/P doped fibres used in Weiss's work [36], it is our estimate, based on an inspection of the data presented, that the signal to noise ratio as a percentage was significantly higher, with a noise level in the region of ±0.1%. However, over the 18–19 m lengths tested, this corresponds to a spatial uncertainty of around ±18–19 mm, an order of magnitude higher than the helical tests demonstrated here.

## 4.4 Summary

An active fibre probe system, utilising off-the-shelf Er doped fibre has been demonstrated, measuring detonation velocity to a precision of $\sim \pm 2$ cm in a 1 m length test. By utilising the strain insensitivity of this measurement scheme, the fibre probe was able to be mounted in a helical geometry which amplified the spatial precision by a factor of ten, resulting in a ±2 mm spatial precision over a 10 cm range.

As a future prospect, a highly doped Er/Yb fibre velocity probe was also demonstrated in a specially designed cutback test. The probe demonstrated high linearity (residuals within around ±20 $\mu$m) over a 1 cm measurement range and double the fluorescence power per unit length, in comparison to the Er fibre used in the explosive tests.

# Chapter 5

# Comparative Study

The aim of this section is to make a comparison between the CFBG, UFBG and active fibre probes in the context of existing technology. Section 5.1 breaks down a variety of existing techniques and discusses which of the FBG or active probes might be a suitable (or better) alternative.

After this, multiple improvements and new techniques are discussed, which could improve the reliability and accuracy of these systems in the future.

## 5.1 Detonation Velocity Probes in Context

***Discrete TOA Devices***

Discrete TOA sensors are some of the earliest detonation velocity sensors to have existed (such as the D'Autriche method [8]) and still offer the most reliable determination of average detonation velocities. This is due to the simplicity of their construction, their commercial availability and their insensitivity to strain/temperature gradients.

In these methods, the measurement range is determined by the distance between the two terminal probes, the spatial resolution is determined by the separation of each adjacent probe and the measurement accuracy is determined by the probe width, spatial positioning accuracy and the rise-time of the back-end hardware.

Measurements of this kind must often compromise between spatial resolution and measurement range, owing to the impracticality of fixing hundreds of probes. Shinas and Doty [24], for example, demonstrate a high spatial resolution of 250 $\mu$m over an area of 1.25 x 1.25 mm. For similar, short length scale tests using an embedded sensor, the UFBG technique is a promising contender.

Whilst both CFBG and UFBG methods can achieve spatial resolutions $\leq$250 $\mu$m, the UFBG is likely to be capable of higher resolutions over a 1 mm measurement range. In this case, according to the results in Section 3, a spatial uncertainty of $\sim$1 $\mu$m is possible using a UFBG — the equivalent CFBG resolution would not scale down so easily, because restrictions on the bandwidth of a 1 mm grating would drastically reduce the signal power.

Alternatively, discrete TOA methods can be scaled up to measure average detonation velocities — in particular, steady-state velocities. In this case, a long measurement range is desirable to maximise the accuracy of the average velocity reading. For these applications, discrete TOA methods are particularly well suited.

It is in the centre ground that CFBG and active probes may be particularly useful. For measurement ranges in the 1–10 cm range, CFBG's offer a resolution in the tens of microns, whereas active fibres can be implemented from 10 cm upwards with resolutions demonstrated in the mm–cm range. It is unlikely that discrete TOA methods can compete with these resolutions over comparable length scales.

#### *Streak Cameras*

Streak cameras are capable of very high temporal resolution measurements over short distance scales. Their measurement range is determined by the smear-rate of their rotating mirror or deflection plates, in combination with the film or sensor size at the back-end. The spatial resolution is determined by the smear-rate and the film or sensor resolution and the measurement precision is affected by the quality of the image that is formed.

Over the typical length range of a streak camera ($\sim$cm) and with spatial resolutions on the order of 0.1% of the measurement range, the UFBG is the closest competitor of the three techniques described here. However, whilst the measurement ranges and resolutions of the two techniques are similar, there are significant practical differences.

First, the UFBG technique is destructive — a UFBG probe can only be used once. This means that the costs accumulate over time, in comparison to the one-off purchase of a streak camera. Commercially available streak cameras can often be bought as integrated units, without the need for additional hardware, so for a fair comparison, the requirement for a high-speed DAQ/oscilliscope should also be added to the cost of the UFBG system. Both methods, therefore, are likely to be costly — especially when spatial resolutions in the tens of microns are desirable.

Secondly, streak cameras require a direct sightline to their subject. For detonation velocity measurements, where direct access to the explosive fluorescence is required, streak cameras may be impractical to use — especially in confined spaces or underground

tests. The UFBG method is not limited in the same way, because it is an embedded sensor. However, its implementation may still be limited to applications in which the probe can be fixed reliably, without strain or temperature gradients along its length.

### *PDV*

As discussed in Section 1.3, PDV techniques are most often used to measure surface velocities — not for the continuous monitoring of a propagating shock-front. However, the reliability of the technique for liquid explosive tests, especially when it is mounted centrally so that the wave fronts are approximately plane, mean that it could be taken as the bench mark in the experiments described here.

All three techniques described in this project are embedded sensors that have been developed to measure detonation velocity in interesting geometries and in consolidated charges. In these scenarios, the PDV method is likely to fail. However, a proposal for a solid-compatible PDV technique, as well as a multicore PDV method are discussed in Section 5.2.

### *Continuous TOA Devices*

Continuous TOA devices are the most versatile detonation velocity measurement systems, because they can be embedded within an explosive and in a variety of geometries. The measurement range of a continuous TOA device is determined by the length of the probe, the spatial resolution is determined by the temporal resolution of the DAQ hardware and the precision is determined by the signal/noise ratio, quantisation error and calibration accuracy.

The three methods discussed in this project are the current contenders for fibre optic continuous TOA devices. They are particularly suited to embedded sensing, because of their small cross-sectional area in comparison to most electronic equivalents. A typical un-coated fibre has a diameter of 125 $\mu$m, whereas a coaxial continuous resistance probe might have a diameter in the mm scale [65].

Of the three fibre optic techniques reported in this project, the highest spatial precision has been demonstrated with the UFBG method. The data from Section 3.3 shows a precision of $\sim \pm 0.1\%$ of the measurement range. Based on the theoretical discussions surrounding the erasure characteristics of a UFBG — mainly that the erasure shape is dependant only on the initial reflectivity — it is clear that this precision is length invariant. This means that a 1 mm long UFBG is capable of 1 $\mu$m spatial precision (depending on the limitations of the acquisition hardware and mounting technique).

However, the UFBG concept has yet to be demonstrated for lengths above 10 mm. This is because the bandwidth of a UFBG becomes narrower as the probe length increases,

making it more difficult to manually tune a laser diode to its Bragg wavelength. The greatest measurement range, using an FBG probe, that has been demonstrated so far is the 24 cm long CFBG test shown in Section 3.2.

In the case of a CFBG probe, the bandwidth *increases* for longer lengths (at a fixed chirp-rate). This, in combination with the broad bandwidth interrogation scheme makes the CFBG method more easily scalable. For length scales in the range 1–10 cm and above, the CFBG probe is proven to be capable of a measurement precision in the region of 50 $\mu$m–1 mm [35].

For very long length measurements on the 1–10 m scale, the active fibre probes show great promise. This concept has previously been demonstrated in lengths up to 20 m, with a spatial precision in the cm scale. In Section 4, a 1 m length of off-the-shelf Er fibre was also tested with a measurement precision in the cm scale.

In this case, the spatial precision was amplified by the implementation of the probe in a helical geometry. Whilst this is conceptually plausible for any continuous TOA device, the strain insensitivity of the active fibre probe makes it particularly simple to mount in these non-linear regimes.

Of the three methods presented in this project, the active fibre probe is the most insensitive to strain. In second is the CFBG method, which is as sensitive to spectral degradation as the UFBG method, but with less extreme consequences. If small, random strains are applied to a CFBG when it is mounted on an explosive, then a LUNA or OSA measurement can be taken and these effects can be mitigated in post-processing.

However, the UFBG system is sensitive to strain to the extent that it is unusable if a near-ideal reflection spectrum is not preserved. For a 10 mm long FBG, with a bandwidth of approximately 160 pm, a 0.0067% strain variation corresponds to a resonance shift of half the bandwidth. Equally, a temperature gradient amounting to an $\sim 8$ °C change would have a similar effect.

## 5.2 Future Work

***Active Fibre Probes***

So far, the active fibre probes have been introduced as a low-cost, scalable velocity sensor for applications that do not require sub-mm spatial resolutions. However, this is primarily due to the low signal powers that they generate, which can't yet be measured using commercially available high-speed photodetectors.

In fact, the cutback tests performed on a 10 mm length of high-concentration Er/Yb fibre demonstrate the potential of these probes to make measurements approaching a

precision of ±20 $\mu$m. However, with a power per length of 10 nW/mm, a distance change of 20 $\mu$m corresponds to a change in the fluorescent power of just 200 pW.

If it were possible to measure such low powers at 100 MHz speeds, the active fibre probe would offer a spatial precision that is competitive with the UFBG method, but at a lower cost and, crucially, without the inherent strain sensitivity.

Alternatively, the low levels of fluorescent power could be amplified up to a level that can be measured using conventional photodetectors. This has already been attempted using erbium doped fibre amplifiers (EDFAs) with no success — the amplifier noise was too high and the input signal power was too low to measure any changes in the total fluorescence.

#### *UFBG Probes*

The UFBG probes that have been demonstrated in this project are 10 mm long, with a bandwidth of around 160 pm. In order to improve the measurement range of this method, an automatic peak-tracking system is required so that the laser can be locked on to the Bragg wavelength.

With an FBG thermal sensitivity of around 10 pm/°C, a change in temperature of 1°C is enough to totally de-tune the interrogating laser wavelength from a 100 mm long UFBG. In explosive tests, where safety regulations may require control areas to be evacuated prior to detonation, slight adjustments to the laser wavelength cannot be made immediately before initiation and should, therefore, be made automatically. This would improve the safety and accuracy of the laser tuning, and make longer UFBG probes more feasible.

An appropriate method for locking the laser wavelength to the Bragg wavelength could be the Pound-Drever-Hall technique [66]. In this technique, the laser frequency is modulated across a small section of the grating reflection spectrum, so that the signal power reflected from the grating varies at the same frequency. By comparing the phase of the wavelength modulation and reflected power signal, it can be determined whether the laser wavelength is above or below the Bragg resonance. This information is used to adjust the DC-offset of the wavelength modulation and converge on the peak reflection point.

#### *FBG PDV*

Throughout this project, it has been discussed that the PDV method for measuring detonation velocity is restricted to liquid explosive tests. This is because the method

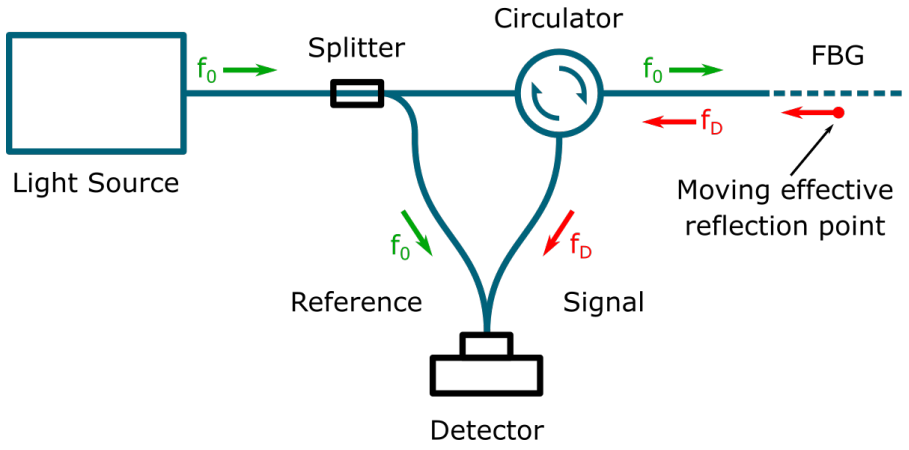


FIGURE 5.1: Schematic showing the operating principle of an FBG based photonic doppler velocimeter (PDV).

relies on picking up Doppler shifted Fresnel reflections from the end facet of the fibre — a process that requires the end facet to be as perpendicular as possible.

An alternative technique, that is thus far untested, is to use an FBG as the feedback element in a PDV system. This concept is demonstrated in Figure 5.1.

In this system, an FBG is embedded in a test explosive and a laser is tuned to its Bragg wavelength. A coupler is then used to mix the output frequency of the laser, with the reflected signal frequency from the FBG. This frequency mixture is collected on a photodetector where, like in a standard PDV measurement, any discrepancy between the signal and reference frequency will result in a beating pattern.

When the FBG is destroyed by an oncoming detonation wave, the *effective reflection point* of the grating will move closer and closer to the detector. It is thought that this process will result in a Doppler shifted return frequency that is proportional to approximately half the detonation velocity.

### *Simultaneous Sensing*

Throughout this project, emphasis has been given to the principle of simultaneous sensing. This is particularly evident in the explosive testing phase, where multiple probes were mounted side-by-side. In Section 3.3 a PDV, UFBG and CFBG probe were fielded simultaneously, with the results overlaid for comparison.

This kind of simultaneous testing should not just be limited to the validation of new detonation velocity sensors, because it can also be used to improve the reliability of measurement results. By comparing multiple probe readings and removing any spurious data points, a more accurate picture of the shock-wave dynamics can be gleaned. This is especially important when measuring new phenomena.

To this effect, fibre optic measurement techniques are capable of *multi-core sensing*. Multi-core fibres can be regular, single-mode fibres that are only 125 $\mu$m in diameter, but that contain a number cores, separated by a few tens of microns. If, for example, a 10 mm UFBG could be written into each core, then five or more simultaneous measurements of detonation velocity are possible over a near identical spatial region and with a spatial precision of $\pm 10$ $\mu$m.

This same concept could easily be extended to both free-space and embedded PDV measurements, with the additional possibility of using rare-earth doped multi-core fibres to increase either: **(1)** The number of simultaneous measurements, by separately monitoring the fluorescence from each core or; **(2)** The total signal power, by combining the fluorescence from each core and monitoring it on a single photodetector.

# Chapter 6

# Conclusions

The initial aim of this project was to explore fibre optic methods for measuring detonation velocity. More specifically, the aim was to build upon the recent successes of the chirped FBG probe and develop embedded, *continuous* time-of-arrival velocity probes which are capable of an even higher spatial precision and resolution.

To this end, three distinct concepts were investigated and trialled — each with their own advantages and disadvantages.

The first concept was to build upon the existing CFBG velocity measurement system and to use simulations to optimise the grating design. It was discovered, using T-matrix simulations, that CFBGs were prone to non-linear bandwidth effects which would tend to underestimate the velocity of a detonation.

However, by appropriately designing a CFBG, with a low reflectively and a high chirp-rate, it was demonstrated, both in simulation and in practice, that these effects can be largely mitigated. In addition to this, a 24 cm long CFBG was trialled in a cylinder test — demonstrating the longest FBG based detonation velocity measurement so far.

The second concept that was pursued throughout this project was the uniform FBG velocity probe. This new system was initially investigated as a simpler and more scalable alternative to the CFBG method, using the same broadband interrogation scheme. However, further experimentation found that the use of a narrow bandwidth interrogation source, fixed on the Bragg resonance of a UFBG, yielded particularly low-noise results. Based on noise alone, the data collected from the UFBG explosive tests showed a spatial uncertainty of less than 10 $\mu$m.

Whilst this new scheme was not demonstrated over the same length scales as the CFBG probes, the maximum optical noise levels were shown to be an order of magnitude lower.

Finally, the third concept that was tested throughout this project was the Er and Er/Yb doped fibre velocity probe. This system was investigated due to its immunity to adverse

strain effects, low cost and simplicity. Initial testing of these fibre probes was done in non-explosive conditions, using a razor blade, in order to pre-calibrate the probes to respond as linearly as possible. This was done by adjusting the length of the active region, as well as the pump power level.

The flexibility and scalability of this technique was demonstrated by fielding off-the-shelf Er doped fibres in a helical geometry, where a 1 m length of fibre was used to measure a 0.1 m region of shock propagation. The spatial precision in this case was around $\pm 2$ mm.

An active fibre probe which was not successfully trialled in explosive tests, but which showed promise during laboratory cutback tests, was a high concentration Er/Yb fibre. This fibre showed a good linearity, with a residual fluctuation of around $\pm 20$ $\mu$m over a 10 mm length scale, but the total fluorescence power was too low to pick up on the 150 MHz photodetectors.

Together, the combination of all three of these concepts demonstrate a significant step forward in the development of embedded fibre optic detonation velocity probes. A higher than ever spatial precision has been demonstrated using UFBG probes. The longest continuous CFBG shock velocity measurement has been demonstrated, using an optimised grating design. A low-cost and strain insensitive measurement system has been demonstrated using off-the-shelf Er doped fibres.

# Appendix A

# UFBG Simulation and Calibration Software

A Matlab app was created in order to simulate UFBGs and calibrate narrowband UFBG test data. Figure A.1 shows the first section of the app, which asks the user to enter an FBG length, Bragg wavelength, peak reflectivity and wavelength offset. When the "simulate" button is pressed, a grating spectrum and an erasure plot are displayed in the graphs underneath. These simulations are calculated using the T-Matrix method.

The intention of this section of the app was to allow non-specialists to get some idea of the grating spectrum that they can expect for a UFBG of a specified reflectivity — How rectangular is the shape? What is the bandwidth? How high are the side-lobes? The "Wavelength Offset" input also allows the user to visualise the effect of misaligning the narrowband laser wavelength.

Figure A.2 shows the calibration section of the Matlab app. In this part, the user is invited to load in oscilloscope voltage data from a narrowband velocity test. Using the dials on the right-hand side, they may then set the region of interest on the time scale and the start and end voltages on the signal scale. The "Cut" button removes data outside the region of interest and the "Normalise" button uses the start and end voltages to normalise the data.

If the grating simulated in the previous section (Figure A.1) corresponds to the grating used to acquire this data, then the "Calibrate" button can be pressed. This will compare the normalised simulation with the normalised test data and return a distance-time graph of the shock-front propagation.


FIGURE A.1: Screenshot of the UFBG simulation section of the Matlab app.

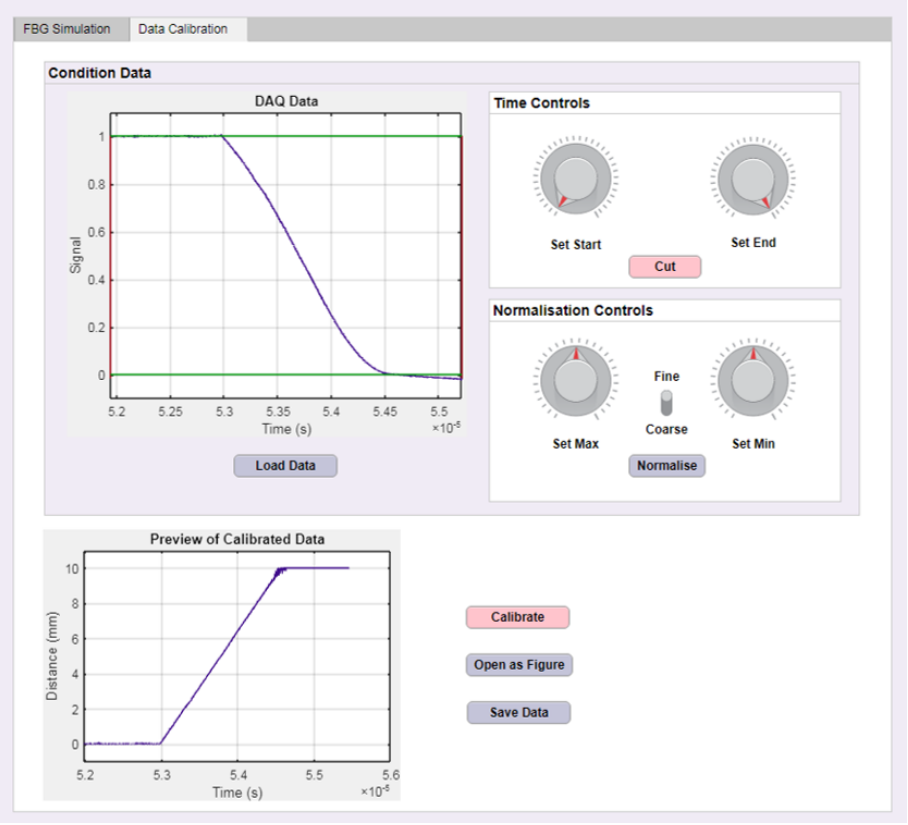


FIGURE A.2: Screenshot of the data calibration section of the Matlab app.

# Appendix B

# Lightweight PDV Software

In every single cylinder test done as part of this project, a PDV measurement was taken in order to verify the results of the new methodologies.

In a PDV measurement, a light signal from a coherent source is used to illuminate a moving target. The reflected light that comes from this target is Doppler shifted with respect to the input signal. By capturing the reflected light and interfering it with a reference wavelength, a beat frequency is generated that is proportional to the velocity of the target.

In these experiments, the beat frequency is captured on a fast photodetector (at least 12 GHz bandwidth), and recorded as a voltage trace on an oscilloscope. To interpret this voltage trace in post-processing, a simple Python program was created.

The interface of this program is shown in Figure B.1. In order to create a readable velocity-time graph from the recorded voltage data, a fast fourier transform (FFT) is carried out that can extract the beat frequency.

This FFT process is done in a series of time windows, so that a beat frequency can be attributed to a specific time step. Before an FFT can be performed on a window, however, the amplitude of the voltage signal must be filtered — this prevents spurious high-frequencies appearing due to discontinuities at either end of the window.

The program in Figure B.1 allows the choice of five different filter shapes. Underneath the filter shape section, the user may select a “Window Size”, which sets the number of data points taken per window. The “Overlap Factor” sets the fractional overlap with adjacent windows, where 0 represents back-to-back windows (no-overlap).

Finally, the user may choose a zero-padding level. This is the number of zeroes added to the end of each window — a process that artificially increases the frequency resolution of an FFT. At the bottom of the “Set FFT Window Specs” box, there is feedback given to the user based on their choice of input parameters. The “Waveform Frequency

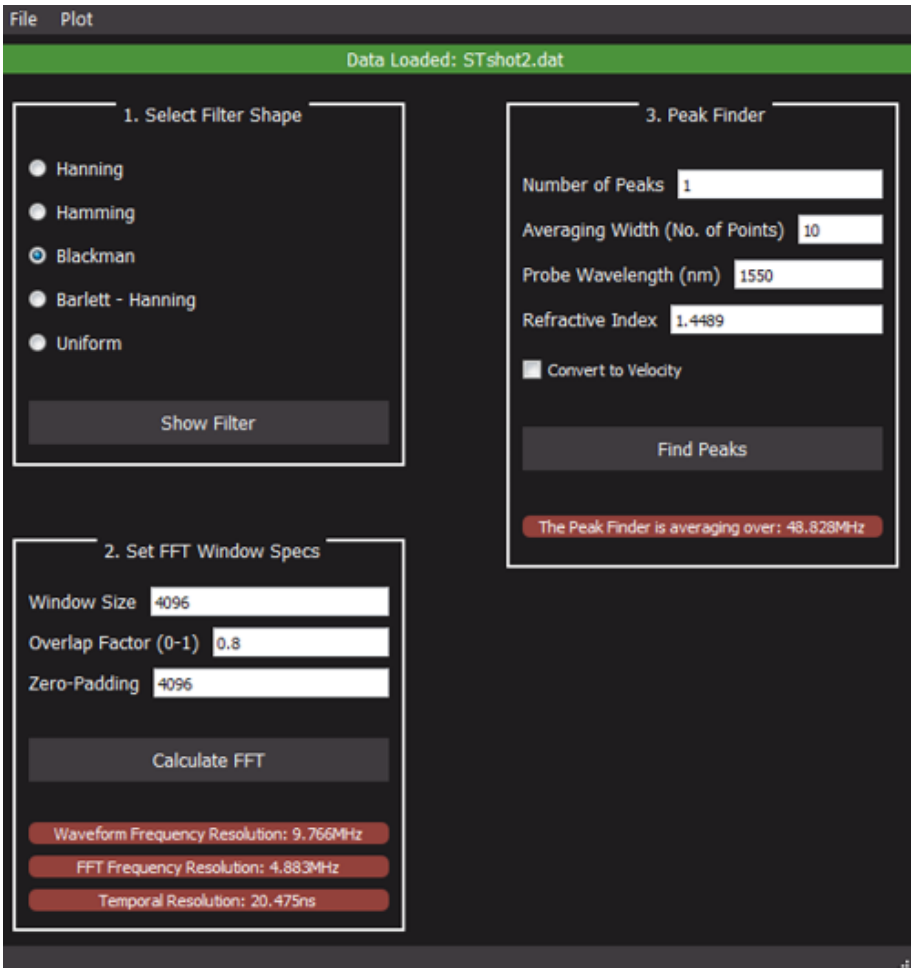


FIGURE B.1: Screenshot of the PDV interpreter.

Resolution" gives the *real* frequency resolution and is determined by the window size. The "FFT Frequency Resolution" gives the artificial resolution, based on the additional zero-padding to each window (terminology has been taken from this article [67]). The "Temporal Resolution" is based on the overlap factor, and gives the time difference between each window.

Once this has all been set, an oscilloscope trace can be loaded in and the "Calculate FFT" button can be pressed. This generates a frequency heat-map, like the one shown in Figure B.2(a). In this plot, the beat frequency can be seen as a peak in the heatmap, forming a horizontal line.

The user can select the region of interest and re-adjust the input parameters as they wish, until the beat frequency is well defined. At this point, the "Peak Finder" box can be used to extract the beat frequency data and save it in a more useful form.

In this process, a simple peak finding algorithm is implemented to try and identify the beat frequency in the data. The "Averaging Width" can be set depending on the data to try and identify the correct frequency spike — however, a high averaging width can

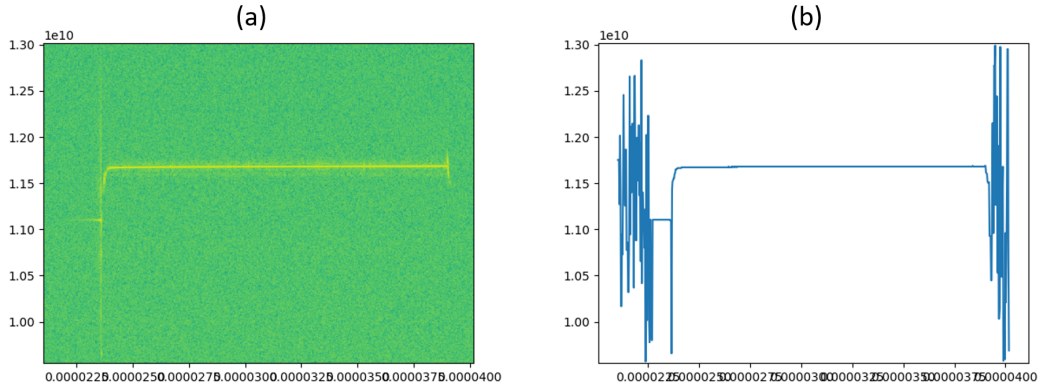


FIGURE B.2: Screenshot of the data calibration section of the Matlab app.

drastically increase the computation time. If there are multiple, simultaneous peaks, then the "Number of Peaks" can be adjust to peak up the highest N peaks in the frequency.

By pressing "Find Peaks", a graph similar to Figure B.2(b) is generated, showing a line graph of the beat frequency against time. By inputting the appropriate "Probe Wavelength" and "Refractive Index" and selecting "Convert to Velocity" this frequency-time graph is converted into a velocity-time graph. This graph can then be saved as it is, or it can be integrated to give a distance-time graph — this was done to generate the PDV data in Figure 4.8, for example.

# Bibliography


[1] R. Meyer, J. Köhler, and A. Homburg. *Explosives*. Wiley, 6th edition, 2007. ISBN: 978-3-527-31656-4.

[2] S. Venugopalan. *Demystifying Explosives: Concepts in High Energy Materials*. Elsevier, 2015. ISBN: 978-0-12-801576-6.

[3] M. Pasha, D. Zaini, and A.M. Shariff. Physical explosion analysis in heat exchanger network design. *IOP Conf. Series: Earth and Environmental Science*, 36:012005, 2016.

[4] S. Glasstone and P.J. Dolan. *The Effects of Nuclear Weapons*. United States Department of Defense and the United States Department of Energy, 3rd edition, 1977. ISBN: 978-1603220163.

[5] National park service handbook for the transportation, and use of explosives. `https://www.nps.gov/parkhistory/online_books/npsg/explosives/index.htm`, 1999. [Online; accessed 24-April-2019].

[6] W. Fickett and W.C. Davis. *Detonation: Theory and Experiment*. Dover Publications, 2000. ISBN: 0-486-41456-6.

[7] L.F. Henderson, G. Ben-Dor, O. Igra, and T. Elperin. *Handbook of Shockwaves*, volume 1. Academic Press, 2001. ISBN: 0-12-086431-2.

[8] M. Suceska. Experimental determination of detonation velocity. *Fragblast*, 1(3):261, 1997.

[9] C.A. Handley, B.D. Lambourn, N.J. Whitworth, H.R. James, and W.J. Belfield. Understanding the shock and detonation response of high explosives at the continuum and meso scales. *Applied Physics Reviews*, 5(1):011303, 2018.

[10] G. Baudin, M. Roudot, M. Genetier, P. Mateille, and A. Lefrançois. Shock-to-detonation transition of RDX, HMX and NTO based composite high explosives: experiments and modelling. *Journal of Physics: Conference Series*, 500:052004, 2014.

[11] S. Gilbertson, S.I. Jackson, S.W. Vincent, and G. Rodriguez. Detection of high explosive detonation across material interfaces with chirped fiber Bragg gratings. *Appl. Opt.*, 54(13):3849, 2015.

[12] J.S. Wilson. *Sensor Technology Handbook*. Elsevier, 2005. ISBN: 0-7506-7729-5.

[13] E. Udd. An overview of fiber-optic sensors. *Review of Scientific Instruments*, 66(8):4015, 1995.

[14] N. Sabri, S.A. Aljunid, M.S. Salim, R.B. Ahmad, and R. Kamaruddin. Toward optical sensors: Review and applications. *Journal of Physics: Conference Series*, 423:012064, 2013.

[15] K.O. Hill, Y. Fujii, Derwyn C. Johnson, and B.S. Kawasaki. Photosensitivity in optical fiber waveguides: Application to reflection filter fabrication. *Applied physics letters*, 32(10):647, 1978.

[16] S.J. Mihailov. Fiber Bragg grating sensors for harsh environments. *Sensors*, 12(12):1898, 2012.

[17] J.W. Arkwright, N.G. Blenman, I.D Underhill, S.A. Maunder, M.M. Szczesniak, P.G. Dinning, and I.J. Cook. In-vivo demonstration of a high resolution optical fiber manometry catheter for diagnosis of gastrointestinal motility disorders. *Opt. Express*, 17(6):4500, 2009.

[18] T.K. Gangopadhyay, M.C. Paul, and L. Bjerkan. Fiber-optic sensor for real-time monitoring of temperature on high voltage (400kV) power transmission lines. *Proceedings of SPIE*, 7503:75034M–1, 2009.

[19] J.M. Lopez-Higuera, L.R. Cobo, A.Q. Incera, and A. Cobo. Fiber optic sensors in structural health monitoring. *Journal of Lightwave Technology*, 29(4):587, 2011.

[20] B. Singh, H. Rana, S. Kumar, P. Bhulania, and G. Minocha. A novel design of fiber optic gyroscope based INS system for UAS applications. *Procedia Computer Science*, 57:1317, 2015.

[21] E.M. Chan, V. Lee, S.P. Mickan, and P.J. Davies. Low-cost optoelectronic devices to measure velocity of detonation. *Proceedings of SPIE*, Vol. 5649:586, 2005.

[22] J. Pachman, M. Kunzel, K. Kubat, J. Selesovsky, R. Marsalek, M. Pospisil, M. Kubicek, and A. Prokes. Optimex: Measuring of a detonation velocity with passive optical fiber system. *Central European Journal of Energetic Materials*, 14(1):233, 2017.

[23] L.K. Cheng and J. van Bree. Fiber-optic sensors in explosion and detonation experiments. *SPIE Newsroom*, 2007.

[24] M.A. Shinas and D.L. Doty. 1550nm fiber optic TOAD (time of arrival diagnostic) for measuring sub-nanosecond resolution of detonation break out. *AIP Conference Proceedings*, 1979:160025, 2018.

[25] P.D. Sargis, N.E. Molau, D. Sweider, M.E. Lowry, and O.T. Strand. Photonic doppler velocimetry. *LLNL e-report, UCRL-ID-133075*, 1999.

[26] D.H. Dolan. Accuracy and precision in photonic doppler velocimetry. *Review of Scientific Instruments*, 81(5):053905, 2010.

[27] P.A. Frugier, P. Mercier, J. Bénier, J. Veaux, M. Debruyne, C. Rion, and E. Dubreuil. Pdv and shock physics: application to nitro methane shock-detonation transition and particles ejection. *Proceedings of SPIE*, 7429:742913, 2009.

[28] P.H. Netherwood. Detonation velocity measurements of the explosives detasheet c and amatol. *US Army Ballistic Research Laboratory, Memorandum Report, 3427*, 1985.

[29] J. Benterou, E. Udd, P. Wilkins, F. Roeske, E. Roos, and D. Jackson. In-situ continuous detonation velocity measurements using fiber-optic Bragg grating sensors. *LLNL e-report, UCRL-Proceedings-233137*, 2007.

[30] G. Rodriguez, R.L. Sandberg, Q. McCulloch, S.I. Jackson, S.W. Vincent, and E. Udd. Chirped fiber Bragg grating detonation velocity sensing. *Review of Scientific Instruments*, 84(1):015003, 2013.

[31] Y. Barbarin, A. Lefrancois, G. Zaniolo, V. Chuzeville, L. Jacquet, S. Magne, J. Luc, and A. Osmont. Optimization of detonation velocity measurements using a chirped fiber Bragg grating. *Proceedings of SPIE*, 9480:94800S–1, 2015.

[32] P. Wei, H. Lang, T. Liu, and D. Xia. Detonation velocity measurement with chirped fiber Bragg grating. *Sensors (Basel, Switzerland)*, 17(11):2552, 2017.

[33] S. Magne, A. Lefrancois, J. Luc, G. Laffont, and P. Ferdinand. Real-time, distributed measurement of detonation velocities inside high explosives with the help of chirped fiber Bragg gratings. *Proceedings of SPIE*, 8794:87942K–1, 2013.

[34] J. Benterou, C.V. Bennett, G. Cole, D.E. Hare, C. May, E. Udd, S.J. Mihailov, and P. Lu. Embedded fiber optic Bragg grating (FBG) detonation velocity sensor. *Proceedings of SPIE*, 7316:73160E, 2009.

[35] G. Rodriguez and S.M. Gilbertson. Ultrafast fiber Bragg grating interrogation for sensing in detonation and shock wave experiments. *Sensors*, 17(2):248, 2017.

[36] J.D. Weiss. Impurity-doped fiber-optic shock position sensor. *Journal of lightwave technology*, 12(10):1891, 1994.

[37] F. Majiet and F.J. Mostert. Investigation on the influence of the initial RDX crystal size on the performance of shaped charge warheads. *Defence Technology*, 2019. DOI: 10.1016/j.dt.2019.07.008.

[38] M. Künzel, J. Selesovsky, and J. Pachman. First attempts in cylinder expansion testing. *New Trends in Research of Energetic Materials*, 2017:736, 2017.

[39] P.D. Dragic. The acoustic velocity of ge-doped silica fibers: A comparison of two models. *International Journal of Applied Glass Science*, 1 (3):330, 2010.

[40] G. Nahmani and Y. Manheimer. Detonation of nitromethane. *The Journal of Chemical Physics*, 24(5):1074, 1956.

[41] OSI Optoelectronics. Photodiode characteristics and applications. `http://www.osioptoelectronics.com/application-notes/AN-Photodiode-Parameters-and-Characteristics.pdf`. [Online; accessed 11-March-2019].

[42] Thorlabs. PDA10CF(-EC) InGaAs Amplified Detector: User Guide. `https://www.thorlabs.com/thorproduct.cfm?partnumber=PDA10CF`. [Online; accessed 26-October-2018].

[43] Newport. USER'S GUIDE 125-MHz Photoreceivers: Models 1801 and 1811. `http://assets.newport.com/webDocuments-EN/images/1801_And_1811_User_Manual_RevG.PDF`. [Online; accessed 26-October-2018].

[44] K. Okamoto. *Fundamentals of optical waveguides, Chapter 4.* Gulf Professional Publishing, 2000. ISBN: 9780125250962.

[45] A. Othonos and K. Kalli. *Fiber Bragg gratings, Chapter 5.* Artech House, 1st edition, 1999. ISBN: 0-89006-344-3.

[46] T. Erdogan. Fiber grating spectra. *Journal of Lightwave Technology*, 15(8):1277, 1997.

[47] R. Kashyap. *Fiber Bragg gratings, Chapter 4.* Academic Press, 1999. ISBN: 9780123725790.

[48] M. Ibsen, M.K. Durkin, M.N. Zervas, A.B. Grudinin, and R.I. Laming. Custom design of long chirped Bragg gratings: Application to gain-flattening filter with incorporated dispersion compensation. *IEEE Photonics Technology Letters*, 12(5):498, 2000.

[49] A. Othonos and K. Kalli. *Fiber Bragg gratings, Chapter 2.* Artech House, 1st edition, 1999. ISBN: 0-89006-344-3.

[50] K.O. Hill and G. Meltz. Fiber Bragg grating technology fundamentals and overview. *J. Lightwave Technol.*, 15(8):1263, 1997.

[51] M.J. Yuen. Ultraviolet absorption studies of germanium silicate glasses. *Applied Optics*, 21(1):136, 1982.

[52] G. Meltz, W.W. Morey, and W.H. Glenn. Formation of Bragg gratings in optical fibers by a transverse holographic method. *Optics letters*, 14(15):823, 1989.

[53] A. Othonos and K. Kalli. *Fiber Bragg gratings, Chapter 4.* Artech House, 1st edition, 1999. ISBN: 0-89006-344-3.

[54] G.D. Marshall, R.J. Williams, N. Jovanovic, M.J. Steel, and M.J. Withford. Point-by-point written fiber-Bragg gratings and their application in complex grating designs. *Optics express*, 18(19):19844, 2010.

[55] P.J. Lemaire, R.M. Atkins, V. Mizrahi, and W.A. Reed. High pressure h/sub 2/loading as a technique for achieving ultrahigh uv photosensitivity and thermal sensitivity in geo/sub 2/doped optical fibres. *Electronics Letters*, 29(13):1191, 1993.

[56] M. Yamada and K. Sakuda. Analysis of almost-periodic distributed feedback slab waveguides via a fundamental matrix approach. *Appl. Opt.*, 26(16):3474, 1987.

[57] M.A. Muriel and A. Carballar. Internal field distributions in fiber Bragg gratings. *IEEE Photonics Technology Letters*, 9(7):955, 1997.

[58] J. Pooley, E. Price, J. W. Ferguson, and M. Ibsen. Optimised chirped fibre Bragg gratings for detonation velocity measurements. *Sensors*, 19(15):3333, 2019.

[59] Y. O. Barmenkov, D. Zalvidea, S. Torres-Peiró, J.L. Cruz, and M.V. Andrés. Effective length of short fabry-perot cavity formed by uniform fiber Bragg gratings. *Opt. Express*, 14(14):6394, 2006.

[60] R. Feced and M.N. Zervas. Effects of random phase and amplitude errors in optical fiber Bragg gratings. *Journal of Lightwave Technology*, 18(1):90, 2000.

[61] D.J. Kitcher, A. Nand, S.A. Wade, R. Jones, G.W. Baxter, and S.F. Collins. Directional dependence of spectra of fiber Bragg gratings due to excess loss. *Journal of the Optical Society of America A*, 23(11):2906, 2006.

[62] J. Pooley, E. Price, J. W. Ferguson, and M. Ibsen. Detonation velocity measurements with uniform fibre Bragg gratings. *Optics Express*, 27(16):23464, 2019.

[63] N.Y. Fan, S. Huang, A.T. Alavie, and R.M. Measures. Rare earth doped fibre for structural damage assessment. *Smart Materials and Structures*, 4(3):179, 1995.

[64] J. Pooley, E. Price, J. W. Ferguson, and M. Ibsen. Detonation velocity measurements using rare-earth doped fibres. *Sensors*, 19(7):1697, 2019.

[65] K. Li, X. Li, H. Yan, X. Wang, and Y. Wang. Study of continuous velocity probe method for the determination of the detonation pressure of commercial explosives. *Journal of Energetic Materials*, 36(4):377, 2018.

[66] E. D. Black. An introduction to pound–drever–hall laser frequency stabilization. *American journal of physics*, 69(1):79, 2001.

[67] S. Hilbert. FFT zero padding. `http://www.bitweenie.com/listings/fft-zero-padding/`, 2013. [Online; accessed 29-March-2019].

# Publications and Events

## Publications

- J. Pooley, E. Price, J. W. Ferguson, and M. Ibsen. Detonation velocity measurements using rare-earth doped fibres. *Sensors*, 19(7):1697, 2019.
- J. Pooley, E. Price, J. W. Ferguson, and M. Ibsen. Detonation velocity measurements with uniform fibre Bragg gratings. *Optics Express*, 27(16):23464, 2019.
- J. Pooley, E. Price, J. W. Ferguson, and M. Ibsen. Optimised chirped fibre Bragg gratings for detonation velocity measurements. *Sensors*, 19(15):3333, 2019.

## Conferences Attended

- *Defence and Security Doctoral Symposium 2017*, Cranfield University (Shrivenham Campus), 2017. [poster presentation]

## Short Courses Attended

- *Key Concepts of Shock Hydrodynamics*, Imperial College London, 2016.
- *Introduction to Explosives*, Cranfield University (Shrivenham Campus), 2017.